

Biologically Inspired Problems Concerning Semiflexible Filaments

**Organization in Plant Cell Geometries
Hydrodynamics of Propulsion**

Marco Cosentino Lagomarsino

2004

Biologically Inspired Problems Concerning Semiflexible Filaments

PROEFSCHRIFT

ter verkrijging van
de graad van doctor aan de Universiteit Leiden
op gezag van de Rector Magnificus Dr D.D. Breimer
hoogleraar in de faculteit der Wiskunde en
Natuurwetenschappen en die der Geneeskunde,
volgens besluit van het College voor Promoties
te verdedigen op dinsdag 25 mei 2004,
klokke 14:15 uur

door

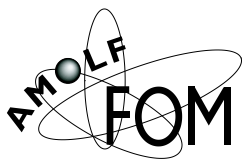
Marco Cosentino Lagomarsino

geboren te Verona
in 1974

Promotor: prof. dr. M. Dogterom

Referent: prof. dr. F. C. Mackintosh (Vrije Universiteit Amsterdam)

Overige Leden: prof. dr. B. M. Mulder (Universiteit Wageningen)
prof. dr. A. M. Emons (Universiteit Wageningen)
prof. dr. W. van Saarloos
prof. dr. P. Kes
dr. C. P. Lowe (Universiteit van Amsterdam)
prof. dr. H. Spaink



The work described in this thesis was performed at the FOM Institute for Atomic and Molecular Physics, Kruislaan 407, 1098 SJ, Amsterdam, The Netherlands. The work is part of the research program of the Stichting voor Fundamenteel Onderzoek der Materie (FOM) and was made possible by financial support from the Nederlandse Organisatie voor Wetenschappelijk Onderzoek (NWO).

Cover: coiled microtubules in a micro-chamber.

ISBN: 90-77209-08-5

A digital color version of this thesis can be downloaded from <http://www.amolf.nl>

Acknowledgments

Most of the work presented in this thesis is the fruit of direct collaboration. Although sometimes this kind of work requires larger efforts than working alone, I believe in its power to generate ideas beyond the reach of each individual that contributes to it. For this reason, I feel it is most appropriate to start by thanking a few people.

Anne Mie Emons and Jan Vos have been my window on plant cell biology during the project presented in the first part of this thesis. At the beginning, the discussions with them were very puzzling for me. I learned many things from this puzzlement. My background is in theoretical physics, and it was not always easy for me to have the carefulness and the tenacity required for experimental work. Doing experiments with Jan was instructive and fun.

With Catalin Tanase I worked on some of the theoretical aspects of the same project on plant cells, and exchanged information on others. Once given a mathematical problem, Catalin does not desist until it is completely unfolded. He is the only person I know on this planet to be confident with Mathematica and its human interface. Bela Mulder, Catalin's supervisor, helped us in many stages of the plant project.

Frank Julicher and Karsten Kruse, in Dresden, introduced Catalin and me to the theoretical approach presented in chapter 5. I particularly like their "blackboard" discussion style, that goes directly to the core of the problems. Alexander Zumdieck shared these blackboard discussions and the work with us.

Fabrizio Capuani is the person who introduced me to the world of computer simulations. He taught me how to debug a code, the most precious skill, but the most boring work! Fabrizio is a very good friend, and one of the maximum experts on Skinner's Constant (Flannegan's Finagling Factor).

Christopher Lowe started with Fabrizio and me the project on filament motility presented in the second part of this thesis. Chris is great in reasoning in "rescaled" terms, and appreciates the value of pure numbers. Perhaps one day he will have his own (however, it will be a "Lowe" number).

Ignacio Pagonabarraga joined the motility project later on, and added his expertise on hydrodynamics and his meticulousity. Marjolein Dijkstra started me up with the simulations presented in chapter 3; Daan Frenkel had the idea to investigate the Kosterlitz-Thouless transition with these simulations, and helped me developing it. Maurice Van Den Boer, Arjan Van Zuuk and Chris Retif helped me with lithography work, and Enrico Conti, another theoretical physicist with experimental curiosities, worked with me on the *in vitro* self-organization of microtubules and motors.

Finally, I want to thank [the person that I cannot thank]. During these four years, she gave me the room to steer my project(s) in the directions I wanted, and the credits for my competence. This is not obvious, and required a lot of trust on her side. Many aspects of the work turned out not to be easy, but, when problems arose, she was always tolerant and open to discuss them.

I wish to thank a number of other people who were not directly involved in the

work presented here. Bruno Bassetti and Patrizia Jona, for the work done together, the many stimulating discussions and the moral help. Vita and Guido, my parents. Fabrizio (again) and Simone, the paranymphs. Simon, Gerbrand, Chantal, for critical reading of this manuscript. Annamaria, Nicola, Gherardo, Ponda. The people at the AMOLF reception. The international group of AMOLF and of the overloop in particular: people from many different cultures (quite a few of these cultures come from Italy) living in harmony. Gerbrand, who taught me most of the (little) Dutch I speak, and the other present and former members of my group. Barbara, for being, and for 13 other excellent reasons. This thesis owes you a great deal, and is dedicated to you. On the other hand, what I owe you is incommensurable.

This Thesis is Partly Based on the Following Papers

Cosentino Lagomarsino M., Dogterom M., Dijkstra M. “Isotropic-nematic Transition of Long, Thin, Hard Spherocylinders Confined in a Quasi-two-dimensional Planar Geometry”

J Chem Phys 119 (6): 3535-3540 AUG 8 2003 (Chapter 3).

Cosentino Lagomarsino M., Tanase C., Mulder B., Dogterom, M. Emons A., Vos, J. “Modeling the Dynamic Spring with Microtubules in Micro-fabricated Chambers”

In Preparation (Chapter 4).

Zumdieck A., Cosentino Lagomarsino M., Tanase C., Mulder B., Dogterom, M., Kruse K., Jülicher, F. “Mean Field Approach to Pre-prophase Band Formation as a Motor-filament Self-organization Process”

In Preparation (Chapter 5).

Cosentino Lagomarsino M., Capuani F., Lowe C.P. “A Simulation Study of the Dynamics of a Driven Filament in an Aristotelian Fluid”

J Theor Biol 224 (2): 215-224 SEP 21 2003 (Chapter 8).

Cosentino Lagomarsino M., Pagonabarraga I., Lowe C.P. “A Computationally Efficient Method to Simulate Elastic Filaments with Hydrodynamic Interactions”

In Preparation (Chapter 9).

Other Papers by the Same Author

Bassetti B., Cosentino Lagomarsino M., Jona P. “A Model for the Self-organization of Microtubules Driven by Molecular Motors”

Eur Phys J B 15 (3): 483 – 492 2000

Cosentino Lagomarsino M., Bassetti B., Jona P. “Rowers Coupled Hydrodynamically. Modeling Possible Mechanisms for the Cooperation of Cilia”

Eur Phys J B 26 (1): 81-88 MAR 2002

Cosentino Lagomarsino M., Jona P., Bassetti B. “Metachronal Waves for Deterministic Switching Two-state Oscillators with Hydrodynamic Interaction”

Phys Rev E 68 (2): Art. No. 021908 Part 1 AUG 2003

Contents

1. Introduction	1
1.1. Microtubules	1
1.2. Flagella and Microorganism Motility	3
I. Organization of Microtubules in Interphase Plant Cells	5
2. Overview of the Problems	7
2.1. Specificity of Plant Cell Morphology Over the Cell Cycle	7
2.2. The Interphase Cortical Microtubule Arrays	10
2.3. Scenarios	13
3. Microtubules Confined in a Quasi-Two-Dimensional Planar Geometry.	15
3.1. Introduction	15
3.2. Methods	17
3.3. Results	20
3.4. Discussion and Conclusions	31
3.A. Computing Orientational Order for a Collection of Bezier Curves .	32
4. Coiling of Microtubules Confined in Box-like chambers	35
4.1. Introduction	35
4.2. Materials and Methods	36
4.3. Results	40
4.4. Discussion and Conclusion	50
5. Mean Field Approach to Pre-prophase Band Formation.	53
5.1. Introduction	53
5.2. Derivation of the Equations	55
5.3. Stability Analysis and Phase Diagram	59
5.4. Solutions of the Nonlinear Mean Field Equations	67
5.5. The State of Microscopic Modeling and Experiments	70
5.6. Conclusions	73

6. Discussion and Open Problems	75
6.1. Considerations on the Scenarios	75
6.2. Other Scenarios for the Interphase Patterns	77
II. Hydrodynamics of Flexible Rod Based Microorganism Motility. A Simulation Study.	81
7. Overview of the Problems	83
8. Dynamics of a Driven Semiflexible Polymer at Low Reynolds Number	89
8.1. Introduction	89
8.2. Model and Simulation	90
8.3. Wiggling Motion	93
8.4. Rotating Constraint	102
8.5. Conclusions	105
8.A. Unequal Friction Coefficients as a Condition for Motility	106
8.B. Analytical Computation of the Swimming Velocity	107
9. A Method to Include Oseen-level Hydrodynamic Interaction	109
9.1. Introduction	109
9.2. Description of the Method	110
9.3. Measurement of the Friction Coefficients and Sedimentation	113
9.4. Sedimentation of an Oblique Filament	116
9.5. One-Armed Swimmer with Hydrodynamic Interaction	120
9.6. Conclusions	121
10. Discussion and Open Problems	123
Bibliography	125
Samenvatting	135
Curriculum Vitae	139

1. Introduction

This thesis relates to filaments. The filaments we will be concerned with can be found in every cell of any living being on this planet which belongs to the class of eukaryotes. Plants, cats, mosquitoes, whales and yeast are eukaryotes; bacteria do not belong to the club, they are prokaryotes. Cells are the elementary working units of the earth living systems. Eukaryotic cells are bigger, more complex, and carry more complex tasks than prokaryotic ones. In fact, prokaryotes are never bigger than just one cell.

Filaments are used in cells for a wide variety of purposes. Perhaps the most known example (which, however, does not concern this thesis) is that both eukaryotes and prokaryotes use a filamentous structure, the DNA, to process information. Eukaryotic cells also use filaments to define their changing internal and external structure and shape, for example when they divide. An example of such process will be the subject of the first part of this thesis. The filaments performing tasks related to cell structure are the main part of the so-called cytoskeleton, by analogy the “skeleton” of the cell. Some specialized cells and unicellular organisms use cytoskeletal filaments to propel a fluid or to propel themselves in a fluid, as is the case for a sperm cell. The hydrodynamics of swimming using a microscopic filamentous appendage will be the subject of the second part.

Since these two topics, although related, are quite different, I divided the thesis in two separate parts, which can be read independently. Each part has its own introductory and closing chapter. I will use the rest of this introduction to set a general framework.

1.1. Microtubules

The first part of the thesis will be concerned specifically with microtubules [1], a particular kind of filament used by eukaryotes. Its subject will be the organization of microtubules before the division of plant cells.

Microtubules (Fig. 1.1) are tubular polymers of the protein tubulin. They are flexible, but at the same time very stiff. In fact, microtubules are the stiffest polymers available to eukaryotic cells, with a persistence length (the length that they have to reach for a thermal fluctuation to bend them) of about 3 millimeters [2], two orders of magnitude greater than their typical length.

The length of microtubules is governed by the “dynamic instability” process [4, 5, 1], which is responsible for stochastic transitions, driven by the far-from-

1. Introduction

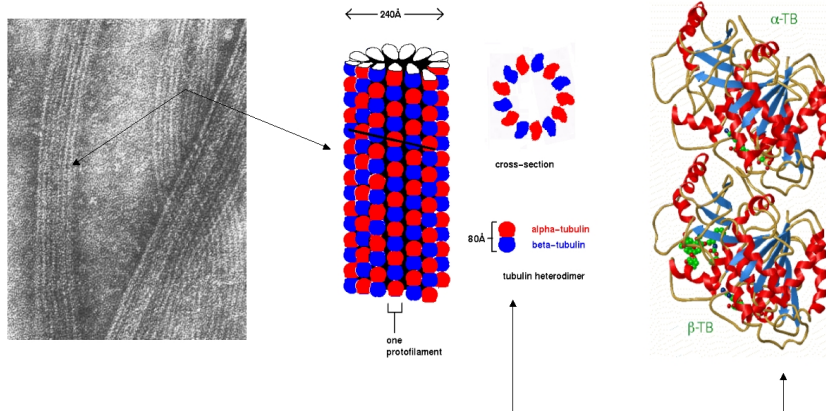


Figure 1.1.: Microtubules and their structure. Left panel: a transmission electron micrograph of microtubules (Gwen Childs, Univ. of Texas, USA). Middle panel: sketch of microtubule structure (John Kenney, Birbeck College, London UK). Right panel: crystallographic structure of tubulin dimer (adapted from ref. [3]).

equilibrium chemical reaction of GTP (Guanosine Tri-Phosphate, a phosphorylated nucleoside composed of guanine, ribose, and three phosphate groups) hydrolysis, between states of polymerization and depolymerization. The dynamic instability is characterized by four parameters, two velocities (growth and shrinkage) and two transition probabilities, called “catastrophe” and “rescue” frequency. The values of these parameters, which depend on physical quantities such as temperature and tubulin concentration, determine whether a steady state exists, or whether the polymers are in a so-called “unbounded growth” state, where their average length increases with time (see Fig 1.2). The steady state length distribution is typically exponential.

In the cells, microtubules are fundamental for the structural organization and its dynamical changes, for instance during cell division. They also play a role in transport processes, for example in the axons of neural cells. How do microtubules generate the forces necessary for all these processes? Besides being themselves active, through the process of dynamic instability, microtubules interact with a class of force generating proteins, called molecular motors [6], which are able to use the energy released by the hydrolysis of ATP (Adenosine Tri-Phosphate, an analogue of GTP that supplies energy for many biochemical cellular processes by undergoing enzymatic hydrolysis). The two main microtubule-interacting classes of molecular motors are called kinesins and dyneins. Actin microfilaments, the other kind of active cytoskeletal filaments, also interact with the molecular motor myosin, and are perhaps more widely known, because the forces they generate are the source of muscle contraction.

How microtubules and actin filaments organize cooperatively into different struc-

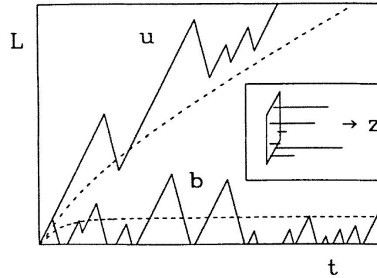


Figure 1.2.: Dynamic instability of microtubules. The graph shows the typical fluctuating (solid lines) and mean (dashed lines) behavior of a microtubule length as a function of time, in presence of dynamic instability, in the regimes of bounded (b) and unbounded (u) growth respectively. Figure adapted from reference [5].

tures which generate the morphology of cells is a fundamental question in cell biology, which has many physical aspects. I will analyze a particular realization of this problem, the case of microtubule organization between two cell divisions in plant cells.

1.2. Flagella and Microorganism Motility

In the second part of the thesis I will analyze the motion of flexible filaments used for propulsion, focusing on some hydrodynamic aspects of this process. The inspiration for this work comes from the swimming of flagellated cells. Flagella [7] are long and thin protuberances of the cell membrane, that contain a highly organized array of microtubules and dynein molecular motors. The forces generated by this array are able to modify the shape of flagella and make the cell swim in a fluid. However, swimming is not a trivial issue for a mesoscopic body, because it cannot rely, as we do, on inertia. To create macroscopically a similar environment we would have to try to swim in something very viscous, like molasses.

One can separate two different sorts of problems concerning flagella. One is how the many interacting internal devices cooperate to generate the forces, and thus the shape. The other is how generically a flexible mesoscopic filament can swim in absence of inertia, how fast and how efficient it can be. I will consider this second problem.

1. Introduction

Part I.

**Organization of
Microtubules in Interphase
Plant Cells**

2. Overview of the Problems

The general importance of investigating the organization of cytoskeletal filaments (and of microtubules in particular) in eukaryotic cells is related to their role in cell morphogenesis [8, 9]. The cytoskeleton can be seen as an active system of proteins and filamentous protein assemblies through which a cell defines its shape, and therefore many aspects of its identity. We all know that the shape of animals is quite distinct from the shape of plants. This is true also at the cell level, although the set of basic proteins that constitute the cytoskeletal machinery in animals and higher plants is largely the same, and these proteins are highly conserved between the kingdoms. In other words, the few existing plant-specific genomic modifications are sufficient to give rise to a quite distinct morphology on many different levels of spatial organization [10, 11]. The question is then what the few essential relevant features at the protein level are that distinguish two morphological categories within eukaryotes. One particularly intriguing realization of this problem forms the motivation for the work I am presenting in this first part of the thesis: the formation of the microtubule cortical interphase array [12, 13, 14, 15] and the preprophase band [16, 17, 14, 18, 19], two patterns with no equivalent in animal cells (Fig. 2.3).

2.1. Specificity of Plant Cell Morphology Over the Cell Cycle

Let us first look at some of the key features that single out the morphology of plant cells, and how they relate with the cytoskeleton. Unlike animal cells, plant cells are constrained within rigid cell walls and are unable to rapidly change shape or to migrate. Cellulose microfibrils are synthesized by a particular enzymatic complex, the cellulose synthase, which is integrated into the plasma membrane [15, 20]. Because plant cells are enclosed in cell walls, their polar growth is an essentially irreversible process that plays a key role during organ morphogenesis. Polar plant cell growth is largely controlled by cell wall properties and is therefore based on completely different mechanisms than the growth of animal cells.

A second main difference with animal cells, is that plant cells generally contain large vacuoles that take up most of the cell volume [21] (Fig. 2.1). Vacuoles are water-containing cavities that perform various functions. They can act as a storage or degradation compartment for nutrients or waste products, as a cost-effective way of increasing cell size, and as a homeostatic regulator controlling both tur-

2. Overview of the Problems

gor pressure and pH of the cytosol. In vacuolated plant cells, the cytoplasm is restricted to thin layers in the cell cortex and around the nucleus, which are linked by transvacuolar cytoplasmic strands. For this reason, during interphase, plant microtubules are found predominantly in the cortical cytoplasm, where they are irregularly, obliquely, or longitudinally arranged.

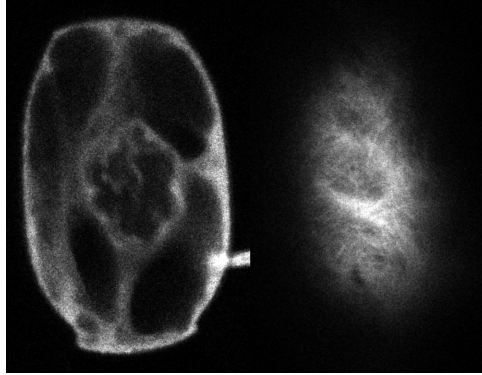


Figure 2.1.: Vacuoles and the microtubule cytoskeleton. The figure shows two confocal sections of a *Tradescantia Virginiana* cell microinjected with fluorescently labeled tubulin purified from pig brain (Jan Vos, University of Wageningen, NL). The left panel is a mid-plane section. Here, the dark areas that fill most of the cell volume are the vacuole. Microtubules (white in the picture) are confined in thin regions surrounding the nucleus and the cortex, and in thread-like volumes called cytoplasmic strands. The right panel is a top-plane section, showing cortical microtubules.

Another fundamental morphological characteristic of plant cells goes back to specificities in the microtubular cytoskeleton: plant cells have no centrosomes [14]. The typical locations of microtubules in animal cells are asters, spindles and flagella. In these cases, microtubules emanate from centrosomes, microtubule-nucleating complexes that are centered on a microtubule-derived apparatus known as a centriole. Centrosomes can act interchangeably as spindle poles, anchors for the radial interphase array or basal bodies for cilia and flagella. In fact, centrosomes are absent from up to half of known eukaryotic species including most fungi, protists and vascular plants and from the spindles and interphase arrays of many algae [6].

Plant microtubule arrays perform functions that relate to the development of the plant cell wall and, hence, to plant cell shape and growth polarity (the choice of a preferred direction of cell expansion). Given the underlying differences we have discussed, what does the microtubular cytoskeleton look like in plants? Single cell model systems such as tobacco BY-2 suspension cells, *Tradescantia Virginiana* stamen hair cells, guard cell initials, cultured pollen tubes, root hairs, trichomes, mesophyll cells and algal cells have been widely exploited to investigate cytoskeletal functions in the cellular processes that affect development [22, 14, 13, 23, 24].

2.1. Specificity of Plant Cell Morphology Over the Cell Cycle

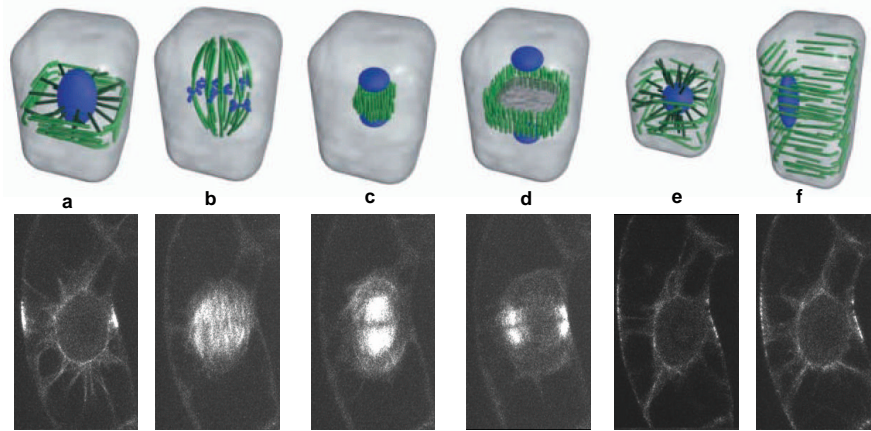


Figure 2.2.: Microtubule arrays during the plant cell cycle. Upper panel, schematic illustration of the three-dimensional configuration of the filaments (adapted from ref. [14]). Lower panel, two-dimensional confocal mid-plane sections of tobacco BY-2 cells, stably expressing GFP-MBD, a microtubule binding domain that originally belongs to the microtubule-associated protein MAP4. The bright areas represent microtubules (Jan Vos, University of Wageningen, NL). (a) Preprophase band. (b) Mitotic spindle (metaphase). (c) Early phragmoplast (telophase). (d) Late phragmoplast. (e) Early cortical interphase array. (f) Late cortical interphase array.

During prophase, microtubules form a mitotic spindle as in animal cells. Spindle poles are typically broad, not tightly focused as in centrosome-containing cells [14] (Fig. 2.2b).

In cytokinesis, the process that results in the separation of two daughter cells following completion of nuclear division, the presence of the external wall prevents a plant cell from forming a membrane neck and cleave it, as animal cells do (using a contractile actin ring, the cleavage furrow). Plants have evolved a unique mode of cytokinesis. A new cell wall, the cell plate, is built by targeted secretion between the two daughter nuclei. Cell plate formation is initiated in the cell center and proceeds centrifugally until the new cell wall fuses with the parental cell wall. Positioning of the cell plate is of crucial importance for plant morphogenesis and is under cytoskeletal control [21]. At the anaphase-telophase transition, microtubules form the so-called “phragmoplast” (Fig. 2.2c and d). Like spindles, phragmoplasts are bipolar complexes containing microtubules with their plus ends meeting at the mid-plane. They direct the transport of vesicles from the Golgi apparatus towards the centrifugally expanding cell plate, which becomes the cross-wall at the interface of daughter cells [14].

Dividing cells in young plant organs generally form perpendicular to the organ surface cell plates. After completing the cell cycle, newly formed cells elongate

2. Overview of the Problems

perpendicularly to the cell plate, resulting in the controlled, directed expansion of developing organs. During embryogenesis and meristem (undifferentiated tissue) development, cell plates in single dividing cells are parallel to the surface, leading to the establishment of new cell layers. Together, these processes are responsible for the organization of cells in files and layers that is typically observed in plant tissues [21].

Microtubules and actin filaments appear to have essential functions in cell plate positioning. At an early stage of cell division, cortical microtubules reorganize into a ring of parallel bundles, the preprophase band (Fig. 2.2a). Actin filaments are also present in this array and may be required for its final restriction to a narrow ring. The preprophase band predetermines the site where the maturing cell plate will fuse with the parental cell wall. It disappears completely when the spindle is formed, but is thought to leave landmarks in the cell cortex that guide the extending cell plate to the correct fusion site [17].

2.2. The Interphase Cortical Microtubule Arrays

In this part of the thesis, we will be concerned with the cortical microtubule structures formed during the interphase of plant cells. The first structure is the cortical microtubule array. It consists of the alignment of the filaments and their typically transverse arrangement with respect to the cell elongation axis. This pattern can be observed already in the early stages of the interphase. The second structure, the preprophase band, forms just before cell division (hence the name) and corresponds to the formation of a narrow, ring-like pattern of transverse microtubules marking the division site of the plant cell. Both patterns (Fig. 2.3 and 2.4), which have the highly conserved protein tubulin as basic building block, are important for many morphological tasks performed by the cell (such as elongation, division, orientation and differentiation). It is therefore useful and natural to ask whether the mechanisms of organization underlying these patterns are universal within higher plants.

The plant cell biology literature on the organization of cortical microtubules in interphase appears somewhat fragmented, often incoherent, and sometimes even contradictory. There are at least two reasons for this. First, that the different experimental techniques exploited give partial visions which are often hard to reconcile. The second reason is that the questions biologists ask are usually quite different from the ones a physicist would ask when confronted with the same problems, in the sense that the details of the mechanism through which phenomena are linked often seem to remain uninvestigated or are considered irrelevant. As a matter of fact, it must be admitted that what seems unsatisfactory to a physicist is in fact an operationally very efficient way of connecting pieces of evidence without which progress would be impossible (this is connected with the more general issue that the whole concept of causality used in biology differs from the one used in physics).

Let us now return to the case of the cortical microtubules assemblies in interphase. While by no means pretending to be exhaustive, I will list a few of the main

2.2. The Interphase Cortical Microtubule Arrays

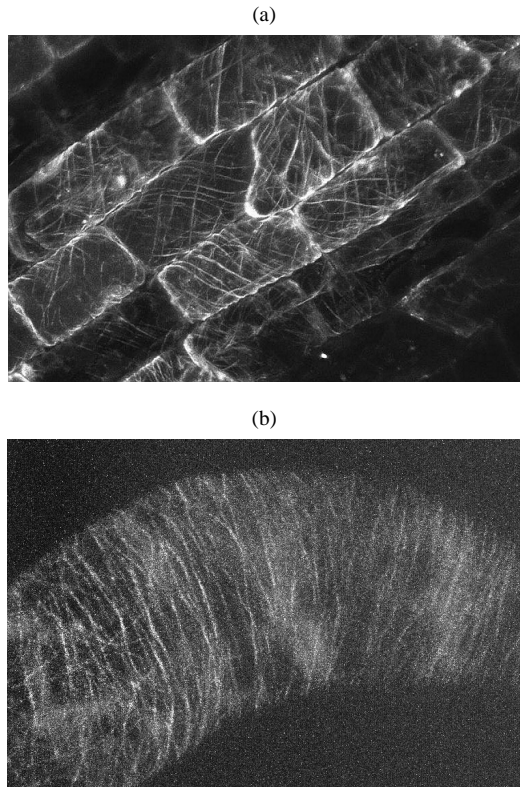


Figure 2.3.: Plant cells in interphase with fluorescent GFP-MBD labeled microtubules, imaged with confocal microscopy. (a) Cortical microtubules in root tissue. (b) Tobacco BY-2 cell line (courtesy Jan Vos, University of Wageningen, NL).

results achieved by the abundant experimental investigation on these arrays over the past twenty years as “stylized facts”. Borrowed from economics terminology, the term stylized fact normally refers to empirical regularities that describe the behavior of economic indicators. Stylized facts are usually formulated in terms of qualitative properties and focus on unifying traits, rather than on exceptions. Thus, the facts I will list are meant as general observations, some of which might not be true for all plant systems, or are open questions of the current scientific debate.

1. Cortical microtubules are confined in the thin ($200 - 500nm$ wide) region between the plasma membrane on one side and the vacuole on the other.
2. In the cortical array, the microtubules are mostly arranged transversely or obliquely to the cell elongation direction, which often coincides with the cell long axis. However, they are able to change their orientation in response to certain stimuli [25]. In non-elongating cells they are never transverse to the

2. Overview of the Problems

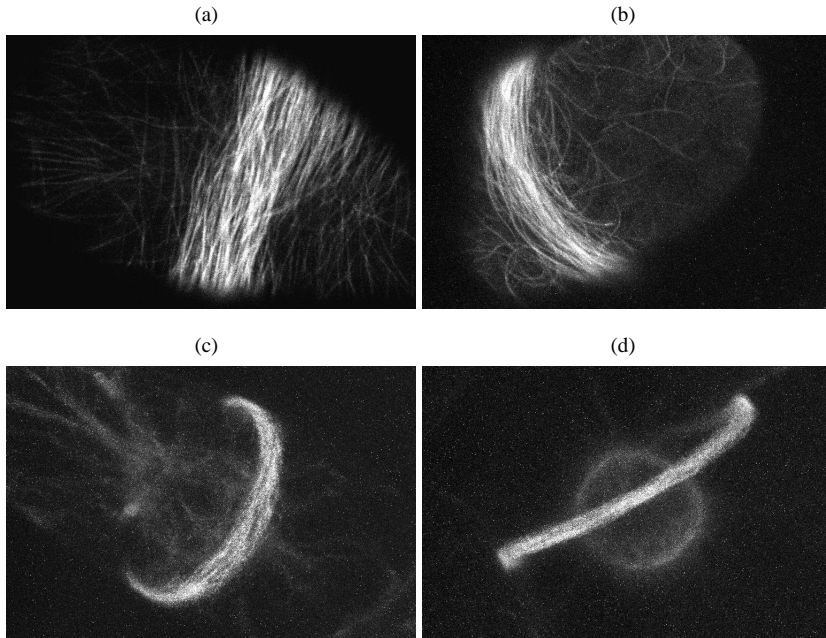


Figure 2.4.: Different stages in the formation of the preprophase band in tobacco BY-2 cells. Microtubules are labeled with the GFP-MBD microtubule binding domain, and imaged with confocal microscopy (Jan Vos, University of Wageningen, NL).

cell long axis but instead random, oblique, or longitudinal.

3. Evidence shows that that (a) microtubules are short compared to the cell size [26], and (b) form long bundles [27, 28, 24] by crosslinking.
4. In mid-interphase, microtubules often appear to form long coils, which seem to wind around the cell cortex as helices [29].
5. Microtubule organization can be regulated by various mechanisms, including tubulin tyrosination [30], and the protein MOR1 (Microtubule Organization-1) [31], and is gravitropic [32].
6. The problem of cortical microtubule organization may be connected with that of cell wall deposition [14, 15, 20]. The connection is not clear cut, however, as in many instances the two phenomena appear to be independent.
7. There is evidence that active processes such as treadmilling [33] and dynamic instability [19, 34] occur; the presence of motor proteins, but not their activity, has been reported in the arrays [35].

2.3. Scenarios

A complete explanation of the formation of the two arrays and their behavior, including the biological and the physical mechanisms involved, is lacking. However, the goal of providing a complete physical description of such processes is to date unrealistic. More modestly, my purpose in this thesis is to present self-contained physical scenarios for the system under investigation, with an eye to increasing the focus on topics and questions that can be addressed with further biological research. The scenarios presented here were explored with the tools of theoretical/computational modeling and *in vitro* experiments, in which the complex biological system is partially reconstructed in a controlled way starting from purified components. The advantage of this approach, which has revealed its usefulness in other instances [36, 37, 38], is that the experiment provides an intermediate description of the system, bridging the living system and the necessarily oversimplified mechanical theory.

The first scenario I will discuss (compatible with stylized facts (1) and (3a)), attempts to explain the alignment of the interphase array as a nematic effect between short microtubules confined in a quasi two-dimensional region. I will present this in chapter 3, starting from computer simulations of long thin hard spherocylinders in a narrow planar slit, which show a transition from the isotropic phase to a nematic phase with quasi-long-range orientational order upon increasing the density. The simulation results will be compared with data obtained from *in vitro* experiments where microtubules are confined in a thin slit, as well as from images of cortical microtubules interphase plant cells.

The second scenario, described in chapter 4, takes as a starting point the so-called “dynamic spring” hypothesis proposed by C. Lloyd and collaborators [39, 40] in the early eighties, which combines stylized facts (3),(4) and (7), in order to explain (2). According to this hypothesis (originally not formulated as a physical model), microtubules forming long coiling bundles are responsible for the arrangement and the orientation of the cortical interphase array. The length of these bundles is supposed to be regulated by the cell through an unspecified mechanism of active relative sliding. In other words, the organization of interphase microtubules is hypothetically caused by a passive coiling mechanism modulated by the active elongation of the bundles.

The third scenario (chapter 5) is dedicated to preprophase band formation. The underlying hypothesis is that (cf stylized fact (7)) an active drive provided by molecular motor complexes or other transport mechanisms, together with the geometrical constraints, are sufficient to organize the microtubules in a ring-like pattern. This hypothesis will be investigated mainly by means of theoretical tools, using a Landau-like mean-field approach for this kind of active, far-from-equilibrium systems, and then compared with more microscopic modeling and results from *in vivo* labeling of nascent preprophase band microtubules.

These scenarios were selected because of their approachability with a combination of theory and *in vitro* experiments, together with their appeal from the point of view of physics, as they are all essentially physical in nature (and have an inter-

2. Overview of the Problems

est independent from the biological inspiration). Needless to say, there are other possibilities, alternative or complementary to these scenarios, the main ones belonging to the class of pattern formation of chemical origin [41, 42]. According to this picture, extrinsic pattern-forming molecules could, using reaction-diffusion, directly or indirectly regulate dynamic instability, treadmilling, and in general the polymerization reaction of microtubules. Explanations of this kind should not be ruled out. Indeed, they have proved successful in simpler analogous systems such as the E. Coli MinCDE operon, responsible for the formation of a protein (FtsZ) ring before bacterial division [43, 44, 45], and in the regulation of the morphology of microtubules in some patterns used by animal cells [46]. Moreover, reaction-diffusion mechanisms have been suggested as a means of alignment and gravitropism for microtubules in solution [47, 48, 49]. I will devote more attention to the discussion of these alternative points of view when drawing some conclusions in chapter 6.

3. Microtubules Confined in a Quasi-Two-Dimensional Planar Geometry.

3.1. Introduction

In this chapter I will consider the working hypothesis that the confinement in a thin region, together with excluded volume effects, are sufficient to explain the alignment of microtubules in the cortical array as a Isotropic-Nematic (I-N) transition. This statement is inspired by stylized facts (1) and (3a) of Ch. 2. Cortical microtubules are confined in a thin region, whose thickness is 10-20 times a microtubule diameter. Additionally, since the microtubules are short, one can, to a first rough approximation, neglect the curvature of the region they are confined in. The consequences of this hypothesis will be tested by an in vitro experiment, where microtubules are confined in a thin flat region built in a microscope slide, combined with a computer simulation study of the phase behavior of a system of thin, hard spherocylinders undergoing a I-N transition confined between two parallel planar plates separated by small distances. The theoretical treatment contains two further assumptions: that the microtubules can be represented as rigid rods (and therefore their elasticity is neglected), and that they interact through a hard core potential (and therefore any further details in the interaction potential are irrelevant). The first of these facts is again justifiable with stylized fact (3a): the short length of microtubules, together with their high rigidity makes them stiff enough to be regarded as rigid. In a situation which is remotely realistic for a plant cell, this will be true provided the microtubules do not assemble in long linear bundles, which may be the case in the early stages of interphase. The second assumption is motivated by the fact that, due to screening and to absence of attraction forces, the interaction potential between microtubules can only be short-ranged repulsive.

The problem analyzed here has an interest independently from its original motivation. In fact, two-dimensional systems behave generically in a qualitatively distinct way from three-dimensional ones. In experiments, they are often not strictly confined to a mathematical surface, but also span a small region in the transverse dimension. A situation where two hard walls very close to each other confine the system occurs between the two extremes of bulk and two-dimensions, and, for this reason, is important to analyze. From this point of view, the question becomes to

3. *Microtubules Confined in a Quasi-Two-Dimensional Planar Geometry.*

explore this intermediate regime, and whether one can construct with microtubules a good model system for the quasi-two-dimensional regime of (broadly polydisperse) hard rods.

It is known [50, 51] that a system of hard needles or high (> 9) aspect ratio disco-rectangles (two-dimensional spherocylinders) in two dimensions exhibits, similarly to the xy -model, a nematic transition to quasi-long-range order of the Kosterlitz-Thouless kind [52]. The role of disclinations in this system has been investigated for different two-dimensional geometries [53]. In addition, density functional theory calculations show that the isotropic-nematic transition in two-dimensional dispersions of self-assembled or polydisperse needles is continuous [54]. A related problem is that of surface effects in presence of a single wall [55, 56, 57]. Several theoretical and simulation studies were focused on fluids of hard rods in contact with hard walls. Chen and Cui performed density functional theory calculations for a fluid of hard semiflexible polymers near a hard wall. They show a weakly first-order uniaxial to biaxial transition (signature of two dimensional ordering in the plane defined by the wall) at a bulk density far below that of the bulk I-N transition [58]. They also observe that the formation of a biaxial nematic film at the wall-isotropic fluid interface with the director parallel to the wall. The thickness of this film appears to diverge as bulk I-N coexistence is approached [58]. A surface induced continuous transition from a uniaxial to a biaxial phase prior to complete wetting was also predicted by density-functional theory of the Zwanzig model [57, 59, 60], in which the orientations of the particles are restricted to three orthogonal directions, and confirmed by simulations for freely rotating spherocylinders [57, 61]. Returning to the case of a fluid confined by two parallel hard walls, it was found by simulations of freely rotating spherocylinders [61] and by density functional theory calculations of the Zwanzig model [59] that the surface-induced uniaxial to biaxial transition is prior to a first-order capillary nematization transition at larger bulk densities, which terminates in a capillary critical point when the wall separation is about twice the length of the rods.

This chapter is organized as follows. In section 3.2 I present the theoretical and experimental model, and introduce the quantities that are measured, namely, the nematic order parameter in both experiment and simulation, and the orientational correlation function in the simulation only. In section 3.3, I present the theoretical results and discuss the *in vitro* experimental system and its connections with the simulation of broadly polydisperse rods on one side, and with the data on plant cell interphase cortical arrays on the other.

The main result from the simulation is that similarly to the strictly two-dimensional system, there is no true transition to long range order in the thermodynamic limit. A thickness-dependent transition to quasi-long range orientational order of the Kosterlitz and Thouless kind is present instead. This is in qualitative agreement with what is observed experimentally in a system of microtubules. On the other hand, the comparison with the *in vivo* system leads us to think that excluded volume effects may not be the most relevant feature for the ordering of interphase microtubules, although they shouldn't be disregarded, because microtubule density is certainly close to the onset of the nematic transition.

3.2. Methods

3.2.1. Simulation of a Fluid of Hard Spherocylinders Confined in a Quasi-Two-Dimensional Planar Slit

The model consists of a Monte-Carlo simulation for a fluid of hard spherocylinders with a (mean) length-to-diameter ratio $L/D = 320$, corresponding to microtubules of $8 \mu\text{m}$ in length and 25 nm in diameter, confined between two planar hard walls with an area of $L_x \times L_y$ in the $x - y$ plane at distance $h = H/D$ (measured in diameters) in the z direction (see Fig. 3.1). Periodic boundary conditions are employed in the x - and y -direction. The simulations were performed in the canonical ensemble, i.e. with fixed number of particles N , total volume $V = L_x L_y H$, and temperature T . The slit width h varies from 1 to 120. I consider both a system of monodisperse rods and a system of polydisperse rods with an exponential length distribution, which resembles closely the experiment with microtubules (see Section 3.3.3). The typical simulation time is about $2 \cdot 10^6$ Monte Carlo sweeps, where one sweep equals one attempted move per particle. More than 10^5 Monte Carlo sweeps were allowed for equilibration. The number of particles N in a simulation is up to 5000, although typically lower than 2000.

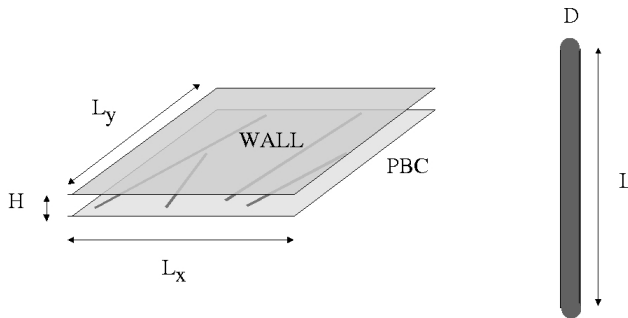


Figure 3.1.: A schematic picture of the system, which consists of a slit of thickness $h = H/D$, enclosed by two planar hard walls in the x - y plane with dimensions $L_x \times L_y$. A particle (spherocylinder) is described by a cylinder of length L and diameter D capped by two hemispheres of the same diameter. Periodic boundary conditions are applied laterally.

Different simulations were run, with varying density of the rods. For the monodis-

3. Microtubules Confined in a Quasi-Two-Dimensional Planar Geometry.

perse spherocylinders I considered the dimensionless density

$$C = \frac{N}{V}(L+D)^2D,$$

where N is the number of particles, $V = L_x L_y H$ is the total volume. For each value of the density, I measured the eigenvalues of the standard 3×3 nematic order-parameter tensor

$$Q_{\alpha\beta} = \left\langle \frac{1}{N} \sum_{i=1}^N \left(\frac{3}{2} u_{\alpha}^i u_{\beta}^i - \frac{\delta_{\alpha\beta}}{2} \right) \right\rangle,$$

where $\alpha, \beta = x, y, z$; u_{α}^i is the α component of the unit vector defining the orientation of particle i , and $\delta_{\alpha\beta}$ is Kronecker's delta. Diagonalizing $Q_{\alpha\beta}$ gives the orientational order parameters. As the typical cylindrical symmetry of the nematic state is broken a priori by the geometric constraints on the system, the most suitable order parameter Δ is proportional to the difference between the two highest eigenvalues of the average nematic tensor, normalized with a factor of $2/3$ to make it lie in the interval $[0, 1]$. It is easy to realize that when $h = 1$ this quantity reduces to the two-dimensional nematic order parameter [50] and for larger h it can be identified with the biaxial order parameter [57]. In fact, for $h = 1$, one of the three eigenvalues of Q will be $-1/2$ due to the geometric confinement, so that the submatrix defined by the other two eigenvalues will coincide with the exception of a constant factor with the two-dimensional nematic order parameter 2×2 tensor, and

$$\Delta \sim S = \left\langle \frac{1}{N} \sum_{i=1}^N \cos(2\theta_i) \right\rangle,$$

where θ_i is the planar smallest angle formed by the i -th particle with the nematic director, and S is the 2-dimensional orientational order parameter. Furthermore, it is possible to examine the density and orientational order parameter Δ profiles along the axis orthogonal to the walls. These are measured using bins with a typical width of about D , accumulated over the sweeps in the simulation [57]. Lastly, I measured the orientational correlation function

$$g_2(r) = \langle (\cos(\theta(0)) - \cos(\theta(r))) \rangle,$$

which describes the decay of the long wavelength fluctuations in the orientation.

3.2.2. In Vitro Confinement of Stabilized Microtubules in a Quasi-Two-Dimensional Planar Geometry

Tubulin and Microtubules

Tubulin was purified from pig brains as described in [37] and resuspended in MRB80 buffer (80 mM K-Pipes, 1 mM EGTA, 4 mM $MgCl_2$, pH 6.8). The protein concentration was measured by UV absorption. Rhodamine-labeled tubulin was purchased

lyophilized from Cytoskeleton (Denver, USA) and resuspended in MRB80. Microtubules were polymerized from free tubulin at 10 mg/ml, 1-3% rhodamine-labeled, with 5 mM GTP, incubating for 5 minutes at 30°C. They were then stabilized with 5 mM Taxol in MRB80.

Sample Preparation

Microscope coverslips were cleaned with chromosulfuric acid, sonicated in water, and rinsed in ethanol. Photoresist S1813 (purchased from Microresist, Germany) was spun on the samples to form a layer 1.2 μm thick. The samples were then illuminated with UV light through a quartz mask containing a chromium pattern of 100 μm thick parallel lines spaced 5 mm from each other. The patterns were developed, rinsed, and baked at 90°C for 1 hour. The samples were built by sealing a patterned coverslip with an agarose (1%) coated slide, and pushing with a standard weight for 10 minutes, so that the patterned lines acted as spacers to keep the wall separation at about 1 μm . Sample thickness was checked with confocal microscopy in a few cases. All the surfaces were coated by flowing a 2.5 mg/ml solution of casein dissolved in MRB80 to avoid aspecific binding of tubulin to the surfaces. After this step, taxol stabilized microtubules were flown in, at a concentration of 2-5 mg/ml, together with an oxygen scavenging system (75 mM glucose, 0.6 mg/ml glucose oxidase, 0.3 mg/ml catalase, 7mM dithiothreitol). The sample was pushed for 10 minutes after each flowing step and left under the weight for at least one hour afterwards before observation, to allow for relaxation of the microtubules. Such a sample can be observed for about 36 hours, before microtubules start to depolymerize.

Fluorescence Microscopy and Image Analysis

The samples were imaged with a Leica DM-IRB microscope, equipped with a 100W mercury lamp and a 100x oil immersion objective (N.A. 1.4). Conventional fluorescence images were taken using a KAPPA ccd device, connected to a computer and a S-VHS VCR. For quantitative measurement of local density and order parameter, we analyzed fluorescence images, tracking manually the profiles of individual microtubules using Bezier curves. With this procedure, it is possible to measure the local density of polymerized tubulin simply through the total length of microtubules in one field of view. Moreover, the order parameter tensor, or rather the entire orientational distribution function can be measured, knowing the equations of the interpolating Bezier lines, as describes in Appendix 3.A. As it is not possible to distinguish individual microtubule profiles at high density, I used an experiment where rhodamine-labeled and unlabeled microtubules were differentially mixed in such a way that only 1 filament out of 300 on average were fluorescently labeled.

3.3. Results

3.3.1. Simulation of Monodisperse Rods

Order Parameter and Size Effects

Fixing the lateral size $L_x = L_y = L_{xy}$ of the system, and measuring the order parameter Δ as a function of C , I find a transition to an ordered state for a density which depends slightly on h . Figure 3.2 shows a few typical snapshots of the fluid of spherocylinders for different densities of rods and a lateral view of the simulation box to illustrate its thickness. A transition from a uniaxial phase (in which the rods are randomly oriented in the xy plane) to a biaxial phase (where the rods have a preferred orientation in the xy plane) is apparent from visual analysis of these pictures.

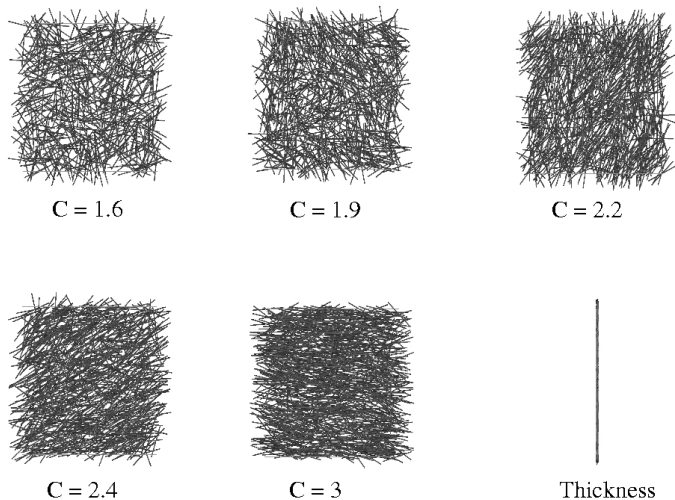


Figure 3.2.: Snapshots of the configuration of the system projected on the xy plane for different values of the dimensionless density $C = N/V(L+D)^2D$. Here $h = 20$, $L_{xy} = 1400D$, N varies from 600 to 1150 and the equilibration time is 10^6 sweeps. The diameters of the rods are not drawn to scale.

The order parameter and its profile along the z -axis as a function of density are plotted for a few examples in figure 3.3. I define arbitrarily the apparent transition density C_{trans} as the density at the intersection of the tangents constructed on the low density part and the linearly increasing part of $\Delta(C)$ at fixed density (see figure 3.3).

The apparent phase transition from a uniaxial to biaxial phase, however, depends in all instances on the lateral size of the system. In fact, the order parameter drops with increasing size at fixed C , in a way that the apparent transition

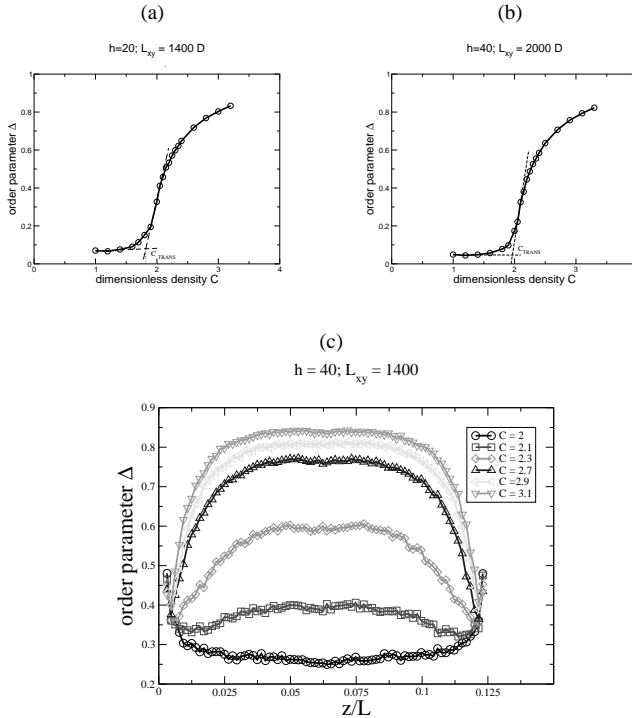


Figure 3.3.: (a) and (b). Order parameter Δ as a function of non-dimensional density for $L_{xy} = 1400D$. (a) $h = 20$ (b) $h = 40$. The transition density C_{trans} can be defined through the intersection of the tangents (dashed lines in (a) and (b)) constructed on the low density part and the linearly increasing part of the graphs. (c) z profile of the order parameter for $h = 40$, $L_{xy} = 1400D$ and increasing density.

density increases. I measured this effect consistently for different transverse sizes ($h = 5, 20, 40, 60$). Figure 3.4 reports an example for $h = 20$.

This fact gives a hint that, as in the strictly two-dimensional system, there could be no true phase transition in the thermodynamic limit, but a transition to quasi-long-range order. To establish this, it is necessary to test whether the orientational correlation function shows an algebraic decay (see below).

For comparison with real finite size systems it is interesting to look at the apparent transition density C_{trans} , at fixed lateral size L_{xy} , varying the small transverse size h . Two examples of the resulting phase diagrams are reported in figure 3.5. The transition density is roughly constant for thicknesses lower than $h = 15$ (see Fig. 3.5b) and increases almost linearly for thicker boxes (see Fig. 3.5a).

3. Microtubules Confined in a Quasi-Two-Dimensional Planar Geometry.

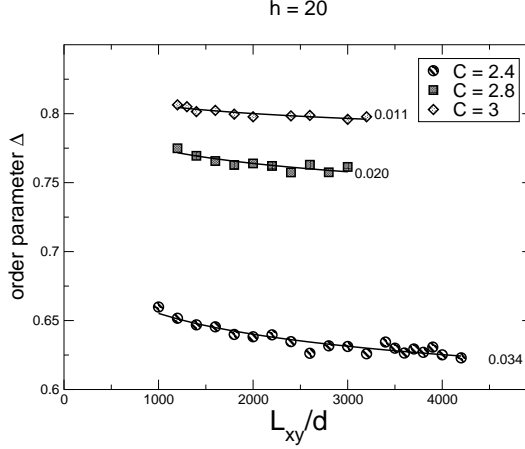


Figure 3.4.: Finite size effects in the measurement of the order parameter Δ . The graph shows the decay of Δ for three dimensionless densities as a function of the lateral size L_{xy} when the vertical size $h = 20$ is kept fixed. The numbers to the right of the curves are the exponent from power law fits. The decay of the order parameter for increasing size causes a shift in the apparent transition.

3.3.2. Correlation Function

As argued in the previous section, because of the finite size effects (decrease of Δ with increasing size), little can be concluded about the nature of the phase transition, or even its existence based on the measurements of the order parameter. These finite size effects, together with the presence of a phase transition to quasi-long-range order in the strictly two-dimensional system, make it sensible to investigate the decay of long wavelength orientational fluctuations. This is a delicate matter due to the very long relaxation times of these soft modes. I investigated the transition for integer values of h up to $h = 10$, with a simulation box having a lateral size $L_{xy} = 4000D$. Above this thickness, the number of particles was too high to achieve relaxation in reasonable times. In all these cases $g_2(r)$ showed a transition from exponential to power law decay with increasing density. One example, for $h = 6$, is plotted in figure 3.6. This transition does not depend on the size of the system, which just needs to be large enough so that the correlation of the modes is not affected by the periodic lateral boundary conditions.

From the above data, one can conclude that we are in presence of the same phase transition as in the two dimensional system of needles, described by the Frank elastic free energy,

$$F = \frac{1}{2}K \int (\nabla\theta(\mathbf{r}))^2 d\mathbf{r}.$$

Therefore, the transition density C_{trans}^{KS} can be set when the exponent of g_2 crosses

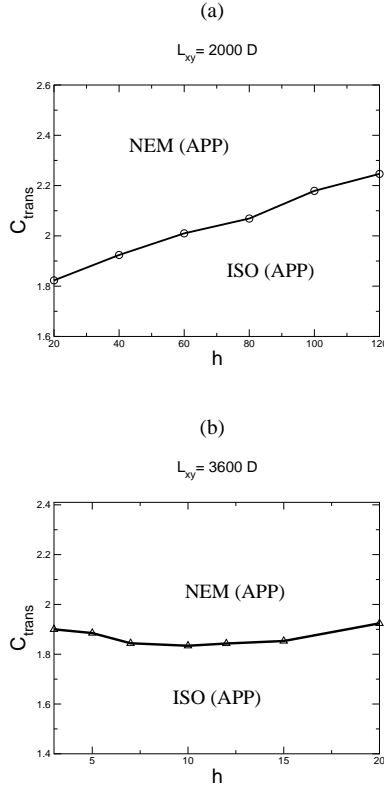


Figure 3.5.: Phase diagrams for the apparent nematic transition at fixed lateral size L_{xy} . The reduced uniaxial-biaxial transition density C_{trans} for different values of h . (a) Lateral size $L_{xy} = 2000D$, thickness from $h = 20$ up to $h = 120$; the number of particles N for these runs is up to 7000. (b) Lateral size $L_{xy} = 3600D$, thickness up to $h = 20$, N up to 6000. The two critical lines in (a) and (b) do not connect continuously at $h = 20$ because of the finite size effects.

1/4 [50]. Going to the limiting case $h = 1$, one can recover the fully two-dimensional system and compare the transition density with the one given in [50]. I measure a $C_{\text{trans}}^{KS}(h = 1) = 6.5$ which seems in good agreement with the 7.5 to 8 of Frenkel and Eppenga, considering the longer relaxation times we allow ($5 \cdot 10^5$ sweeps for up to 2600 particles). This value can also be compared with the 5.3 found in [51] for disco-rectangles with $L/D = 15$. The most interesting question, though, is how the transition density changes as a small lateral dimension is added. By a naive argument comparing the three-dimensional density C with the two dimensional one $C_{2d} = \frac{N}{L_x L_y} (L + D)^2$ one would expect to see a transition density which goes like $1/h$ so that the “effective” two-dimensional density is kept fixed. However, accord-

3. Microtubules Confined in a Quasi-Two-Dimensional Planar Geometry.

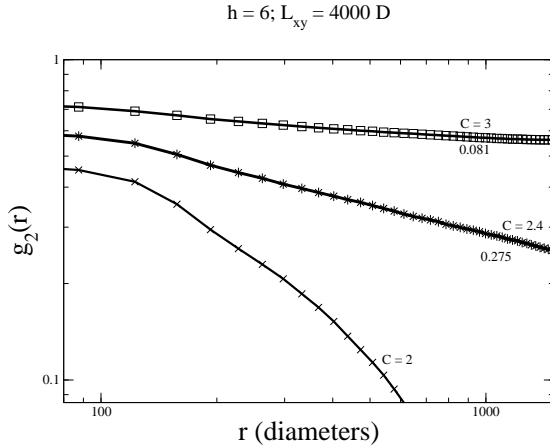


Figure 3.6.: Log-log plot of the orientational correlation function $g_2(r)$ for different values of the density, in the case $h = 6$. For low density this quantity has exponential decay, which becomes algebraic with increasing C . The numbers next to the curves indicate the decay exponents from power-law fits. By convention, the transition is defined to be where the exponent of the correlation function crosses $1/4$, in this instance around $C = 2.4$.

ing to the data, shown in Fig. 3.7, this decay is slower than this power law. We can try to understand this by a qualitative argument based on the fact that this two dimensional transition is mediated by defects. Adding a small transverse dimension, the liberty of effective overlaps given by the third degree of freedom makes it harder to form a disclination, so that a higher density than just h times the two-dimensional one is required to achieve the transition. This fact is illustrated in Fig. 3.8, which shows two typical xy -projections of the nematic states for $h = 1$ and $h = 3$. The configurations are qualitatively similar, but in the case $h = 3$ many effective overlaps are noticeable.

3.3.3. Experiment, Polydisperse Rods, and Comparisons

In the experiment, taxol stabilized microtubules are confined in a region with a thickness that is very small compared to their (mean) length and very large compared to their diameter. The sample consists of a microscope coverslip patterned with $1.2\mu m$ thick photoresist patterns used to maintain a constant separation with the microscope slide. The filaments are broadly polydisperse, typically showing an exponential distribution in length with an average aspect ratio of a few hundreds (figure 3.9). Their lengths do not vary in time due to stabilization with taxol [1].

To predict the experimental behavior of this system, I performed similar simu-

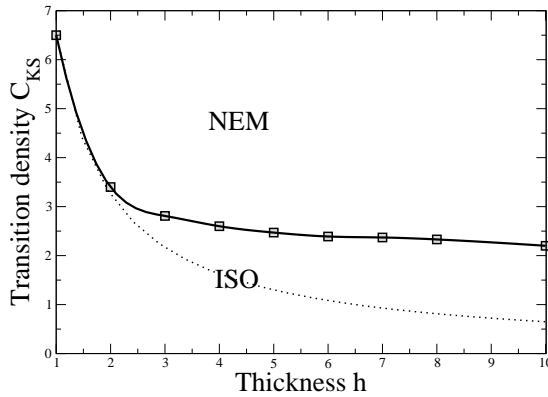


Figure 3.7.: Phase diagram for the nematic transition in quasi two dimensional geometry. The Kosterlitz-Thouless transition density C_{trans}^{KS} is plotted as a function of the system thickness h . Its decay is slower than the naively expected $1/h$ indicated by the dotted line.

lations for a set of polydisperse rods with an exponential length distribution. In the simulation of the polydisperse case, the apparent transition at fixed size is broader

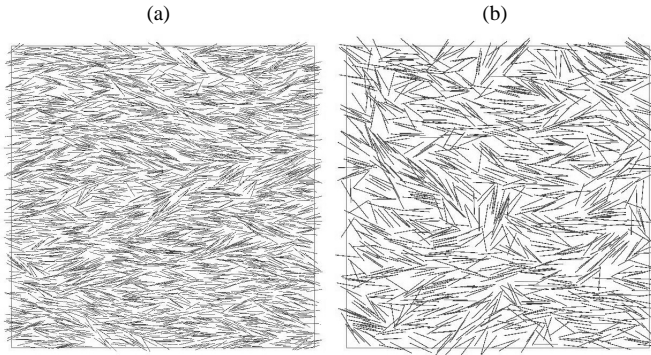


Figure 3.8.: Typical snapshots of configurations of two dimensional nematic-like phases. The pictures are projections of the configurations on the xy -plane. (a) 3074 particles in a slit with $h = 1$, $L_{xy} = 6000D$. The defects are noticeable in the picture. (b) 1150 particles in a slit with $h = 3$, $L_{xy} = 4000D$. Along with the defects, overlaps between projections of particles due to the transverse degrees of freedom are visible.

3. Microtubules Confined in a Quasi-Two-Dimensional Planar Geometry.

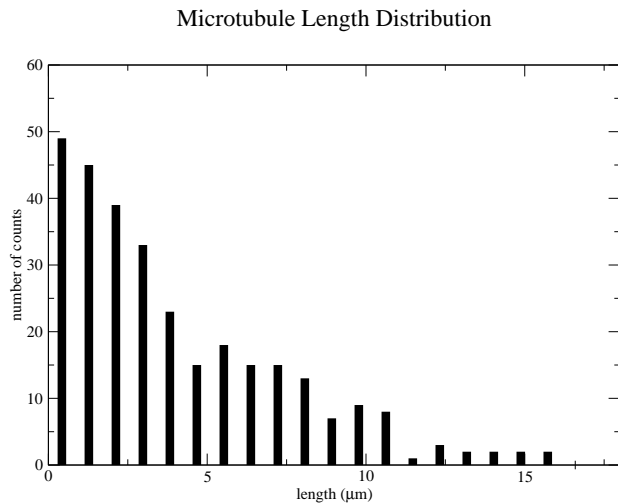


Figure 3.9.: Measured length distribution histogram for microtubule lengths in one experiment. The data are obtained from a set of fluorescence snapshots of the same experiment. The average length of the polymer is $5 \mu\text{m}$, corresponding to an aspect ratio of about 200.

than the one observed for the monodisperse system (figure 3.10) and its onset is at lower densities, due to the effect of long rods. Nevertheless, the qualitative behavior of the system is the same, with size effects and power-law decay in the correlation function. By measuring the total length of the rods in one box, knowing that the length of a tubulin dimer is 8 nm and that each polymer is composed of 13 protofilaments, one can predict the concentration of polymerized tubulin needed to have the ordering transition at a fixed size. The size of the system can be set as the field of view of the microscope, which is effectively the scale at which the experimental system is observed. With this identification, the apparent transition density, expressed in terms of tubulin concentration, falls in the experimentally accessible region of 2 to 5 mg/ml of (polymerized) tubulin.

To substantiate these observations, I measured order parameter and density by analyzing fluorescence images from the experiment (see Fig. 3.12). Quantitative work on the experimental system involves a few complications. First, the density of polymerized tubulin cannot be implied directly from the amount flown in the sample, due to density variations in different locations of the sample, which are due to compartmentalization caused by non-uniform coating, and to uncertainties in the ratio of polymerized to unpolymerized protein. Second, at high densities the order parameter cannot be immediately measured from image analysis because the individual rods cannot be distinguished from each other. This last problem can be bypassed using a partial labeling experiment, where rhodamine-labeled and unlabeled (stabilized) microtubules prepared in the same way are mixed in unequal proportions. Despite of these problems, the simulation results are qualitatively con-

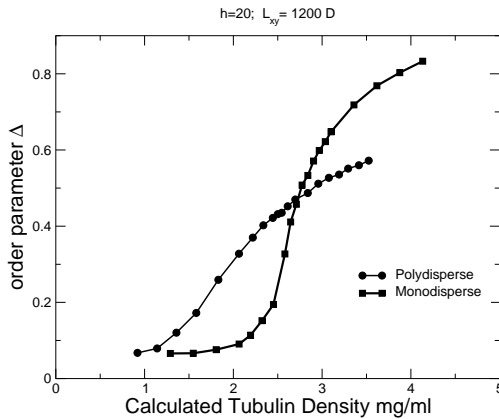


Figure 3.10.: Apparent transition predicted by the simulation in the exponentially polydisperse case for a fixed size $L_{xy} = 1200D$ compared to the (simulated) monodisperse system with the same mean aspect ratio (320). The order parameter is computed in the usual way. The simulated system size $L_{xy} = 1200D$ corresponds to a window of observation of $30 \times 30 \mu m$, which is comparable with that of a field of view of the microscope. The x-axis contains the calculated (polymerized) tubulin density computed from the total length of the rods in the simulation box, using the fact that $1 \mu m$ of polymer contains circa 1625 tubulin dimers, which in turn have a mass of about 100 kDa.

sistent with the experimental observations (see figure 3.11 as an illustration), as the ordering transition can be observed for increasing microtubule densities within the range predicted by the simulation. Furthermore, in the experiment, microtubules are observed to order in “patches” of tens of microns in size, which is consistent with the absence of true long range order predicted by the simulation. These patches have all possible orientations, indicating that the alignment is not purely due to the flow applied to the microtubule solution while inserting it in the sample, and that the system, despite the artificial density variations, is - at least locally, on a scale of a few hundred μm - relaxed.

To obtain the configuration of microtubules from a snapshot, I tracked the filaments manually, using Bezier interpolating curves. From this information it is immediate to compute tubulin density from the total polymer length, as done with the simulation. The procedure we adopt to measure the order parameter is outlined in Appendix 3.A (the reader can refer to the thesis of Catalin Tanase [62] for more details). The measurement of microtubule density and order parameter across single fields of view should compare directly with the results obtained from the simulations on a box of the same scale. A comparison of this kind is shown

3. Microtubules Confined in a Quasi-Two-Dimensional Planar Geometry.

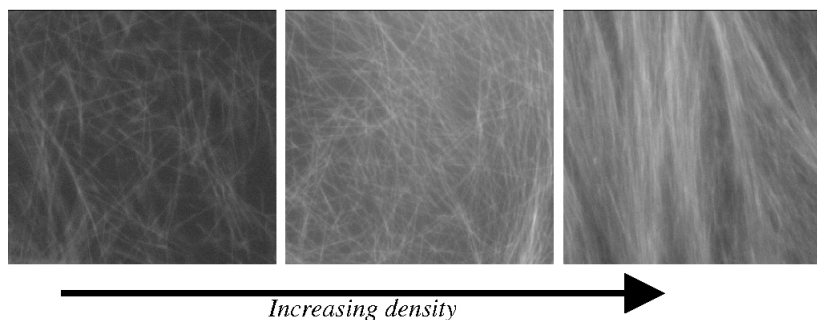


Figure 3.11.: Snapshots from the experiment. The microtubules, confined in $1\ \mu\text{m}$ thick microscope slides, are imaged with fluorescence microscopy, the pictures show one field of view, sized $40\times 30\ \mu\text{m}$, corresponding to a magnification of 100x. The concentration range of polymerized protein is estimated to be 2-4 mg/ml. The rods are observed to align for increasing densities on scales from 30 to $100\ \mu\text{m}$. On larger scales, patches of aligned rods with different orientation are noticeable. The local density of tubulin cannot be measured directly, but can be estimated comparatively from the average pixel intensity in the images after subtracting the background, provided that the settings of the ccd camera are fixed. In the above figure, starting from the left, the second snapshot is approximately 1.5 times denser than the first, while the third is twice as dense as the second.

in Fig. 3.13. Looking at this graph, the correlation between density and order parameter seems to be present in the experiment, with a transition density which lies roughly in the range indicated by simulations. The high density points in the graph correspond to two partial labeling experiments, where fluorescently labeled polymers are mixed with unlabeled ones and used as tracers, in a way that only $1/300$ in length of the microtubules are visible. Since the number of traced microtubules in one snapshot remains roughly constant, for these high density points the absolute error on the estimated density is about two orders of magnitude greater than for the low density set. Other sources of experimental error are resolution of fluorescence, manual tracking, small number of filaments for the averaging. Different images may have slightly different densities (because they come from different areas of the sample). Therefore this comparison has to be regarded as a qualitative one, which anyway gives confirmation of what is predicted by the simulation.

The same tracking procedure can be carried out using images of microtubules in the interphase cortical arrays of plant cells. Thus, we can compare directly the *in vitro* data with information extracted in the same way from fluorescence images of GFP labeled cortical microtubules in Tobacco BY-2 cell lines. This was done in

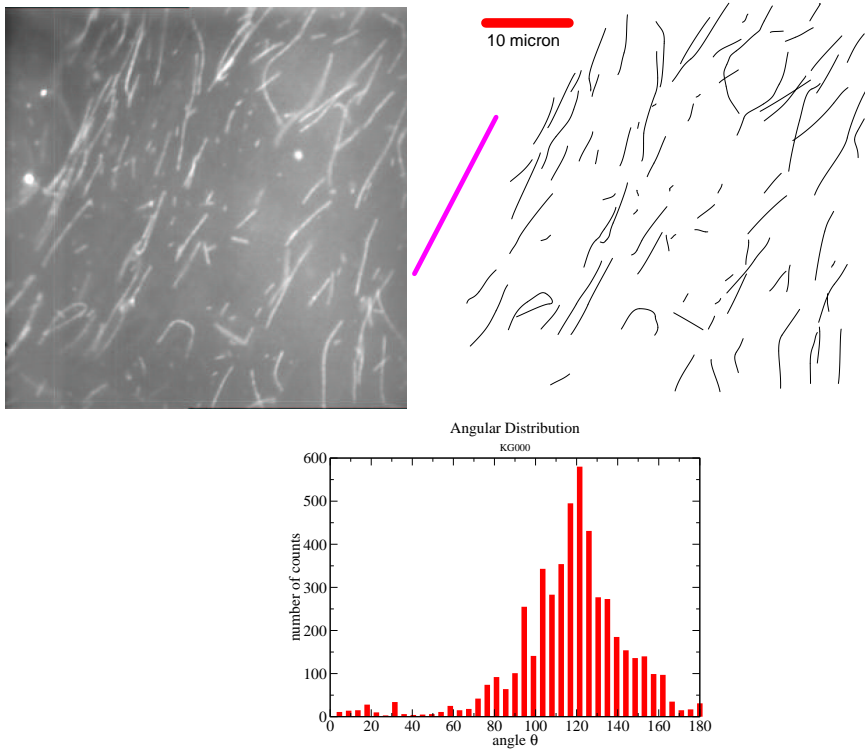


Figure 3.12.: Example of data analysis from a partial labeling experiment. Upper left: original fluorescence image, where only 1/300 (in length) microtubules are labeled. Upper right: Manual tracking of microtubules, the nematic director is plotted on the left, and the scalebar in the upper left corner corresponds to 10 μm . Lower panel: orientational distribution function histogram. The order parameter is $S = 0.77$.

3. Microtubules Confined in a Quasi-Two-Dimensional Planar Geometry.

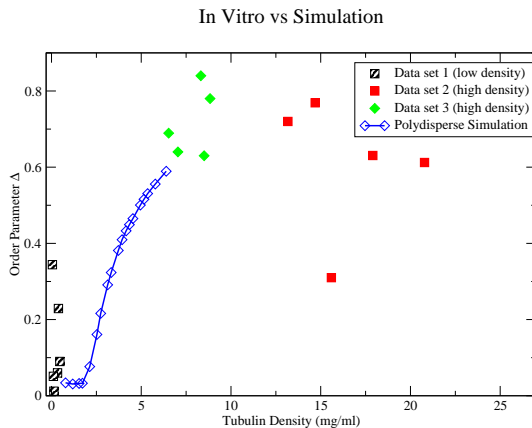


Figure 3.13.: Experimental data, compared with data from the simulation of polydisperse rods. In the experiment the observation scale is 55×45 or $40 \times 30 \mu m$. In the simulation the rods have an exponential length distribution with an average length of $5 \mu m$ and the box dimensions are $h = 40$, $L_{xy} = 1400D$, corresponding to the geometry and observation scale in the experiment.

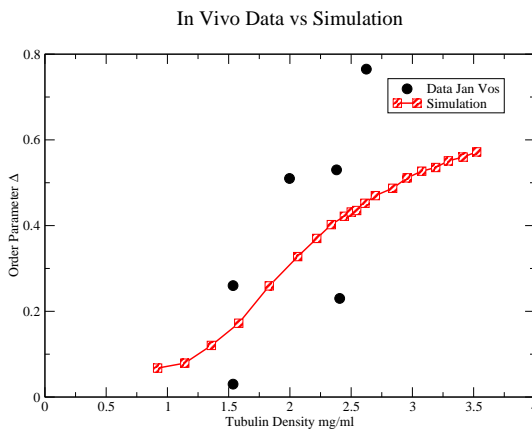


Figure 3.14.: Graph of order parameter vs density. Comparison of plant data (BY2 cell line) with simulations. To compute the density, a thickness of $200 nm$ was assumed. The original images (Jan Vos) have a scale of about $20 \times 20 \mu m$. The length distribution of cortical microtubules is not known. In the simulation I used an exponential length distribution for the rods with average length of $5 \mu m$ and the box dimensions are $h = 10$, $L_{xy} = 1400D$. The data on plant cells were provided by Jan Vos, Wageningen University.

a few cases and the results are shown in Fig. 3.14. The measurement error on the data points shown should be smaller than that from the *in vitro* experiment because the number of tracked filaments is higher. These data are subject to an uncertainty in the density because the thickness of the layer where the plant microtubules are confined is not known exactly. I assumed a value of 200 nm. With this thickness, the density appears to be in the range of the onset of the apparent isotropic-nematic transition on this scale. On the other hand, because of the lack of data, it is not possible to establish a clear correlation, or a lack thereof, between density and order parameter. However, it appears that in the few instances analyzed the ordering in the *in vivo* system at a fixed density roughly corresponds to that expected from the apparent nematic transition. Varying the thickness from 200 to 500 nm does not affect this observation.

3.4. Discussion and Conclusions

I will divide the conclusions in general ones for a system of confined rods, and more specific ones for the problem of microtubule organization in interphase plant cells.

Focusing on the generic aspects of the nematic transition in a quasi- two-dimensional system, the main result is that a transition to long-range-order is absent in the thermodynamic limit. Instead, a Kosterlitz-Thouless-like transition is present, revealed by the algebraic decay of the orientational correlation function. This has some interesting general consequences. First of all, it indicates that a system with some small transverse third dimension will maintain the same qualitative behavior as a true two-dimensional one. Secondly, the slower decrease of the Kosterlitz-Thouless transition with increasing plate separations for the 2D-like isotropic-nematic transition indicates that there is an important role played by the transverse degree of freedom in the elimination of disclinations. Possible future work in this direction includes investigating in more detail the crossover between two- and three-dimensional behavior, exploring slit thicknesses that are comparable with the length of the rods. This kind of work would require using spherocylinders with a lower aspect ratio, to keep the number of particles, and therefore the computational cost, reasonably low. One possibility is that the Kosterlitz-Thouless transition in the strictly two-dimensional and quasi-two-dimensional system ends in the previously observed wall-induced uniaxial to biaxial transition [57] at larger plate separation. If this would be true, this transition would not be connected to capillary nematization (a transition from a biaxial to a condensed nematic phase), which terminates in a critical point at a fixed plate separation [59].

Turning our attention to microtubules, the simulation appears to be in qualitative agreement with what is observed in the *in vitro*, broadly polydisperse system, for which I could estimate quantitatively density and ordering through image analysis. This indicates that, at least for our scopes, the model of a microtubule as a hard-rod is sufficiently good to grasp the basic features of the *in vitro* system.

Comparing these results with the same analysis carried out for plant cells should

3. Microtubules Confined in a Quasi-Two-Dimensional Planar Geometry.

in principle lead to considerations of some biological relevance. However, one should be fairly cautious on this point, for two basic reasons. First, the experimental and the theoretical model, compared to the plant system, make rather crude approximations that have to be considered. In the experiment, the curvature of the confining surface is absent; in the model, both this curvature and microtubule elasticity are disregarded. Second, the data in our possession are hardly sufficient for clear-cut conclusions. Assuming that the microtubules do not arrange themselves into long coils by crosslinking, which may be true in the early stages of interphase, it remains a doubt on the polymers average length and length distribution in a plant cell, which are not known. The only study that investigates them systematically [26] is rather old and indicates an average length of about $3 \mu\text{m}$. The importance of curvature and microtubule elasticity strictly depends on how long microtubules are. However, on the basis of energy minimization, one would expect that, because of these features, any alignment would be favored along the elongation axis of the cell, which has lower curvature, rather than transversely or oblique, as observed in a plant cell.

What we can say here is that, under our assumptions, the density of cortical microtubules in plant cells appears to be close to the onset of an apparent nematic transition on the scale of observation, so that excluded volume effects may play some role. The available data points from the analysis of the orientation of fluorescently labeled cortical microtubules indicate alignment for plant microtubules where expected from the simulated nematic transition. However, the data are too scarce to correlate density with ordering, so this correspondence could be merely coincidental. It appears then plausible that excluded volume is not the most relevant feature of the system, and other processes play a more important role than volume exclusion. In other words, although the results are not sufficient to completely discard the working hypothesis of a nematic transition for cortical microtubules in plant cells, which could be tested with more stringent *in vivo* experiments, they put under discussion whether the model considered in this chapter is the most appropriate to describe the system and includes all the necessary features.

3.A. Computing Orientational Order for a Collection of Bezier Curves

In this appendix I will describe the procedure adopted to compute the order parameter by interpolating with Bezier curves the configurations of microtubules in a fluorescence snapshot. Let us consider a collection of these Bezier curves. The goal is to determine an orientational order parameter or rather a full orientational distribution function for this collection. Consider first a single filament of length L . The orientational distribution function for this filament is given by

$$f(\varphi) = \frac{1}{L} \int_0^L ds \delta(\varphi - \varphi(s)), \quad (3.1)$$

3.A. Computing Orientational Order for a Collection of Bezier Curves

where s is the arclength parameter of the curve and $\varphi(s)$ is the local angle it forms with an arbitrary oriented axis in the plane. If we denote the curve by $\{\mathbf{r}(s) | s \in [0, L]\}$ and the unit vector along the reference axis by $\hat{\mathbf{x}}$ the angle is defined by $\cos \varphi(s) = \dot{\mathbf{r}}(s) \cdot \hat{\mathbf{x}}$ where the dot denotes the derivative $\frac{d}{ds}$ with respect to the arclength. Note that because of the arclength parametrization $|\dot{\mathbf{r}}(s)| = 1$. The arclength along an arbitrarily parametrized curve is given by

$$s(t) = \int_0^t dt' \left| \frac{d\mathbf{r}}{dt}(t') \right|. \quad (3.2)$$

Furthermore,

$$\dot{\mathbf{r}}(s) = \frac{d\mathbf{r}}{dt}(t(s)) \frac{dt(s)}{ds} = \left| \frac{d\mathbf{r}}{dt}(t(s)) \right|^{-1} \frac{d\mathbf{r}}{dt}(t(s)). \quad (3.3)$$

This allows to write Eq. (3.1) as

$$f(\varphi) = \frac{\int_0^1 dt \left| \frac{d\mathbf{r}}{dt} \right| \delta\left(\varphi - \arccos \frac{\frac{d\mathbf{r}}{dt} \cdot \hat{\mathbf{x}}}{\left| \frac{d\mathbf{r}}{dt} \right|}\right)}{\int_0^1 dt \left| \frac{d\mathbf{r}}{dt} \right|}. \quad (3.4)$$

The information in the orientational distribution function is more readily extracted from the moments

$$c_k = \langle \cos k\varphi \rangle = \int_0^{2\pi} d\varphi \cos k\varphi f(\varphi). \quad (3.5)$$

Since the filaments do not possess intrinsic orientation we are at liberty to assign either end as origin. The reparametrization $s \rightarrow L - s$ leads to $\varphi(s) \rightarrow (\varphi(s) + \pi) \bmod_{2\pi}$. Invariance under this transformation implies $c_{2k+1} = 0$ for all k . The explicit form of the moments is

$$c_k = \frac{\int_0^1 dt \left| \frac{d\mathbf{r}}{dt} \right| \cos\left(k \arccos \frac{\frac{d\mathbf{r}}{dt} \cdot \hat{\mathbf{x}}}{\left| \frac{d\mathbf{r}}{dt} \right|}\right)}{\int_0^1 dt \left| \frac{d\mathbf{r}}{dt} \right|}. \quad (3.6)$$

Reduction of the integrand through trigonometric multiple angle formulas leads to the consideration of the integrals

$$d_n = \frac{\int_0^1 dt \left| \frac{d\mathbf{r}}{dt} \right| \left(\frac{\frac{d\mathbf{r}}{dt} \cdot \hat{\mathbf{x}}}{\left| \frac{d\mathbf{r}}{dt} \right|} \right)^n}{\int_0^1 dt \left| \frac{d\mathbf{r}}{dt} \right|}. \quad (3.7)$$

A Bezier curve has the standard parametrization

$$\mathbf{r}(t) = \mathbf{r}_0 + \mathbf{r}_1 t + \mathbf{r}_2 t^2 + \mathbf{r}_3 t^3, \quad (3.8)$$

where $t \in [0, 1]$. The following "special" points are associated with it

$$\begin{aligned} \mathbf{r}_A &= \mathbf{r}_0 = \mathbf{r}(0) \\ \mathbf{r}_B &= \mathbf{r}_0 + \frac{1}{3}\mathbf{r}_1 \\ \mathbf{r}_C &= \mathbf{r}_0 + \frac{2}{3}\mathbf{r}_1 + \frac{1}{3}\mathbf{r}_2 \\ \mathbf{r}_D &= \mathbf{r}_0 + \mathbf{r}_1 + \mathbf{r}_2 + \mathbf{r}_3 = \mathbf{r}(1), \end{aligned} \quad (3.9)$$

3. Microtubules Confined in a Quasi-Two-Dimensional Planar Geometry.

or equivalently

$$\begin{aligned}\mathbf{r}_0 &= \mathbf{r}_A \\ \mathbf{r}_1 &= 3(\mathbf{r}_B - \mathbf{r}_A) \\ \mathbf{r}_2 &= 3(\mathbf{r}_C - 2\mathbf{r}_B + \mathbf{r}_A) \\ \mathbf{r}_3 &= \mathbf{r}_D - 3(\mathbf{r}_C - \mathbf{r}_B) - \mathbf{r}_A.\end{aligned}\quad (3.10)$$

We have therefore

$$\frac{d\mathbf{r}}{dt} = \mathbf{r}_1 + 2\mathbf{r}_2 t + 3\mathbf{r}_3 t^2, \quad (3.11)$$

so that

$$\left| \frac{d\mathbf{r}}{dt} \right|^2 = q_0 + q_1 t + q_2 t^2 + q_3 t^3 + q_4 t^4 \equiv Q(t), \quad (3.12)$$

with

$$\begin{aligned}q_0 &= \mathbf{r}_1 \cdot \mathbf{r}_1 \\ q_1 &= 4(\mathbf{r}_1 \cdot \mathbf{r}_2) \\ q_2 &= 6(\mathbf{r}_1 \cdot \mathbf{r}_3) + 4(\mathbf{r}_2 \cdot \mathbf{r}_2) \\ q_3 &= 12(\mathbf{r}_2 \cdot \mathbf{r}_3) \\ q_4 &= 9(\mathbf{r}_3 \cdot \mathbf{r}_3).\end{aligned}\quad (3.13)$$

If we define

$$\frac{d\mathbf{r}}{dt} \cdot \hat{\mathbf{x}} = \mathbf{r}_1 \cdot \hat{\mathbf{x}} + 2(\mathbf{r}_2 \cdot \hat{\mathbf{x}})t + 3(\mathbf{r}_3 \cdot \hat{\mathbf{x}})t^2 = P(t), \quad (3.14)$$

the integrals d_{2l} are concisely written as

$$d_{2l} = \frac{\int_0^1 dt \frac{P(t)}{\sqrt{Q(t)}^{2l-1}}}{\int_0^1 dt \sqrt{Q(t)}}. \quad (3.15)$$

These integrals are either evaluated numerically or using reduction to standard Elliptic integrals. In Postscript file formats the Bezier curves are represented by the construct

```
xA yA m(oveto)
xB yB xC yC xD yD c(urveto) ,
```

where the labeling is the same as in Eq. (3.9).

Dealing with an ensemble of N filaments, the proper choice for the distribution function is

$$f(\varphi) = \frac{\sum_{i=1}^N \int_0^1 dt \left| \frac{d\mathbf{r}_i}{dt} \right| \delta \left(\varphi - \arccos \left| \frac{\frac{d\mathbf{r}_i}{dt} \cdot \hat{\mathbf{x}}}{\left| \frac{d\mathbf{r}_i}{dt} \right|} \right)}{\sum_{i=1}^N \int_0^1 dt \left| \frac{d\mathbf{r}_i}{dt} \right|}. \quad (3.16)$$

This form correctly weighs each filament with its length, so that each stretch of filament contributes equally to the total order.

4. Coiling of Microtubules Confined in Box-like chambers

4.1. Introduction

This chapter focuses on the scenario for the cortical array which takes as a starting point the “dynamic spring” hypothesis proposed by C. Lloyd and collaborators [39, 40] in the early eighties. According to this hypothesis, microtubules forming long coiling bundles, whose length is regulated by the cell through an unspecified mechanism of active relative sliding, are responsible for the transverse arrangement and the reorientation of the cortical interphase array. Although this hypothesis is not originally formulated as a physical model, from our point of view we can say it combines stylized facts (3),(4) and (7) of chapter 2, to explain stylized fact (2). In other words, the apparent orientation of interphase microtubules is supposed to be caused by a passive coiling mechanism in combination with the active elongation of the bundles. Formulated in this way, the dynamic spring hypothesis can be investigated using physical methods.

The approach I will take to test the implications of the hypothesis combines a simple analytical treatment, where one bundle is modeled as a flexible inextensible filament confined on a two dimensional surface, with experiments, where microtubules are grown *in vitro* from nucleation seeds in microfabricated chambers. The chambers have similar sizes and aspect ratios as a typical plant cell. In other words, the model system for an elongating bundle of microtubules in a plant cell is a microtubule polymerizing from a nucleation seed in a microfabricated chamber, which, in turn, is described theoretically as an unstretchable filament with bending elasticity confined on a two-dimensional surface. The elongation of a filament caused by polymerization replaces the hypothetical active sliding mechanism between microtubules which causes the elongation of bundles *in vivo* according to the dynamic spring hypothesis. The nucleation seeds play the role of microtubule nucleation agents present in the cell. This physical model is bound to a number of assumptions and simplifications on the nature of the coiling bundle, its physical properties and elongation mechanism. The implications of these choices will be discussed along with the results (section 4.3) and in the conclusions (section 4.4). The chapter starts with an introduction of the methods (section 4.2), after which I present the results (section 4.3). The theoretical predictions are presented first, with the aim of establishing the correct conceptual framework for the experiment. The conclusions are contained in section 4.4.

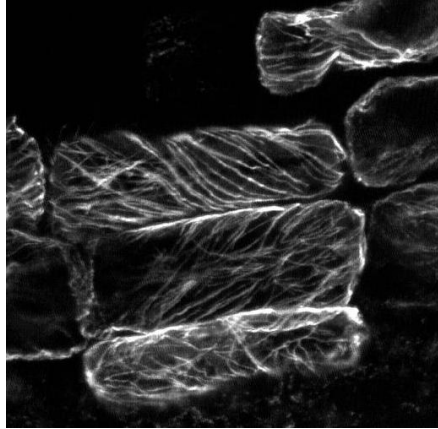


Figure 4.1.: Example of apparent coiling microtubule bundles. Parenchyma cells in the elongating part of a flax stem showing arrays of cortical microtubules labeled with Mouse monoclonal anti α -tubulin and Goat anti Mouse Alexa/488, after enzymatic digestion of cell walls with Macerozyme and cellulase Onozuka R-10. Courtesy André van Lammeren, Henk Kieft, Beata Petrovska (Plant cell Biology, Wageningen University and Research Center).

4.2. Materials and Methods

4.2.1. Theory

Model

The representation of a microtubule, or a bundle, is a filament having length L , whose shape is described by a curve $\mathbf{r}(s)$, assigning a point in space for any value of the arclength parameter s . A given shape corresponds to a single configuration. In the model, the functional

$$E[\mathbf{r}(s)] = \frac{1}{2}k \int_0^L C(s)^2 ds \quad (4.1)$$

specifies the value of the bending energy. Here, $C(s) = \left(\frac{\partial^2 \mathbf{r}}{\partial s^2}\right)$ is the local curvature and k the bending rigidity of a (bundle of) microtubule(s). In the model the value of k is considered as a fixed parameter. Furthermore, I impose the condition that a microtubule is, to a first approximation, unstretchable.

Energy Estimate for Longitudinal vs Transverse Helical Coiling

A first question relevant for the plant system and the *in vitro* experiment is which way is energetically favored for the filament to wrap around the confining surface

(cf. Fig. 4.6b). To estimate which orientation is favored in a plant-cell geometry, I compare the energy of two families of configurations, which can be called “transverse” and “longitudinal”. In doing this I impose both the shape of the filament and that of the confining surface, and then calculate the corresponding energies and compare them.

This is done in a first instance neglecting the caps. For the transverse helix, I use a cylinder with a larger height than its base diameter. For the longitudinal helix I consider a generalized cylinder with elliptical, or rectangular with rounded edges, base.

This last case (Fig 4.2) is particularly simple to tackle analytically, as the helix on the cylinder has constant curvature, and the curve on the generalized cylinder is (univocally) constructed by piecewise connection of straight (zero curvature) lines on the sides and a helix on the edges.

In figure 4.2 the size of the confining surface is $2R \times 2R \times 2D$, where $D > R$ (the box is elongated), and, calling L the filament length, $L > 2D$ (necessary geometrical condition for the filament to be able to form a helix). The result for the ratio of E_{long} , the energy of a longitudinal coil, to E_{trans} , the energy of a transverse one, can be easily computed as

$$\frac{E_{\text{long}}}{E_{\text{trans}}} = \frac{R}{R + \frac{2}{\pi}(D - R)} \left(\frac{L^2 - 2R^2}{L^2 - 2D^2} \right)^2,$$

which leads to the plot in figure 4.6. This calculation can be repeated numerically and considering closed surfaces (i.e. adding the caps). For example, a cylinder with semi-spherical caps, a parallelepiped with rounded edges, and an ellipsoid, yield very slight variations in the result.

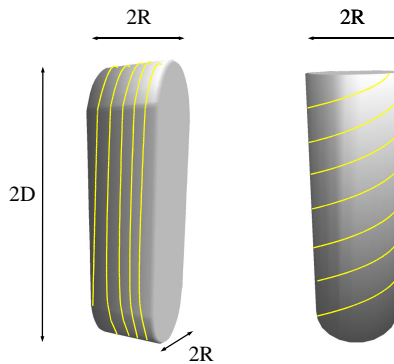


Figure 4.2.: Example of geometry used for the energy estimate, using a cylinder (right panel) and a generalized cylinder with rectangular base and round edges (left panel). To compare the two geometries, both their dimensions, R and D , and the filament length L have to be equal.

Minimum Energy Configuration for a Filament in a Confined Cylinder

A further step in the model is to determine whether a helix is indeed the minimum elastic energy configuration to be expected for a coil. To find the minimum energy configuration for a fixed shape of the confining surface, one must evaluate the functional 4.1 over the set of all possible configurations of the filament. The favored configuration is the one that minimizes elastic energy, i.e. for which

$$\delta E = 0.$$

For a filament on a cylinder without caps (such as the one in the right panel of figure 4.2, this leads to the Euler-Lagrange equation

$$\ddot{\gamma}(s) + 2 \cos^3 \gamma(s) \sin \gamma(s) = 0 ,$$

where $\gamma(s)$ is the angle between the tangent vector $\mathbf{t} = d\mathbf{r}/ds$ of the filament and the horizontal axis, defined by the unit vector $\hat{\mathbf{e}}_\varphi$ associated to the angular cylindrical coordinate φ (cf. the thesis of Catalin Tanase [62] for an explicit derivation of this equation). This equation is formally very similar to that of a pendulum, and yields the confined solutions shown in figure 4.7b. Only by applying an external force can a helix be obtained as a solution. For further details on these calculations the reader is referred to the thesis of Catalin Tanase [62]. Knowing the solution for the cylinder without caps also allows to compute the minimum energy configuration of an elastic filament confined on a spherocylinder, by patching the solution on the sphere (which has constant curvature) and that of the cylinder (see Fig. 4.8).

4.2.2. Experiment

Microfabricated Chambers

Microscope coverslips were kept for one day in cromosulfuric acid mixture, then rinsed in water and in a 2M solution of KOH in ETOH. After being rinsed again in water, they were sonicated three times for 10 min in water, rinsed in ethanol, and dried in an oven at 100°C. Photoresist SU-8 (purchased from Microresist, Germany) was spun on the samples in layers of 25 or 40 μm , which, after a pre-exposure bake (on a hot plate. 4 minutes at 60°C, 16 minutes at 90°C) were illuminated with UV light at 1.75mW/cm² through a quartz mask with chromium patterns, consisting of arrays of rectangles and ellipsoids, 25x35 or 40x80 μm in size. The patterns were developed for five minutes in Microresist SU-8 developer, rinsed and hard baked (in the oven, for 30 minutes at 120°C). The size of the chambers was chosen according to a prior determination of the size of barrel shaped, non-tip, Tradescantia Virginiana stamen hair cells made by Jan Vos (Wageningen University). These data were not divided according to the cell cycle state (cells just before division are larger than ones that have just finished division). For the cell diameter he found a mean value of 25.7 μm (standard deviation 1.7 μm) ranging from a minimum value of 22.7 μm to a maximum of 30.5 μm . For the cell length the mean value was 35.9 μm (standard deviation 6.4 μm), with minimal value 18.4 μm

and maximal value $48.7 \mu\text{m}$. The surfaces to seal the microfabricated chambers were made from silicon rubber PDMS (polydimethylsiloxane). The silicone elastomer precursor and a curing agent (Dow Corning Sylgard 184) were mixed in a 10/1 weight ratio, and brought under a low atmospheric pressure with a small vacuum pump (Laboport) for 15 minutes in order to remove air bubbles. A uniform layer about 2 mm thick was obtained by pouring the mix of on top of plastic (flexible) sheets, which were then baked at 100°C for one hour for crosslinking to occur. The resulting rubber-like sheet was cut in circular discs. Patterned coverslips and PDMS discs were cleaned by sonicating subsequently in ethanol, in water with 5%, and water, each step lasting one minute.

Microtubule Nucleation Seeds

Nucleation seeds were grown from free tubulin (purified as described in section 3.2) at 5 mg/ml in MRB80 with 2 mM GMPCPP, incubating for 45 minutes at 35°C . The batch of GMPCPP was generously provided by Tim Mitchison (Harvard Medical School, USA). The seeds were extended with 20%-rhodamine labeled 0.4 mg/ml tubulin tips polymerized with 0.5 mM GTP, for ease of localization, and then immediately flash-frozen in liquid nitrogen to keep the extensions stable.

Sample Preparation

All the surfaces were coated through incubation with a 2.5 mg/ml solution of casein dissolved in MRB80 to avoid aspecific binding of tubulin to the box walls, then dried with nitrogen. After this step, (a) the nucleation seeds in MRB80 and (b) a solution of 1 mg/ml tubulin (10% rhodamine labeled) with 2.5 mM GTP, an oxygen scavenging system (75 mM glucose, 0.6 mg/ml glucose oxidase, 0.3 mg/ml catalase, 7mM dithiothreitol) were introduced in the sample in two separate steps on a cold block, with intermediate incubations in a low-vacuum chamber to avoid the trapping of air bubbles in the chambers. After each incubation, the excess fluid on top of the sample was removed by pipette suction, to avoid as much as possible tubulin dilution.

The chambers were sealed with PDMS discs, which were built in a slide with a circular hole as illustrated in figure 4.3. By using a solution of core-shell fluorescent (FITC) silica beads ($1\mu\text{m}$ diameter) in water, it was possible to test that the chambers were filled and sealed. The beads were imaged with fluorescence microscopy.

Fluorescence and Confocal Microscopy. Image reconstruction.

The samples were imaged from the side of the patterned coverslip, using a Leica TCS-SP2 confocal microscope and a Leica DM-IRB microscope with a 100W mercury lamp. Oil immersion objectives (N.A. 1.4, 63x magnification for confocal, 100x for conventional fluorescence) were employed.

To reconstruct the shape of the polymerized microtubules, I acquired z-stacks of images and analyzed them. Due to the scattering from the walls there was a

4. Coiling of Microtubules Confined in Box-like chambers

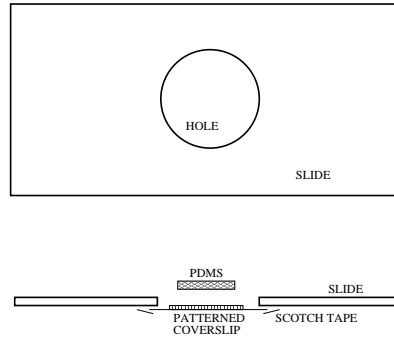


Figure 4.3.: Sketch of slide assembly.

large contrast decrease from top to bottom of the chambers. This is inherent to the imaging method, as it was verified by imaging a solution containing simply a fluorophore (figure 4.4). Image reconstruction using isosurfaces was carried out after

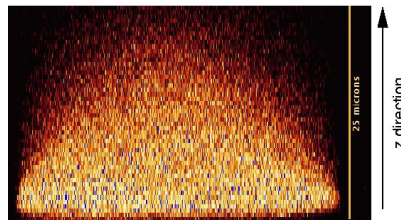


Figure 4.4.: Contrast anisotropy in the z direction. The image represents a yz section of a chamber containing a solution of water and fluorescein 0.05 mg/ml. The bottom (low z) part of the sample is the imaging side.

applying a linear gradient contrast mask in the z direction with the program ImageJ [63]. Isosurfaces were visualized using the VTK (Visualization ToolKit [64]) routines, through the freely available front-end program MayaVi. Manual particle tracking was carried out using ImageJ, and the coordinate files were analyzed with the freeware program Xmakemol [65].

Due to the flexibility of PDMS, sometimes the caps of the chambers were slightly bend inwards. This problem was enhanced by thermal expansion if I incubated the samples at 35°C to increase microtubule polymerization. In all the cases used for the analysis, deformation was checked with the confocal microscope and was less than 5% of the box height.

4.3. Results

To recapitulate, the model system I use for an elongating bundle of microtubules in a plant cell is a microtubule polymerizing from a nucleation seed in a microfabri-

cated chamber, in turn described in mathematical terms as an unstretchable filament with bending elasticity confined on a two-dimensional (cylindrical) surface. The elongation of a filament caused by polymerization represents in the experiment the elongation of bundles *in vivo* according to the dynamic spring hypothesis. The nucleation seeds play the role of microtubule nucleation agents. Clearly, in setting up this physical model one is forced to make a number of assumptions. Mainly that (i) the passive behavior of a bundle of microtubules *in vivo* is qualitatively the same as that of a single microtubule, (ii) the elongation mechanism does not matter, so that polymerization can represent relative sliding, and, for the theory, (iii) that bending elasticity is the only important feature. Although the *in vitro* experiment is the core of this chapter, I will start presenting the theoretical model, and then proceed with the experimental model system.

4.3.1. Theory

In our minimal model of microtubule cortical arrangement, the cell is depicted as a two dimensional closed surface to which the filaments are confined, typically a cylinder with caps. Microtubules (or bundles) are represented by elastic inextensible line-like objects. The bending elasticity of the filaments is the only feature responsible for their shape. In particular, there is no intrinsic chirality (a filament, at rest, does not have any structural signature that make it prefer a helical shape), and no torsional elasticity (response to twist). This is justified by experimental observations of the mechanical properties of microtubules polymerized *in vitro*. Thus, the organization at the cortex is determined only by the interplay between the length of the elastic filament and the constraint forces that confine it in a two dimensional surface. Biologically, the two dimensional confinement can be thought of as imposed by the presence of crosslinkers that connect microtubule bundles to the plasma membrane, or by the buckling of the microtubules, as in the *in vitro* model system. The model is complete once the geometry and dimensions of the box and the filaments' stiffness are specified. Comparing with the *in vitro* model system, none of these quantities can be regarded as free parameters, as the bending stiffness of a microtubule is known experimentally [66]. For the *in vivo* system the stiffness of a microtubule bundle of n filaments can be estimated as n times that of a single microtubule.

According to the dynamic spring hypothesis, the configuration a filament assumes in the cylindrical box is a helix (Fig. 4.5), whose pitch is determined by the length of the filament. Such a dynamic spring can determine its pitch by adjusting its length, as predicted by Lloyd and collaborators. Short filaments will want to be straight, and therefore align with the long axis of the cell. The longer the filament, the lower the helix pitch, so that microtubules look more and more transverse. We can call this configuration a “transverse coil”, because the grooves will be transverse to the long axis of the cell in the limit of long filament length. However, another configuration is possible, which I will call “longitudinal coil”, in which the polymer is wrapped around the long axis of the cell.

To establish which way of coiling is energetically favorable, one can assume

4. Coiling of Microtubules Confined in Box-like chambers

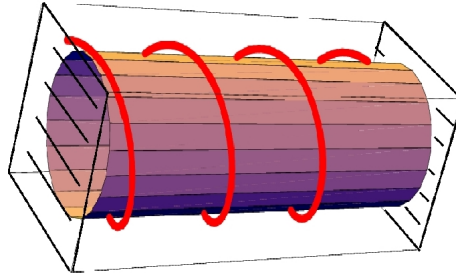


Figure 4.5.: Illustration of the dynamic spring hypothesis. The bundle wraps around the cylinder and has a helical shape. The longer the filament, the lower the helix pitch (microtubules look more and more transverse). I choose to call this configuration “transverse”.

the two classes of configurations and compare the bending energies, for a box of a given size. This comparison is of course dependent on the details of the geometry: whether the cell is cylindrical or has the shape of a parallelepiped will matter. However, we are interested in the detail-independent qualitative features. Biologically, this is motivated by the fact that elongated cells with different shape details show the same organization of interphase microtubules. In practice, I approached the problem by doing the calculations for a few different box shape details, and verifying that the results are consistent (see section 4.2.1).

As a first step we can consider only the lateral sides as accessible area. This is equivalent to imposing two walls at the extremities of the cylindrical surface that prevent the filament from spanning the cylinder caps. I model a longitudinal coil in the same way, by considering an elliptical cylinder with confining walls, or any generalized cylinder whose base has an aspect ratio (length to width) greater than one and contains the long axis of the cell. The main point is that there is a trade-off in energy cost for the filament between doing a smaller number of high-curvature turns (longitudinal coil), or a higher number of low-curvature ones (transverse coil).

According to these estimates, for aspect ratios and sizes comparable to the experimental (and biological) ones, transverse helices always have higher energy than longitudinal ones for sufficiently large filament lengths, so that, in the limit of large length, a dynamic spring that minimizes bending elastic energy would always be a longitudinal coil. For small filament lengths, transverse helices can have lower energy than longitudinal ones. The crossover length depends only slightly on the shape in the geometries I checked, but, more importantly, it depends on the aspect ratio, decreasing as the box becomes more elongated. This is described in figure (4.6), which contains a plot of the relative ratio of bending energy of a longitudinal and transverse coil for a box with longitudinal size of $35 \mu\text{m}$ as a function of lateral

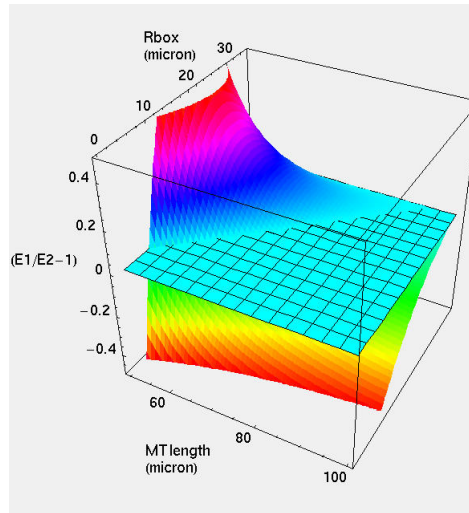


Figure 4.6.: Relative ratio of the bending energy of a longitudinal (E1) and a transverse coil (E2), as a function of filament length and lateral size for a box with longitudinal size (2D, comparing with figure 4.2) of $35 \mu\text{m}$. When this quantity is higher than zero, a transverse coil is favored. The intersection with the zero plane yields a line which gives the length below which transverse coiling is favorable as a function of the lateral size (2R in figure 4.2). For the experimental value of a lateral size of $25 \mu\text{m}$, this critical value for the filament length L is $80 \mu\text{m}$. This estimate refers to a cylindrical box for the transverse coil compared with a rectangular one with rounded caps for the longitudinal coil (figure 4.2).

size and filament length in μm . This quantity is positive when the transverse coil is favored, negative when the longitudinal coil has lower energy, and zero when the two configurations are equivalent. The graph shows that a transverse coil is favored for shorter filaments, while for longer ones the dominant shape is a longitudinal one. For the values of the parameters used in the *in vitro* experiment, we can expect a threshold filament length (above which longitudinal coiling is energetically favored) around $80 \mu\text{m}$.

Although these qualitative estimates can be useful to get a grasp on the system, one has to determine whether the actual minimum energy configuration is a helix. Let us consider again a cylinder where the filament is confined between two walls. Following the dynamic spring hypothesis, we may expect a helix as a minimum energy configuration. In fact, the solution given by minimization of the energy functional is not this one, but an oscillating configuration where the filament criss-crosses back and forth from one wall to the other (Fig 4.7b, cf. section 4.2 and the thesis of Catalin Tanase [62]). The resulting pattern of interwoven oblique lines is resemblant of what can sometimes be observed in plants, particularly in non-

4. Coiling of Microtubules Confined in Box-like chambers

elongating cells (Fig. 4.7c). Comparing this configuration with a helix of equivalent length, it is easy to understand why coiling back should be favored, as the hoops of a long helix become close to transverse circles, whose curvature is the highest on the surface of a cylinder, while the oblique grooves maintain their curvature minimal, regardless of the filament length.

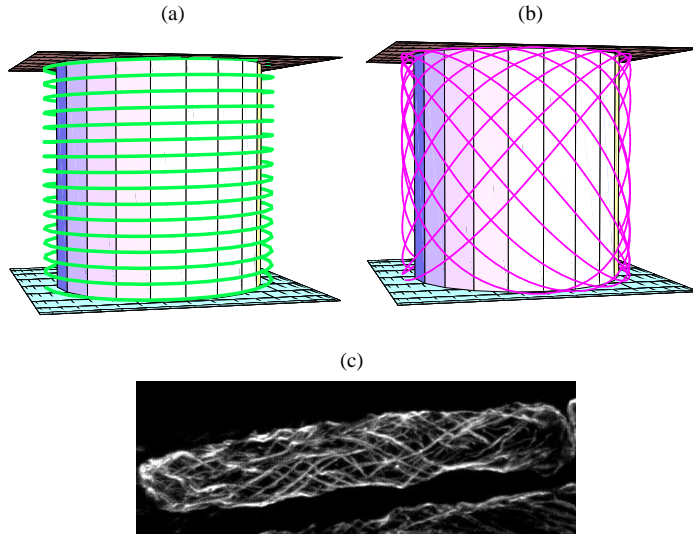


Figure 4.7.: (a) Helical configuration for an elastic filament confined in a cylinder, between two walls. (b) Solution of the Euler-Lagrange minimum energy equation for a filament of the same length. Comparing (a) and (b), it is apparent how the helix becomes more unfavorable as the filament length increases, because each groove becomes more similar to the maximum curvature trajectory, which is a transverse circle around the cylinder perimeter. (c) Non-elongating parenchima flax stem cell. Courtesy of André van Lammeren, Henk Kieft, Beata Petrovska (Plant cell Biology, Wageningen University).

Adding the caps, the filament is free to explore more configurations, including longitudinal and transverse coils as particular cases. The question is then whether a longitudinal or a transverse coil is favored when the length becomes greater than the long axis of the cell. The procedure to find minimum energy solutions can easily be extended to a cylinder with spherical caps [62]. The solutions in this case always wrap longitudinally (Fig 4.8). In other words, it is not easy for a dynamic spring based on bending elasticity neither to be transverse, nor to regulate its pitch by adjusting its length. To obtain a helical configuration from the minimum energy equation for a cylinder with walls, one has to apply an external constant force in the longitudinal direction (see ref. [62]).

Summing up, from the simple picture provided by these theoretical considera-

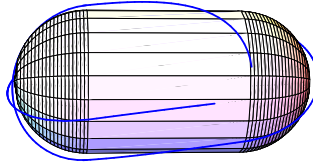


Figure 4.8.: Solution of the Euler-Lagrange equation for a spherocylinder. The filament starts from an imposed transverse orientation, but quickly reverts to longitudinal coiling.

tions we expect that

- 1) Assuming that the configurations are helices, longitudinal coils are energetically favored for longer filaments.
- 2) Transverse coils may be favored for shorter filaments.
- 3) The minimization of the energy functional shows solutions that are *not* helical, nor completely transverse configurations even in the limiting case of a cylinder without caps.
- 4) A helix can be obtained by applying a further external force on the filament [62].

4.3.2. In Vitro Experiment

In the experiment microtubules are polymerized from nucleation seeds in micro-fabricated chambers with the typical size and aspect ratios of plant cells. In these samples, the confinement is not strictly two dimensional. However, the confinement on the wall is granted by buckling, provided the filaments are long enough.

The chambers are built in microscope coverslips using lithographic techniques. They have the shape of cylinders with elliptical or rectangular base. I used chambers of two sizes, namely $35 \times 25 \times 25 \mu\text{m}$ and $80 \times 40 \times 40 \mu\text{m}$ (figure 4.9). Conventionally, I will call “top” of chamber the coverslip side, i.e. the observation face under a microscope. The chambers were filled with microtubule nucleation seeds, free tubulin and GTP and then sealed with rubber like material (PDMS). Microtubules polymerize at room temperature from the nucleation seeds in the sealed chambers, reaching lengths greater than the long axis of the box. Each chamber contains roughly a few tens of microtubules. The length of the individual polymers is not under control, as, because of the dynamic instability process, microtubules polymerizing from seeds have a wide steady-state length distribution [67].

The free tubulin is labeled with the fluorescent dye rhodamine, so that the growing microtubules can be imaged with conventional fluorescence and confocal techniques. This involves a few technical delicacies, because of both the limited free

4. Coiling of Microtubules Confined in Box-like chambers

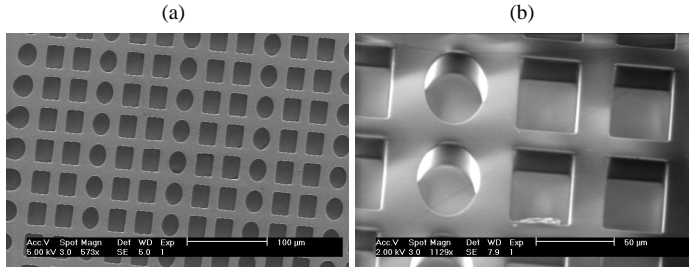


Figure 4.9.: SEM images of the chambers, which consist of rectangular boxes or cylinders with elliptical shape. A sample consists of an array of thousands of chambers on a microscope coverslip. a) Array of $35 \times 25 \times 25 \mu\text{m}$ boxes. b) Tilted view of an array of boxes sized $40 \times 40 \times 80 \mu\text{m}$ (detail).

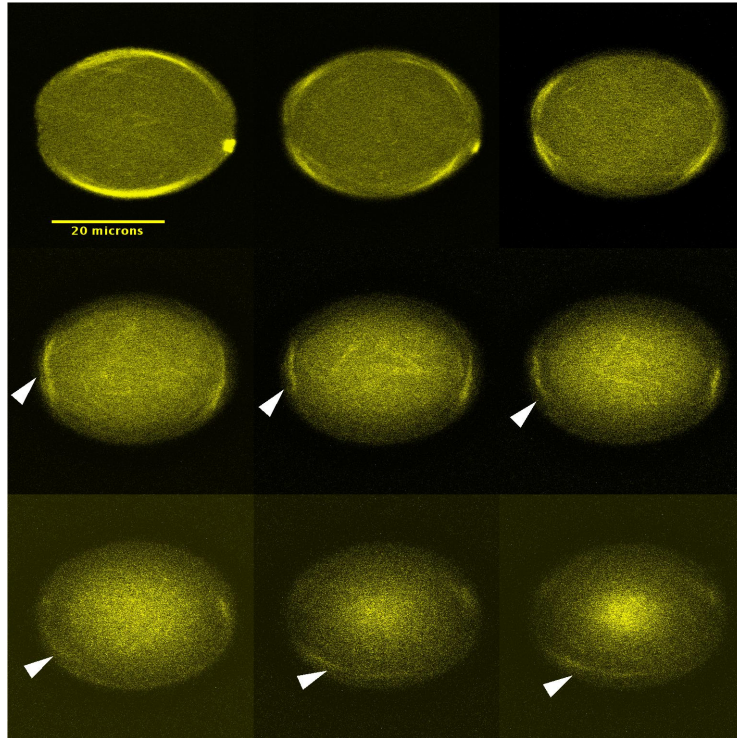


Figure 4.10.: A montage of confocal xy sections showing microtubules (white) in a chamber, from top to bottom in lexicographic order. Microtubules can be followed through the sections to form a coil. The distance between two subsequent sections is about $2.5 \mu\text{m}$

tubulin pool in the confined chambers, which prevents microtubule reassembly after photobleaching, and the scattering from the side walls, that affects the imaging (see discussion in section 4.2.2). In the bigger ($40 \times 40 \times 80 \mu\text{m}$) chambers, the microtubules were too short to form coils, and the longest ones were observed buckling after having positioned themselves along the longest available diagonal in the boxes, but not collapsing on the side walls. Thereby I estimate a maximal microtubule length of about $100\text{--}120 \mu\text{m}$. In the smaller chambers ($35 \times 25 \times 25 \mu\text{m}$) the polymers were long enough to collapse on the side walls and coil.

Confocal imaging of the chambers allows to reconstruct the full shape of the buckled microtubules in an individual box. However, it was not possible for us to image single filaments (visible in conventional fluorescence), due to thermal vibrations and scattering from the chambers' walls. After one hour of incubation, when most of the free tubulin in the chamber is polymerized from the nucleation seeds, the configurations were more stationary, and confocal microscopy could be used. The dominant configurations appear as half-pitched helices that coil around the long axis of the cell, therefore showing a longitudinal coil arrangement (figures 4.10 and 4.11).

Conventional fluorescence is useful to image the configurations of microtubules in many chambers of the array, to have a quantitative feeling of the statistical occurrence of the different coiling configurations. With this technique, only the microtubules close to the top of the chambers can be seen clearly. Nevertheless, transverse coils can be distinguished from longitudinal ones (figure 4.12). As the integration time is smaller than with the confocal, individual microtubules can be seen right after they get stuck in the long axis of the boxes.

In the later stages (after 30 min - 1 h incubation at room temperature) more microtubules polymerize, and imaging is easier. In this case it is possible to collect data in a significant number of chambers (typically a few hundreds per sample). After counting the configurations for 148 chambers over three experiments, I found 71% of the chambers showing only longitudinal coils. About 16% show mostly longitudinal coils and some transverse, while less than 1% contains only filaments coiled transversely. The rest show random, or non-definable orientations. Most of the longitudinal coils observed, wind around the direction of observation (top to bottom) of the chambers, as in Fig. 4.10. In other words, rotating the boxes 90 degrees about their long axis, I find fewer longitudinal coils, which are nevertheless present, as it can be seen from the middle right panel of Fig. 4.12.

In the early stages of polymerization, after 10 minutes of incubation at room temperature, individual microtubules are already long enough to coil, and their configurations can be observed. However, the statistics is poor because only in a few of the many chambers the polymers are long enough to be observable. Furthermore, the classification of coiling configurations in longitudinal and transverse is somehow more subjective due to imaging problems. Nevertheless, it appears that there is more balance between the number of longitudinal and transverse coils. Of 54 buckled individual microtubules observed, 36 were judged longitudinal and 18 transverse. This greater frequency of transverse coils is consistent with the theoretical prediction that such coils are favored for shorter filaments.

4. Coiling of Microtubules Confined in Box-like chambers

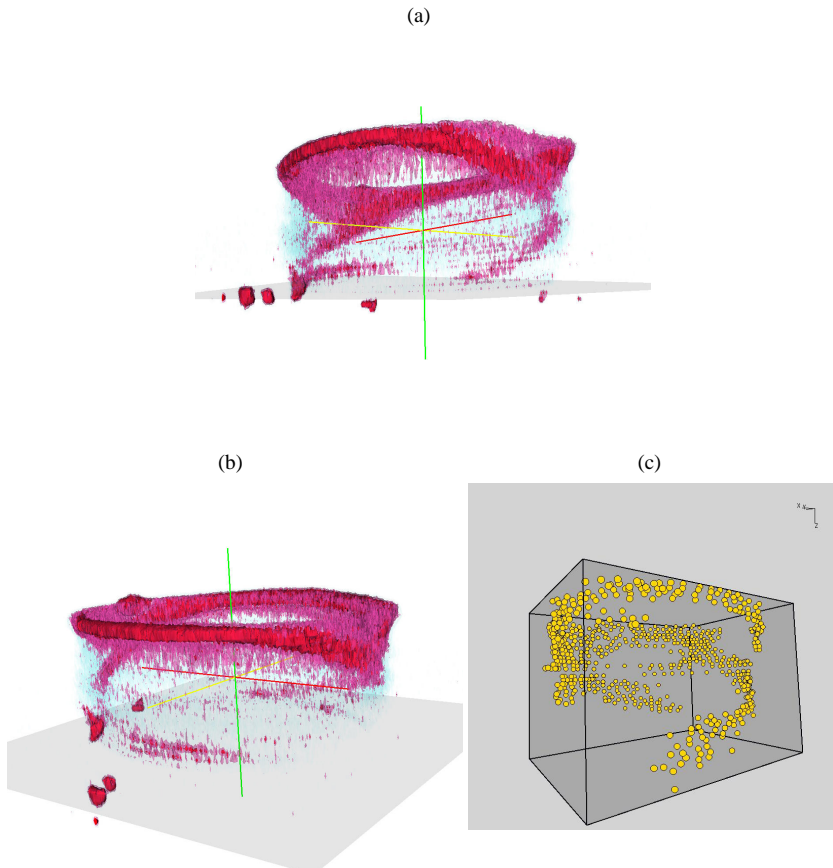


Figure 4.11.: (a) and (b) 3D image reconstructions of a configuration from a confocal z-stack using intensity iso-surfaces. The red/purple iso-surfaces show the bundle of microtubules. The light blue iso-surface shows the shape of the chamber. (c) 3D image reconstruction of a coil using position tracking methods. The spheres indicate points which were manually tracked from confocal xy stacks. The image was then reconstructed using the freeware program Xmakemol.

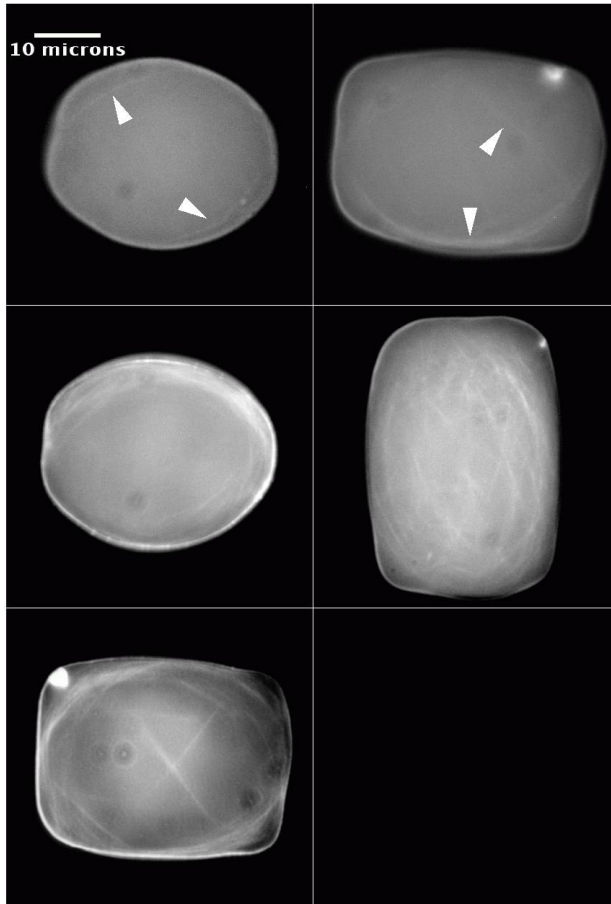


Figure 4.12.: Images from conventional fluorescence. Rhodamine labeled microtubules are imaged in the focal plane at the top of the microchambers. **TOP.** Early stages of polymerization and buckling (after 10 minute incubation at room temperature). Left: individual microtubules coiling longitudinally are visible. Right: a group of filaments is coiling longitudinally; an individual filament coiling transversely is visible. **MIDDLE** and **BOTTOM.** Images of coiled microtubules after one hour of incubation at room temperature. In most of the cases (71%) all the coiling filaments are longitudinal (middle-left). Although the dominant coil is always longitudinal, transverse coils are sometimes (16%) visible (bottom left). Middle-right panel: a chamber with marked longitudinal coiling which is not strictly top to bottom.

4.4. Discussion and Conclusion

A first fact that emerges from this investigation is that confinement and bending elasticity together are sufficient to organize the microtubules in coiling configurations that are similar to those observed in plant cells. This fact may be considered trivial, but it is a necessary preliminary to give physical grounds to the dynamic spring hypothesis, which is not a physical model in its original formulation.

The experiment and the theoretical considerations consistently indicate that, for aspect ratios and sizes that are relevant to the plant cell, the favored configuration of a dynamic spring in an elongated box is a longitudinal coil, differently from the transverse microtubule coils observed in elongating plant cells. The dynamic spring is modeled theoretically as a filament with bending elasticity and without compliance for stretch or compression, and experimentally as a microtubule growing in a confined geometry. A simple estimate predicts that, supposing that the configurations are helices whose pitch is dependent on filament length, longitudinal coiling is always energetically favored provided the filament is long enough. The experimental observations seem to be consistent with these simple theoretical predictions, as I find more balance between longitudinal and transverse coiling in the early stages of polymerization, together with a decided preference for longitudinal coils in later stages, when microtubules are longer, with a maximum length of the order of $100 \mu\text{m}$. For the experimental box size of $35 \times 25 \times 25 \mu\text{m}$, the theoretical threshold filament length above which longitudinal coiling is energetically favored is around $80 \mu\text{m}$.

It should be noted that most of the longitudinal coils observed wrapped around the top to bottom direction. This preference could be due to the fact that the surface of the chambers is not exactly symmetric for rotations around its long axis, and that geometric details play a slight role, such as a slight concaveness of the PDMS cap, or the difference in material of the box faces. Other problems could come from the anisotropic imaging with the confocal due to scattering from the side walls (see discussion in section 4.2.2). These problems could potentially bias the observations, affecting also the number of observed transverse coils. On the other hand, I consider consistency with theory, together with the fact that the theoretical predictions are robust with respect to changes in the geometry, an indication of the significance, at least from the qualitative point of view, of the experimental results.

To conclude, this work suggests that transverse and longitudinal coiling configurations of microtubules, similar to those observable in interphase plant cells can be created *in vitro* using a purified system of microtubules polymerizing in an elongated box. In doing this, the only two relevant features are bending elasticity and confinement. However, considering the aspect ratio of typical plant cells, these elements are not sufficient to account for the transverse arrangement of microtubules in the cortex of interphase plant cells. Additional factors, such as kinetic constraints or active forces generated by the cell, are necessary. The simplest possible mechanism would be that the caps of the box are not accessible, for some reason, to the microtubules forming the interphase cortical array, and the polymers are pinned at both ends, to prevent them from coiling back, so that they are forced to organize in

a transverse (helical) coil. If on the other hand the caps are accessible, by kinetic constraints I mean the following. Transverse coils are formed in the beginning of interphase, compatibly with the finding that for shorter filaments transverse coils are favored, but when the microtubules grow something prevents them from transforming their configuration into the minimum bending energy one (a longitudinal coil) and they get trapped into a metastable state. The molecular mechanism for this metastability could have a variety of microscopic origins, ranging from steric hindrance to the presence of crosslinking molecules connecting the bundles to the plasma membrane (such as the kinesin MAP120 [24, 68], or PLD [24, 69]).

As for the active forces beyond simple microtubule polymerization, such as treadmilling [33] or molecular motors, the last option is particularly appealing, because simple assemblies of molecular motor complexes and microtubules have been shown to be capable of exhibiting a remarkable number of organizations [36, 70]. For example, besides possibly being responsible for the elongation of the dynamic spring, motors could also generate forces regulating the shape of these bundles, like torsional forces that are not inherent of the single microtubules. However, to my knowledge nothing has been reported yet about the activity of motors localized in the microtubule cortical array during interphase [23]. On the other hand, it is known that such motors are involved in cell shape generation [71, 72] and cellulose deposition [73]. Based on these observations, I can advance the hypothesis that whatever the missing additional factors to have a transverse arrangement of long cortical microtubule bundles could be, they may be present only in elongating cells, consistently with the higher frequency of transverse cortical arrays in such cells.

Finally, an important question is how the basic physical behavior discussed here relates, or may relate, to biological regulation. A general point that can be made is that, for the case of cytoskeletal organization, any regulation process has to deal at one stage or the other with physical mechanisms of force generation, aggregation, organization. In this view, for example, my observations are in general consistent with the observed reversible disorganization caused by microtubule (bundles) temperature-dependent disruption in cells with mutations in the MOR-1 gene [31] (see section 2.2). However, the gap must be bridged with additional hypotheses, the simplest one being that the breakdown of long microtubule bundles in short fragments prevents the organization mechanism described here. In a similar way, hypotheses can be made regarding the physical changes underlying post-translational modifications of tubulin, such as cleavage of c-terminal tyrosine, causing re-arrangements in the cortical array [30].

4. *Coiling of Microtubules Confined in Box-like chambers*

5. Mean Field Approach to Pre-prophase Band Formation.

5.1. Introduction

In the previous two chapters, I have addressed two possible mechanisms for the formation of the cortical microtubule array. Both mechanisms, excluded volume and bundle coiling, were essentially passive in nature, and based on equilibrium properties of the system (although the second contained bundle elongation as an active ingredient, its crucial properties were determined by the passive bending elasticity). This chapter will be dedicated to the formation of the pre-prophase band under the working hypothesis (corresponding to stylized fact (7) in chapter 2) that it is caused by a drive which can be associated to the activity of molecular motors. The line of action will be mainly theoretical, and only in the last section (5.5) I will discuss the role of experimental tests *in vivo* and *in vitro*.

The fact that motor complexes (constructs where two or more molecular motors are joined through their tail region, thus being able to generate sliding motion between different microtubules) are able to interact with microtubules in the bulk or in confined geometries to create a number of patterns, such as bundles, asters and vortices, has been first established from *in vitro* experiments [36, 70]. These results were confirmed by molecular dynamics simulations [74, 75], and, to a certain extent, by theoretical mean field descriptions where a particular “move”, or mechanism of motor-microtubule action is postulated, and used to derive evolution equations in the macroscopic limit [76, 77]. For this reason. I will refer to these models as “microscopic”. However, it must be said that in all these models, the microscopic move is not based entirely on mechanical modeling, but relies on symmetry arguments. Similar one-dimensional theoretical models were developed to mimic the mechanics of stress fibers, actin bundles, or the actin cleavage furrow have been able to predict the ability of bundles and rings to contract, the response of bundles to external forces, and the insurgence of solitary waves [78, 79]. The simplicity of the one dimensional geometry allowed explicit treatment of the non-local effects of motor action. On the other hand, to date there are no results on the formation of ring-like structures, and on the interdependence of these structures with the cell finite geometry. This is the problem under investigation in this chapter.

Here, rather than making an initial choice of a microscopic “move” for the motors, I will follow a completely macroscopic approach, which builds up from a work of Kruse and collaborators [80] and is related in spirit to a similar approach by Lee

5. *Mean Field Approach to Pre-prophase Band Formation.*

and Kardar [81, 82]. This approach allows to explore the phase diagram of systems of filaments and active components in general, without prior commitment to a particular microscopic picture. The starting point will be a generic macroscopic model to describe the mean-field behavior of systems of actively driven filaments. Since the symmetries of the system are the basis to introduce the physical description, we can say this approach has the same spirit as a Landau mean field theory [83]. However, the equations of motion are more general than what can be derived from a free energy, and allow for a broad range of far from equilibrium drives. For the case of microtubules, these may include treadmilling, dynamic instability and molecular motors. The presentation of the method and the equations will be the subject of section 5.2.

As it will become clear during the exposition, the most general formulation of the model is too complex to be handled. It contains a jungle of parameters to explore, most of which are not easily interpretable. For this reason, we will make a number of restricting hypotheses, of three different types. A first kind is purely geometric, and involves reproducing features such as the correct dimensionality, topology and shape of a plant cell cortical region. A second kind of hypotheses concerns the adaptation of the model to more or less established experimental observations, namely the facts that the pre-prophase band is rotationally symmetric and, more importantly, that the microtubules that constitute it are aligned with randomly directed plus ends. Finally, the third kind of restriction will be an attempt, based on symmetry reasoning, to select for the possible driving terms caused by the activity of molecular motors with respect to treadmilling and polymerization. These hypotheses will be sufficient to characterize a smaller parameter space, many traits of which are interpretable with knowledge drawn from the theory of equilibrium suspension of rods [84].

In other words, I will adopt a top-down method, where the first objective is to find a minimal realization of the mean field theory that reproduces ring-like inhomogeneous steady states, within the physical and geometric restrictions. The second goal is to identify the role of the different parameters. This will be the core of sections 5.3 and 5.4. The advantage of this methodology is that, in absence of detailed experimental information, one is not committed to any particular microscopic picture of the activity of motor complexes, and the model remains open to the results of new investigations. The subsequent step in the method is a microscopic identification of the active terms that are recognized as important within the top-down, macroscopic approach. This is a separate task, which can be accomplished using more detailed models of motor activity [78, 75, 74, 77, 76, 62], and looking at the equations of motion they generate in a mean-field limit. Once this is known, direct experimental tests for the activity of the drive can be proposed. I will dedicate some discussion to an attempt of this kind in section 5.5, based on the hypothesis that motor complexes act as illustrated in figure 5.1. (more details can be found in the thesis of Catalin Tanase [62]).

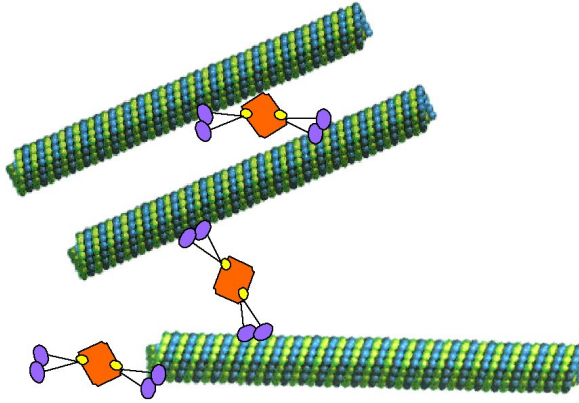


Figure 5.1.: One possible mechanism of action for molecular motors in a self-organization experiment. Motors are associated in complexes and can act on more than one microtubule, thereby generating forces between them. In a self-organization assay [36], the motors are normally kinases with an engineered biotin tail, connected by streptavidin links.

5.2. Derivation of the Equations

5.2.1. General Approach

Before I outline the derivation of the equations for the particular case of interest (that is, applying the restricting hypotheses listed above), it is worth spending a few words on the general aspects of the method [80]. The goal is to define a mean field theory for active systems of filaments, possibly in interaction with other molecules, using a Landau-like macroscopic formulation, where the equations of motion are written purely from symmetry considerations. The theory is based on a set of fields, functions of space and time (in general tensors), which are supposed to be coarse grained. That is, the small scale features of the system under exam have been averaged out, and there is a cutoff length scale a , under which nothing can be resolved.

The first step is a choice of the relevant fields, or the quantities that one is interested to include in the description. The first one, obviously, will be the filament density, followed by order parameters like filament vector orientation and nematic order (the list of tensor order parameters becomes infinite if one wants to take into account all the possible ones). It is possible to have more than one filament species, for example actin and microtubules. The density of free monomers (tubulin, actin) should be considered in case one wants to take into account the process of polymerization of the filaments. Other fields that may be considered relevant are the densities of all the other molecules that interact in some way with the filaments,

5. Mean Field Approach to Pre-prophase Band Formation.

for example, molecular motors or crosslinking agents. In summary, the fields are specified as a set of densities $\{C_i\}$ and a set of tensor order parameters $\{\mathbf{O}_i^{(R_i)}\}$ of rank R_i .

The second step is to write the equations of motion for the relevant fields. It is not possible to derive these equations from a free energy functional, because this would rule out many terms related to nonequilibrium drives. One can rely on a few less restrictive hypotheses:

- The evolution equations are first order in time. In other words, the dynamics of the fields is overdamped. For example, the evolution of a generic order parameter will be given by $\partial_t \mathbf{O}_i^{(R_i)} = \mathbf{W}_i^{(R_i)}(C_1, C_2, \dots, \mathbf{O}_1^{(1)}, \dots)$, where $\mathbf{W}_i^{(R_i)}$ is a tensor expression of the same rank and symmetry as $\mathbf{O}_i^{(R_i)}$, containing all the fields and their derivatives.
- Conservation of mass. The total densities C_i have to obey continuity equations of the kind $\partial_t C_i + \nabla \cdot \mathbf{J}_i = 0$. In the case of polymerization processes one has to take into account the appropriate source terms for filament and monomer density.
- The currents are generated by a generic stress tensor, which contains the active drives: $\eta \mathbf{J}_i = \nabla \cdot \boldsymbol{\sigma}_i^{(2)}(C_1, C_2, \dots, \mathbf{O}_1^{(1)}, \dots)$, where the expression for the stress tensor can contain all the fields and their derivatives.

In the spirit of Landau mean field theories, the expressions for $\mathbf{W}_i^{(R_i)}(C_i, \mathbf{O}_i)$ and $\boldsymbol{\sigma}_i^{(2)}(C_i, \mathbf{O}_i)$ are written as Taylor expansions in the fields, discarding all the terms that are not allowed by symmetry. These expressions can be truncated to a certain order in the fields and in the derivatives, making approximations on the strength of the nonlinearities and on the wavelengths that the system can assume respectively.

It is easy to realize that, if one wants to take everything into account at the same time, the formulation becomes bulky and cumbersome. On the other hand, one can use the formal elements of the mean field theory as building blocks to generate minimal models. This is the procedure I will follow in the remainder of this chapter.

5.2.2. Definition of the Model

Let us start by choosing the relevant fields. One first restriction one can make, related to the geometry of a plant cell cortex, is to consider a two-dimensional system. The filaments, microtubules, have an intrinsic orientation, defined, for example, by the direction of the plus end. We can associate to each of them a unit vector \mathbf{n} , which is dependent on the filament position, *i.e.* $\mathbf{n}(i) = \mathbf{n}(\mathbf{x}_i)$, where $\mathbf{x}_i = (x_i, y_i)$ is the position vector (which has two components in 2D), and i is the filament index. I assume here that the fields describing relevant quantities correspond to local averages of the “moments” of \mathbf{n} (*i.e.* the tensor products that can be constructed with it), of which we consider up to the second. The first field, which is the zeroth moment of \mathbf{n} , describes the local density $c(\mathbf{x}, t)$ of microtubules.

The first moment of \mathbf{n} is the average orientation $\mathbf{p}(\mathbf{x}, t) = \langle \mathbf{n} \rangle_{\mathbf{x}, t}$, where $\langle \cdot \rangle$ denotes an average over all filaments within a region of size a , which is large compared to a single filament and small on a “macroscopic” scale, which in the system we consider will be defined by the size of the system (a plant cell). Each region is labeled by the continuous coordinates $\mathbf{x} = (x, y)$, at time t . I choose to disregard the order parameter \mathbf{p} in this description, justified by the experimental observation that microtubules in plant cells align regardless of their orientation [85, 86, 19]. This is a radical assumption, considering that it implies that the active terms generated by motor activity do not break the microtubule left-right symmetry, while we know that a single motor is able to break this symmetry. I will discuss further the implications of this choice in section 5.5.

The nematic order parameter tensor $\mathbf{Q}^{(2)}$ describes local alignment regardless of orientation. It is symmetric and traceless. Its components $\mathbf{Q}_{\alpha\beta}^{(2)} = q_{\alpha\beta}$ are given by the local average

$$q_{\alpha\beta} = \langle n_\alpha n_\beta - \frac{1}{2} \delta_{\alpha\beta} \rangle. \quad (5.1)$$

From the tensor

$$\mathbf{Q}^{(2)} = \begin{pmatrix} q_{11} & q_{12} \\ q_{12} & -q_{11} \end{pmatrix}, \quad (5.2)$$

we can derive two parameters:

$$\begin{cases} S & = 2\lambda = 2\sqrt{q_{11}^2 + q_{12}^2} \\ \tan\phi & = \frac{\lambda - q_{11}}{q_{12}}. \end{cases} \quad (5.3)$$

S is the two-dimensional nematic order parameter that we already encountered in chapter 3. Being zero for fully disordered systems and one for fully ordered systems, it measures the degree of alignment. The angle ϕ is the orientation angle of the nematic director. Its value is zero for alignment along the x -axis, and $\pi/2$ if the alignment is along the y -axis. For both horizontal and transverse alignment, we have $q_{12} = 0$, and one can show that the sign of q_{11} indicates a specific alignment direction. Indeed, if we expand Eq. 5.3 to second order in q_{12}^2 :

$$\begin{aligned} \tan\phi &= \frac{\sqrt{q_{11}^2 + q_{12}^2} - q_{11}}{q_{12}} \\ &= \frac{|q_{11}| \left(1 + \frac{1}{2} \frac{q_{12}^2}{q_{11}^2}\right) - q_{11}}{q_{12}} \end{aligned} \quad (5.4)$$

$$= \begin{cases} \frac{q_{12}}{2q_{11}} \rightarrow 0 & \text{if } q_{11} > 0 \\ 2\frac{|q_{11}|}{q_{12}} + \frac{q_{12}}{2|q_{11}|} \rightarrow \pm\infty & \text{if } q_{11} < 0 \end{cases}. \quad (5.5)$$

Furthermore, I choose to disregard the fields associated to motor and tubulin density. The first quantity can be considered effectively constant assuming that each filament always interacts in the same way with the others. This corresponds to

5. Mean Field Approach to Pre-prophase Band Formation.

a picture in which the motors co-localize with microtubules, but their accumulation is low enough not to affect their average activity on the filaments. Disregarding tubulin density implies assuming fast diffusion. Under these assumptions, we are left with the two fields $c = c(x, t)$; $\mathbf{Q}^{(2)} = \mathbf{Q}^{(2)}(x, t)$; $(\mathbf{Q}^{(2)})_{\alpha\beta} = q_{\alpha\beta}$. We can now write the dynamic equations following the criteria listed above: conservation of total filament density, currents can be derived from a generic stress tensor, and the equations are first order in time.

$$\begin{cases} \partial_t c + \nabla \cdot \mathbf{j} = 0 \\ \partial_t \mathbf{Q}_{\alpha\beta}^{(2)} = \mathbf{W}_{\alpha\beta}^{(2)}(c, \mathbf{Q}^{(2)}), \end{cases} \quad (5.6)$$

where $j_\beta = \eta^{-1} \partial_\alpha \sigma_{\alpha\beta}$ (sums on repeated indices are implied) is the current generated by the stress tensor $\sigma^{(2)}$. We can neglect the source terms in the continuity equation for c , on the basis of the experimental observation that the density of polymerized microtubules is roughly constant during pre-prophase band formation.

The expressions for $\mathbf{W}^{(2)}$ and $\sigma^{(2)}$ are written as Taylor expansions in the fields, keeping only the terms allowed by symmetry. For example, a term like $\delta_{\alpha\beta} c$ cannot be present in the equation for $\mathbf{W}^{(2)}$, which is traceless. In the same way, no antisymmetric term can be present in the equation for $\sigma^{(2)}$. Thus, we write

$$\begin{aligned} -\eta^{-1} \sigma_{\alpha\beta} = & \delta_{\alpha\beta} (a_1 c + a_2 \Delta c) + a_3 \partial_\alpha \partial_\beta c \\ & + a_4 \delta_{\alpha\beta} c^2 + a_5 \partial_\alpha c \partial_\beta c + a_6 \delta_{\alpha\beta} c \partial_\alpha \partial_\beta c + \dots + \\ & + b_1 q_{\alpha\beta} + \delta_{\alpha\beta} b_2 \partial_\gamma \partial_\delta q_{\gamma\delta} + b_3 \delta_{\alpha\beta} q_{\gamma\delta} q_{\gamma\delta} + \dots \end{aligned} \quad (5.7)$$

$$\begin{aligned} W_{\alpha\beta} = & d_1 q_{\alpha\beta} + d_2 \Delta q_{\alpha\beta} + d_3 \Delta^2 q_{\alpha\beta} + d_4 \mathbf{Q}_{\alpha\beta}^{(2)3} \dots \\ & + f_1 \left(\partial_\alpha \partial_\beta c - \frac{1}{2} \delta_{\alpha\beta} \Delta c \right) \\ & + f_2 \left(\partial_\alpha c \partial_\beta c - \frac{1}{2} \delta_{\alpha\beta} (\nabla c)^2 \right) + f_3 \left(c \partial_\alpha \partial_\beta c - \frac{1}{2} \delta_{\alpha\beta} c \Delta c \right) + \dots \end{aligned} \quad (5.8)$$

It is possible to make a further simplification considering the spatial symmetry of the pre-prophase band. As we have seen, the geometry of a typical plant cell is a capped elongated cylinder, where microtubules are confined in the cortical region, close to the surface. The pre-prophase band is symmetric with respect to rotations of this cylinder, so it makes sense to search for solutions with this property. This is done by averaging out the fields that depend on the angular cylindrical coordinate y , or equivalently by projecting them on the x direction. This operation generates an effectively one-dimensional model where the quantities depend only on the longitudinal coordinate x (Fig. 5.2).

$$\begin{cases} \partial_t c = & \partial_x^2 \{ a_1 c + (a_2 + a_3) \partial_x^2 c + a_4 c^2 + a_5 (\partial_x c)^2 + a_6 c \partial_x^2 c + \dots \\ & b_1 q_{11} + b_2 \partial_x^2 q_{11} + 2b_3 (q_{11}^2 + q_{12}^2) \} + \dots \\ \partial_t q_{11} = & d_1 q_{11} + d_2 \partial_x^2 q_{11} + d_3 \partial_x^4 q_{11} + \dots \\ & + \frac{1}{2} f_1 \partial_x^2 c + \frac{1}{2} f_2 (\partial_x c)^2 + \frac{1}{2} f_3 c \partial_x^2 c + \dots \\ \partial_t q_{12} = & d_1 q_{12} + d_2 \partial_x^2 q_{12} + d_3 \partial_x^4 q_{12} + \dots \end{cases} \quad (5.9)$$

In what follows I will truncate these expressions trying to keep as few terms as possible. We will see that remarkable behavior emerges already by stopping this expansion at the second order in the power of the fields and in the derivatives. For consistency reasons that will become clear later, I will need to allow for fourth order derivative terms with “small” coefficients.

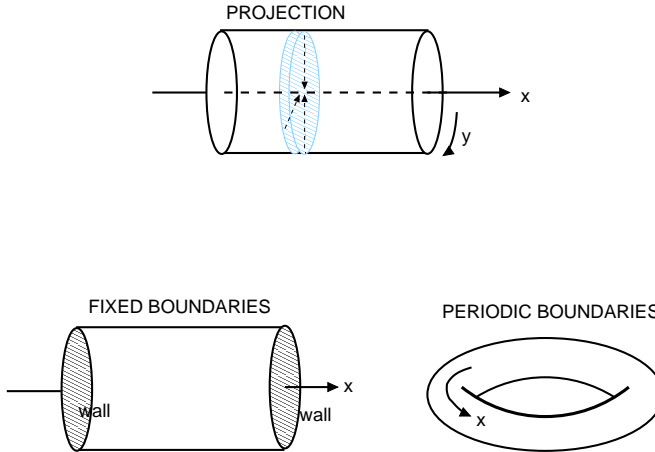


Figure 5.2.: Projection and boundary conditions.

The above equations specify the model, and have to be solved with the appropriate boundary conditions. The lateral boundaries should realistically impose zero current at the sides of the cylinder, but we will consider mainly the more easily treatable case of periodic boundaries, which topologically speaking correspond to a donut shaped cell (Fig. 5.2).

I will show that this model is minimal, in the sense that it is simple enough to be manageable, it depends on few relevant parameters, and at the same time is not trivial, showing complex behavior that includes the desired ring-like (or stripe-like, in the one-dimensional effective model) inhomogeneous steady states. I will proceed in two steps. First, I will characterize through linear stability analysis the regions of parameter space where different instabilities of a homogeneous steady state may occur. Next, I will pinpoint the region that is most worthy of examination in connection with stripe-like states, and I will analyze numerically and analytically the role of nonlinear terms in the stabilization of stripe-like instabilities.

5.3. Stability Analysis and Phase Diagram

Linear stability analysis is a standard technique in the investigation of pattern formation [42]. It consists in performing a functional expansion about a known steady state solution of the evolution equations, obtaining linearized equations with a reduced set of (rescaled) parameters, and looking for the unstable modes as a function of these parameters. In our case, the nonlinear equations are written in (5.9). It is

5. Mean Field Approach to Pre-prophase Band Formation.

easy to check that the homogeneous isotropic state $c(x) = c_0$; $q_{ij}(x) = 0$ is a solution. The functional expansion then reads

$$\begin{aligned} c(x) &= c_0 + \delta c(x); \\ q_{ij}(x) &= 0 + \delta q_{ij}(x), \end{aligned}$$

The linearized equations for $\delta c(x)$, $\delta q_{ij}(x)$ derived with this ansatz are

$$\partial_t \begin{pmatrix} \delta c \\ \delta q_{11} \\ \delta q_{12} \end{pmatrix} = \begin{pmatrix} D\partial_x^2 - \varepsilon\partial_x^4 & F_1\partial_x^2 & 0 \\ F_2\partial_x^2 & E + G\partial_x^2 - \varepsilon\partial_x^4 & 0 \\ 0 & 0 & E + G\partial_x^2 - \varepsilon\partial_x^4 \end{pmatrix} \begin{pmatrix} \delta c \\ \delta q_{11} \\ \delta q_{12} \end{pmatrix}. \quad (5.10)$$

The parameters that appear in Eq. (5.10) have been conveniently redefined for ease of interpretation. We can try to infer their meaning looking at their role in the equations and using some knowledge from equilibrium dilutions of rods [84].

- $D = a_1 + 2c_0a_4$ plays the role of a diffusion-like term. However, even if one sets $a_1 > 0$ to make it a well behaved diffusion constant in the full equations, D can change sign and become negative in the linearized equations, because of the coefficient $2c_0a_4$, coming from the quadratic term in c .
- $F_1 = b_1$ and $F_2 = \frac{1}{2}f_1$ are linear coupling terms between the second derivatives of c and q_{11} which enter in a symmetric way. Linear coupling terms of this kind between c and q_{12} are forbidden by the hypothesis of constant fields in the y direction.
- $E = d_1$ Can be identified with a rotational diffusion term for the rods, when $E < 0$. In equilibrium systems, E crossing zero is a signature of a nematic-like transition.
- $G = d_2$ can be seen as an “elastic constant” term, comparing with an evolution equation of the order parameter of an equilibrium liquid crystal [84].
- $\varepsilon > 0$ is a (small) stabilizing term that we include in order to have stability at small wavelengths. This term is necessary for consistency with the coarse-grained description we adopt here, because any instability below the cutoff length scale a would be nonphysical. We will see that no physical features of the system depend on ε .

The current caused by the perturbing fields we have applied reads

$$-j = D\partial_x\delta c + F_1\partial_x\delta q_{11} - \varepsilon\partial_x^3\delta c. \quad (5.11)$$

In case one wants to perturb around a state with nonzero (constant) order, the equations have to change in order to allow for this steady state solution. For example, to obtain a steady state solution with nonzero alignment of the kind

$$\mathbf{Q}_0^{(2)} = \begin{pmatrix} -q_s & 0 \\ 0 & q_s \end{pmatrix},$$

it is sufficient to add terms proportional to $d_1 q_s$ in the equations for q_{11} and q_{12} that appear in (5.9). In this case, if $q_s = 1/2$, there is perfect order along the y direction; for lower values, the ordering decreases gradually. However, it is easy to check that perturbing around this steady state ($q^{11} = q_s + \delta q^{11}$; $q^{12} = 0 + \delta q^{11}$), the linearized dynamic equations remain unchanged, because all the contributions of the pre-ordering cancel out.

5.3.1. Periodic Boundaries

If we impose periodic boundaries, the problem can be solved using a Fourier series ansatz, which guarantees automatically that periodicity is fulfilled. This, applied to Eq. (5.10), gives

$$\partial_t \begin{pmatrix} \delta c \\ \delta q_{11} \\ \delta q_{12} \end{pmatrix} = \begin{pmatrix} -Dk^2 - \varepsilon k^4 & -F_1 k^2 & 0 \\ -F_2 k^2 & E - Gk^2 - \varepsilon k^4 & 0 \\ 0 & 0 & E - Gk^2 - \varepsilon k^4 \end{pmatrix} \begin{pmatrix} \delta c \\ \delta q_{11} \\ \delta q_{12} \end{pmatrix}, \quad (5.12)$$

with $k = \frac{2n\pi}{L}$, $n \in \mathbb{Z}$. For every value of k , the solution in Fourier space is

$$\begin{pmatrix} \delta c(k, t) \\ \delta q_{11}(k, t) \\ \delta q_{12}(k, t) \end{pmatrix} \sim e^{\lambda t} \begin{pmatrix} \delta c(k, 0) \\ \delta q_{11}(k, 0) \\ \delta q_{12}(k, 0) \end{pmatrix}.$$

Substituting this expression in Eq. (5.12), we can read it as an eigenvalue problem, where the sign of the real and imaginary part of the eigenvalue $\lambda(k)$ determine the time evolution of the mode labeled by k . A positive $\text{Re}\lambda$ corresponds to exponential growth, a negative $\text{Re}\lambda$ to exponential damping of the mode. An instability occurs when, for a small change of parameters, the eigenvalue with highest real part crosses zero. An eigenvalue with nonzero imaginary part determines an oscillating solution for the particular mode it refers to. An instability of this kind is called a Hopf bifurcation [42].

The dynamics for q_{12} is not coupled to the other fields. Its corresponding eigenvalue is $E - Gk^2 - \varepsilon k^4$. The upper 2×2 block matrix can be analyzed independently. Its eigenvalues are

$$\lambda_{12} = \frac{1}{2} \left(E - (D + G)k^2 - 2\varepsilon k^4 \pm \sqrt{E^2 + 2E(D - G)k^2 + (4F_1 F_2 + (D - G)^2)k^4} \right). \quad (5.13)$$

For **large** k , solutions have to be stable for consistency with the coarse-graining hypothesis. This is guaranteed by the fourth order derivative terms, if $\varepsilon > 0$. In the $k = 0$ limit, one of the two eigenvalues is always equal to E (more precisely, the highest eigenvalue is always $\max(0, E)$). This means that the $k = 0$ (constant) mode is unstable iff $E > 0$. This kind of global instability is uninteresting for us, because it cannot be directly related to pattern formation. Furthermore, this kind of solution for the perturbing field δc is not compatible with conservation of mass (for the order parameter, it is similar to a nematic transition). Thus, for the further

5. Mean Field Approach to Pre-prophase Band Formation.

analysis I will always assume that $E \leq 0$, which corresponds to a passive term, interpretable as rotational diffusion.

Since the characteristic equation is a second order polynomial in λ , the eigenvalues are either both real or complex conjugates. On the other hand, the same eigenvalue equation is a fourth order polynomial in k^2 , involving all the other parameters. For this reason, although it is in principle possible to obtain everything analytically, this may be rather involved. The fastest way to derive the complete map of instabilities is to study the sign of $\lambda_1 + \lambda_2$, $\lambda_1 \lambda_2$ and of the argument of the square-root part of the eigenvalues $\Delta(k)$, as a function of k and the parameters. These quantities have particularly simple expressions:

$$\begin{cases} \lambda_1 + \lambda_2 = E - (D + G)k^2 - 2\epsilon k^4 \\ \lambda_1 \lambda_2 = k^2 f^{(3)}(k^2) \\ \Delta = ((D - G)^2 + 4F_1 F_2)k^4 + 2E(D - G)k^2 + E^2, \end{cases}$$

where $f^{(3)}$ is a third-order polynomial in k^2 .

$$f^{(3)}(u) = \epsilon^2 u^3 + \epsilon(G + D)u^2 + (DG - F_1 F_2 - \epsilon E)u - DE.$$

Before we go on with the discussion, it is necessary to spend a few words classifying the possible instabilities that we can expect given these expressions. Now, the eigenvalues approach $k = 0$ as

$$\begin{cases} \lambda_1 = -Dk^2 \\ \lambda_2 = E - Gk^2. \end{cases}$$

Let us assume they are real. As we know that they have to become negative for large k , the possibilities are: for $D > 0$ (1a) they always stay negative, and the homogeneous state is stable, or (1b) the largest becomes positive for a certain value of k and then crosses zero again (Fig. 5.3c); for $D < 0$ (2a) The largest eigenvalue, which starts with a positive slope, crosses zero three times (Fig. 5.3b) or (2b) only once (Fig. 5.3a). This last possibility is the one I will concentrate on, for two reasons. First, the lowest mode to become unstable is always the first, so that a stripe-like mode is always involved in the instability. Second, this instability can never be a Hopf bifurcation, because, supposing the eigenvalues become complex, their real part $(\lambda_1 + \lambda_2)/2$ is always negative for small, k , because we chose $E < 0$. If the eigenvalues can become complex, the situation is in principle more intricate, because, the real part $(\lambda_1 + \lambda_2)/2$ can cross zero twice if $D + G < 0$. However, we will see that the only kind of instability that can occur is the one sketched in Fig. 5.3a.

To localize the boundaries between the different kinds of instability, we can distinguish two cases.

- If $D + G > 0$, $\lambda_1 + \lambda_2$ is always negative, thus the instabilities are simply located by imposing $\lambda_1 \lambda_2 = 0$. One solutions of this is always $k = 0$, the others are given by the real and positive roots of $f^{(3)}$. It can be easily checked that, in the limit of small ϵ , $f^{(3)}$ can have 2 or none positive roots if $D > 0$,

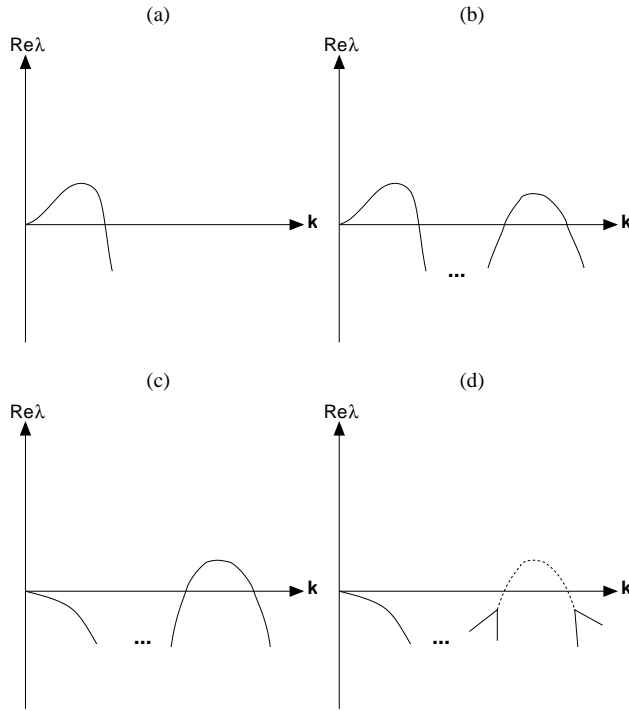


Figure 5.3.: Instabilities that can occur with periodic boundary conditions. The largest real part of the eigenvalues is plotted as a function of k . (a) 1 real root of $f^{(3)}$ corresponds to instabilities that start from $k = 0$, so that the lowest mode to become unstable is always the first. For this instability the eigenvalue can never be complex. This is the most interesting kind of instability for us, because the stripe-like mode $k = 1$ is always unstable. (b) Three real roots of $f^{(3)}$, with $\Delta > 0$ at both instabilities. The small k instabilities compete with other ones with smaller wavelengths. (c) Two real roots of $f^{(3)}$, with $\Delta > 0$ at the instability. The system becomes unstable at small wavelengths. (d) No real roots of $f^{(3)}$. The eigenvalues (solid line) become complex ($\Delta < 0$), but their real part (dashed line) crosses zero at finite k (Hopf bifurcation).

5. Mean Field Approach to Pre-prophase Band Formation.

and 1 or 3 positive roots if $D < 0$. The possible instabilities that can result are (a), (b), (c) in Fig. 5.3. Furthermore, if the eigenvalues are complex conjugates, $\lambda_1 + \lambda_2 = 2\text{Re}\lambda_{12} < 0$, so that there cannot be Hopf bifurcations (instabilities with complex eigenvalues).

- If $D + G < 0$, $\lambda_1 + \lambda_2$ can become positive, and one has to be more careful. To characterize the instabilities, it is necessary to study the sign of both $f^{(3)}$ and Δ . The roots of $f^{(3)}$ are discussed in the same way as in the previous case. In addition, when $\Delta < 0$ at the instability, there will be a Hopf bifurcation. It turns out that this is possible only for $D > 0$, $D + G < 0$, $F_1 F_2 < 0$, $G > D - \sqrt{-4F_1 F_2}$, and the corresponding instability is the one sketched in Fig. 5.3d.

From all these considerations, one can derive the stability diagram of Fig. 5.4

Looking at Fig. 5.4, it is striking how even such a simple model can exhibit extremely diverse behavior. Once again, the question is what to focus on using physical arguments. I have already argued that the relevant instability for the problem we are concerned with is the one depicted on Fig 5.3a. In addition, one can make the further physical restriction that the relevant instabilities are those that are accessible from the homogeneous state upon continuous variation of one control parameter. This corresponds to a picture where the plant cell cannot alter suddenly the parameters associated to motor activity (for example the density of motors), but it has to do it slowly, starting from an initial isotropic state after cell division. Accepting this fact, we can restrict ourselves to the transition marked by an arrow in the lower panel of Fig. 5.4. Admittedly, the realism of this hypothesis can be discussed, and in principle other regions of parameter space should be explored. On the other hand, to do this, one should be guided by the feedback from experiment and microscopic modeling. Given the present knowledge, I consider it sufficient to explore the implications of this gradual parameter variation hypothesis, and concentrate on one transition. This choice, of course, will have to be confronted with experimental results.

Let us now look at the unstable modes. The eigenvalues given in equation (5.13) correspond to the following eigenvectors (up to an overall normalization factor):

$$\vec{v}^\pm = \begin{pmatrix} v_1^\pm \\ v_2^\pm \end{pmatrix} = \begin{pmatrix} E + (D - G)k^2 - \varepsilon k^4 \pm \sqrt{(E + (D - G)k^2)^2 + 4F_1 F_2 k^4} \\ 2F_2 k^2 \end{pmatrix}.$$

We can focus on \vec{v}^+ , which always has the largest real part. From the above expression, it is easy to see that $v_1^+ \cdot v_2^+$ can be positive or negative. In fact, replacing $F_1 \rightarrow -F_1$ and $F_2 \rightarrow -F_2$ changes the sign of v_2^+ but leaves the corresponding eigenvalue unchanged. As a consequence, there are two equivalent possibilities for the unstable modes,

$$\begin{aligned} \delta c_k(x) &= v_1^+ \cos(kx) \\ \delta q_{11,k}(x) &= v_2^+ \cos(kx), \end{aligned}$$

that, for $k = 2\pi/L$ correspond to a longitudinal or a transverse nascent ring. This is illustrated in Fig. 5.5. The stripes of Fig. 5.5 are always the lowest unstable

5.3. Stability Analysis and Phase Diagram

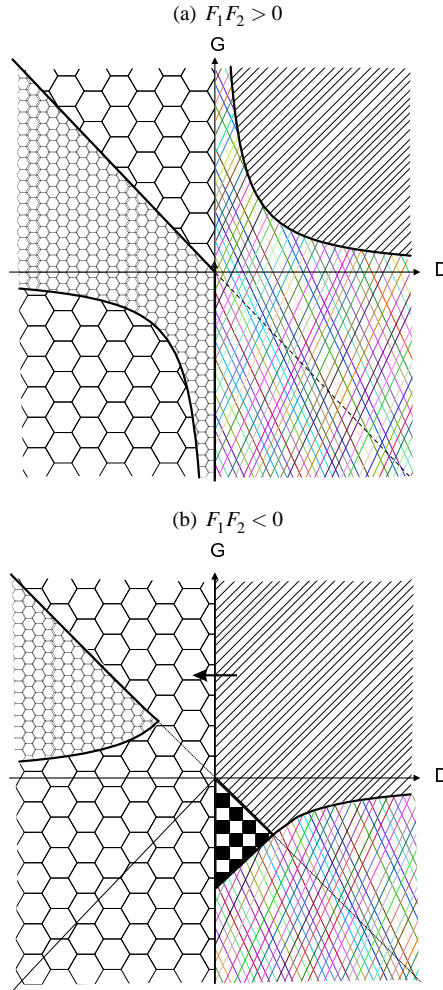


Figure 5.4.: Instability phase diagram for periodic boundaries. The different instabilities are plotted as a function of the parameters $G, D, F_1 F_2$, in the limit of small ε . In the figures hatching corresponds to stability of the homogeneous state, cross-hatching to instabilities at finite k (Fig. 5.3c), large hexagons to small k instabilities (Fig. 5.3a), small hexagons to competition between finite k and small k instabilities (Fig. 5.3b), checkerboard tiling to oscillatory instabilities (Fig. 5.3d). (a) $F_1 F_2 > 0$ (b) $F_1 F_2 < 0$.

5. Mean Field Approach to Pre-prophase Band Formation.

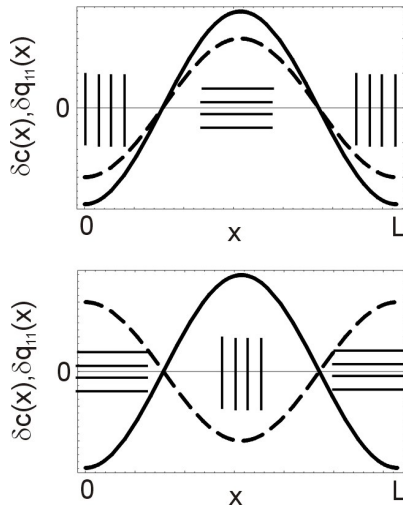


Figure 5.5.: Unstable stripe-like modes for periodic boundaries. $\delta c(x)$ (solid line) and $\delta q_{11}(x)$ (dashed line) are plotted as a function of x . Two equivalent possibilities exist, for both of which $\delta q_{12} = 0$. In the first case (higher panel), higher density correlates with longitudinal ordering, giving rise to a longitudinal stripe, while in the second case (lower panel) higher density is associated with transverse ordering, as in the pre-prophase band.

mode in the transition we are focusing on. Furthermore, there will be always be a particular size L of the system, for which the first mode is also the fastest growing one. The fact that ordering of the unstable modes can only be transverse to the x direction (the “long axis” of the plant cell) comes formally from the requirement of rotationally symmetric patterns, which uncouples q_{12} from the density c at linear order.

To summarize, from this analysis it emerges that, for first mode (stripe-like) instabilities, the change of sign of D from positive to negative, and therefore the quadratic term in the density field (a_4 in Eq. (5.9)), is fundamental. In addition, the product $F_1 F_2$ has to be negative, corresponding to negative feedback between ordering and growth, and G has to be positive. Finally, for periodic boundaries, there is a symmetry between longitudinal and transverse stripes that start emerging.

5.3.2. Zero Flux Boundary Conditions

The stability analysis with periodic boundaries I have presented in the previous section has the advantage to be analytically treatable. More realistically, thinking about the plant cell problem, one should impose the condition of no flux, or zero

current at the boundaries, instead. For example, the boundary conditions

$$\begin{cases} j(0) = j(L) = 0 \\ \delta q_{11}(0) = \delta q_{11}(L) = 0 \\ \delta q_{12}(0) = \delta q_{12}(L) = 0, \end{cases} \quad (5.14)$$

where one sets in addition fixed boundaries for δq_{ij} , satisfy this requirement. Unfortunately, so far I was not able to find the solution of this fixed boundary problem analytically. For this reason the structure of the stability diagram was explored numerically or relying on approximations.

Using these techniques to analyze the transition that emerges from the periodic boundary case, I find that

- Again, δq_{12} , is decoupled from the other perturbing fields, so it is straightforward to find the solution

$$\delta q_{12}(x, t) = \sum_{n=0}^{\infty} \delta q_{12}^0 e^{(E - G(\frac{\pi n}{L})^2 - \varepsilon(\frac{\pi n}{L})^4)t} \sin\left(\frac{\pi n x}{L}\right),$$

which has the same stability features as the previous case.

- In the limit of large k (small wavelengths), there are periodically spaced discrete modes with the same relation $\lambda(k_n)$ as for the periodic boundary case, so that, for sufficiently large k the large k instabilities are located in the same regions of parameter space as in the case of periodic boundary conditions.
- The critical surface $D = 0$ found for $F_1 F_2 < 0$ appears to be still present. In this case as well the lowest mode to become unstable is the first, although its functional form will be changed due to the different boundary conditions. It is possible that the symmetry between longitudinal and transverse nascent stripes will be broken in these circumstances.

Although the problem of linear stability analysis with zero flux boundary conditions is still open and subject to current work, these results are sufficient to indicate that the instability we are concentrating on is still present.

5.4. Solutions of the Nonlinear Mean Field Equations

Linear stability analysis helped us locating the regions of parameter space where inhomogeneous nonequilibrium states form. The critical line $D = 0$, for $F_1 F_2 < 0, G > 0$ was chosen as the most important to be analyzed, as it is the only boundary between the homogeneous state and first mode instabilities. However, in order to find the final state and characterize it, the full nonlinear equations (Eq. (5.9)) are needed. Stated another way, the question is to find the appropriate nonlinear terms that stabilize into stationary stripe-like patterns the stripe-like instabilities we have

5. Mean Field Approach to Pre-prophase Band Formation.

characterized. For this reason, I will start with all the terms written in Eq. (5.9), and I will try to reduce the equations to a minimal set of terms, able to generate the wanted solution. I will look for inhomogeneous steady states both analytically, using a slaving approximation for the fields, and with the use of numerical tools.

5.4.1. Slaving Approximation

It is possible to reduce the set of steady-state equations (Eq. (5.9)) to a nonlinear equation that is analytically solvable. In order to do this, one has to start from the hypothesis that the components $q_{ij}(x)$ of the order parameter follow adiabatically the density field $c(x)$ in the dynamics. That is, the relaxation of the orientational degrees of freedom is much faster than the characteristic time of variation of the density.

In this hypothesis, we can linearize the equations of motion for the order parameter, and keep only the nonlinear terms contained in the evolution equation for the density. Once again, the equation for q_{12} is decoupled from the others and can be ignored, so that the steady state equations for q_{11} and c become

$$\begin{cases} 0 = \partial_x^2 \{ a_1 c + (a_2 + a_3) \partial_x^2 c + a_4 c^2 + a_5 (\partial_x c)^2 + a_6 c \partial_x^2 c + \\ \quad b_1 q_{11} + b_2 \partial_x^2 q_{11} + 2b_3 (q_{11}^2 + q_{12}^2) \} \\ 0 = d_1 q_{11} + d_2 \partial_x^2 q_{11} + d_3 \partial_x^4 q_{11} + \frac{1}{2} f_1 \partial_x^2 c. \end{cases} \quad (5.15)$$

When $d_1 = E$ and $d_2 = G$ are nonzero, the linear differential equation for q_{11} can be solved implicitly with the method of the Fourier transform getting

$$q_{11} = -\frac{1}{2\pi} \int dk \int dx' \frac{f_1 k^2}{2(E - Gk^2)} c(x') e^{ik(x'-x)} := - \int dx' G(x-x') c(x'), \quad (5.16)$$

where $G(x)$ can be computed directly using the residue theorem:

$$G(x) = \pi \sqrt{\left| \frac{E}{G} \right|} e^{-x \sqrt{\left| \frac{E}{G} \right|}}.$$

This convolution term has to be inserted in the steady state equation for c , which has the form $0 = \partial_x j = \eta^{-1} \partial_x^2 \sigma_{11}$. Assuming that the current j is zero, and therefore $-\eta^{-1} \sigma_{11} = \Gamma_0$, a constant, our steady state equation for the density is equivalent to

$$\eta^{-1} \Gamma_0 + a_1 c + a_4 c^2 + a_5 (\partial_x c)^2 - b_1 \int dx' G(x-x') c(x') = 0, \quad (5.17)$$

where I have neglected b_3 , which, taken into account, would add to this equation the solution of the equation for q_{12} as an inhomogeneous term. This integro-differential equation has a compact, straightforward form, but is still too complex to be solved analytically.

Making the further assumption that $E = d_1 = 0$, i.e. the ‘‘rotational diffusion’’ is switched off, it is immediate to check that Eq. (5.17) reduces to

$$\Gamma_0 = \left(a_1 - \frac{(b_1 + 2b_3)f_1}{2G} \right) c - a_4 (c^2 + \frac{a_5}{a_4} (\partial_x c)^2) + a_6 c \partial_x^2 c.$$

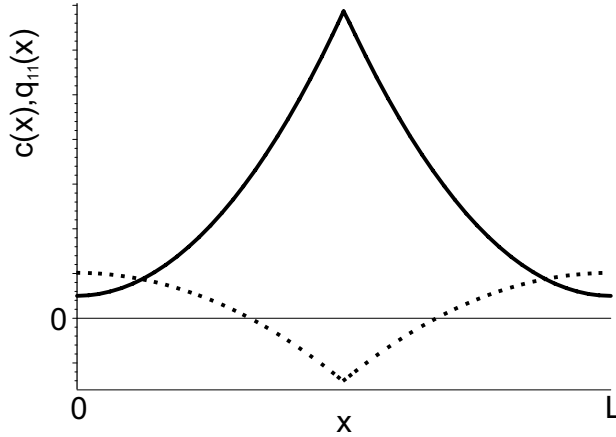


Figure 5.6.: Example of stripe-like inhomogeneous steady-state solution obtained analytically for periodic boundary conditions. The density $c(x)$ (solid line) and the first component of the order parameter q_{11} (dotted line) are plotted as a function of x . Both exhibit a singularity in the middle. The plotted solution corresponds to a transverse stripe (cf. Fig. 5.5).

This equation has stripe-like solutions if $\lambda^2 := -\frac{a_5}{a_4} > 0$ and $a_6 \geq 0$. These solutions can be found provided $a_2 + a_3$ is set to zero. We can distinguish two cases:

- 1) $a_6 = 0$. The equation can be solved analytically. The inhomogeneous steady state solution is of the kind

$$\begin{cases} c(x) = & \alpha + \beta \cosh\left(\frac{x}{\lambda}\right) \\ q_{11}(x) = & \alpha' - \beta \cosh\left(\frac{x}{\lambda}\right), \end{cases}$$

where the coefficients can be computed imposing the periodic boundary conditions and the normalization condition for c . This solution (formally identical to the one found in [79]) is always a transverse stripe with a singularity at the peak (see Fig. 5.6), such that $(\partial_x c)^2$ is continuous in this point.

- 2) $a_6 > 0$. The equation of motion can be solved numerically finding nonequilibrium inhomogeneous steady states similar to the one shown in Fig. 5.6, but with a smoothed peak (because in this case also $c\partial_x^2 c$ has to be continuous).

These considerations indicate that the most important nonlinear terms to obtain our stripe-like solutions are c^2 , which drives the instability, and $(\partial_x c)^2$, which stabilizes the pattern. Furthermore, $c\partial_x^2 c$, removes the singularity from the peak of the stripe.

5.4.2. Numerical Solutions

The numerical solutions are obtained by discretization of the fields and the nonlinear differential operators in space and time, on a fixed mesh. For example, a field

5. Mean Field Approach to Pre-prophase Band Formation.

$\varphi(x, t)$ becomes the discrete field $\varphi_{i, \tau}$, and the solution of the equation of motion looks like

$$\varphi_{i, \tau + \Delta\tau} = \varphi_{i, \tau} + \hat{\mathcal{N}} \varphi_{i, \tau} \Delta\tau,$$

where $\hat{\mathcal{N}}$ is the discrete equivalent of the operator acting on φ (for example, $\partial_x \varphi(x, t)$ becomes $(\varphi_{i+1, \tau} - \varphi_{i-1, \tau})/2\Delta x$, $\varphi(x, t)^2$ corresponds to $\varphi_{i, \tau}^2$, etc.).

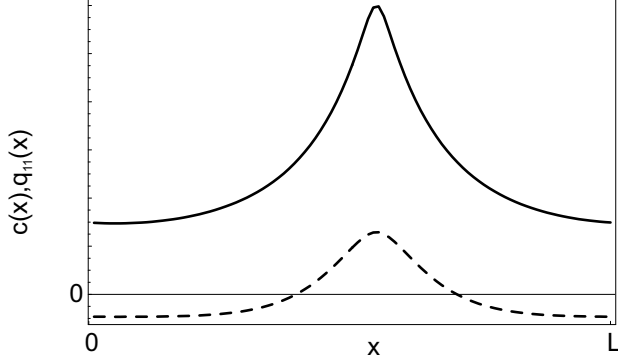


Figure 5.7.: Stripe-like pattern obtained with a numerical solution of the full nonlinear equations. The density $c(x)$ (solid line) and the first component of the order parameter q_{11} (dashed line) are plotted as a function of x . The values of the parameters of the linearized equations that correspond to this solution are $D = -1.5, G = 1.5, F_1 F_2 = -1, E = -1, \varepsilon = 0.005$, whereas the coefficients of the nonlinear terms are $a_4 = -3, a_5 = 1, a_6 = -0.1, d_4 = -1$. The plotted solution corresponds to a longitudinal stripe (cf. Fig. 5.5).

The solutions obtained with this technique do not rely on any approximation on the relaxation time scales of the fields, and, once again, show the formation of stripe-like stationary states in the region of interest. One example is shown in Fig. 5.7. The numerical solutions seem to indicate that, together with the terms that already emerged from the analytical treatment, a third-order term in the order parameter may be important to stabilize the emerging patterns. Finally, as the expression for the entire stress tensor is known from equation 5.7, one can use it to calculate the tension profile of the forming ring, or of the inhomogeneous steady state, once this solution is available. In other words, the model is built to output the contractile forces generated by a ring, once this is formed.

5.5. The State of Microscopic Modeling and Experiments

Having identified a minimal set of terms (essentially, c^2 and $(\partial_x c)^2$) necessary to drive the system far from the equilibrium (homogeneous and isotropic) state, and

to stabilize emergent stripe-like patterns, the problem that remains open is the connection of these terms with the action of molecular motors, or possibly other kinds of active drives. This is, it must be said, quite a delicate point. Throughout this chapter, justified by the fact that microtubules within the pre-prophase band do not possess vector-like orientation, I have chosen to look at states where the left-right symmetry of the filaments is not broken. However, the activity of a single motor does break this symmetry, and this has been the basic ingredient of all the microscopic models so far. As a consequence, the pattern-forming instabilities in these microscopic models break this symmetry as well. To date, all the available theoretical microscopic models [77, 76], except for the one-dimensional treatment of Kruse and collaborators [79], have the limitation of relying on some non-mechanical hypotheses, such as symmetry arguments, for the implementation of motor activity. For this reason, an entirely mechanical (i.e. based only on force balance equations) two- and three-dimensional microscopic model was developed within the same project by Catalin Tanase [62]. In this model, motors with the same directionality (plus- or minus-ended) are supposed to be associated in dimers, and to slide on microtubules generating a constant force (see Fig. 5.1). The resulting motion is dictated by the overdamped force-balance equation. This dynamics is then implemented in the Smoluchowski equation formalism, as in [77], which is then used to derive macroscopic evolution equations for the relevant fields comparable to the ones I discussed in this chapter. Once more, the results indicate that the instability-driving terms come from the vector field $\mathbf{p}(\mathbf{x}, t)$ associated to the orientation of microtubules. Given these facts, two main options remain open

- The microscopic drive of the motors is such that, on average, left-right symmetry is respected. For example, motor proteins may act in heterocomplexes containing motors with different directionalities, or the effects of plus- and minus-ended complexes may somehow balance each other.
- The real instabilities are driven by the vector-like orientation field, and orientational disorder is established at a later stage of pre-prophase band formation, with a mechanism that needs to be elucidated.

On the *in vivo* experimental aspect, besides the data on localization already mentioned [23], nothing is known on the details of the activity of molecular motors localized in the microtubule cortical arrays, except an indirect association with morphogenetic phenotypic shape modifications [72]. Most of the recent attention seems to be concentrated on other active traits of microtubules, dynamic instability and treadmilling [34, 19, 33, 85]. On the other hand, some data is available on the dynamics of pre-prophase band formation (Fig. 5.8), which could be compared to the dynamics of pattern formation in the model when more insight is gained. Finally, concerning *in vitro* experiments, the most straightforward approach is to combine the confinement in a box-like chamber of Ch. 4 with a self-organization assay experiment [36] where motor protein tetramers are formed by linking biologically engineered kinesin with a biotin tail with streptavidin (see Fig. 5.1). Experiments of this kind are currently in progress, and some preliminary results are shown in Fig. 5.9.

5. Mean Field Approach to Pre-prophase Band Formation.

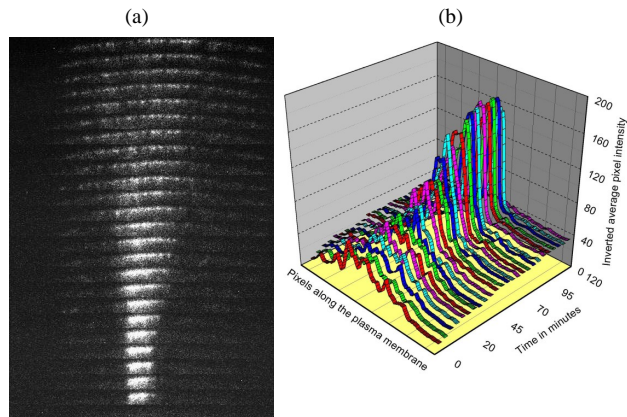


Figure 5.8.: Dynamics of pre-prophase band formation (Jan Vos, EMBL, Heidelberg). (a) Kymograph of the plant cell cortex. (b) Graph of the pixel intensity distribution as a function of time. The width of the intensity distribution shrinks linearly with time.

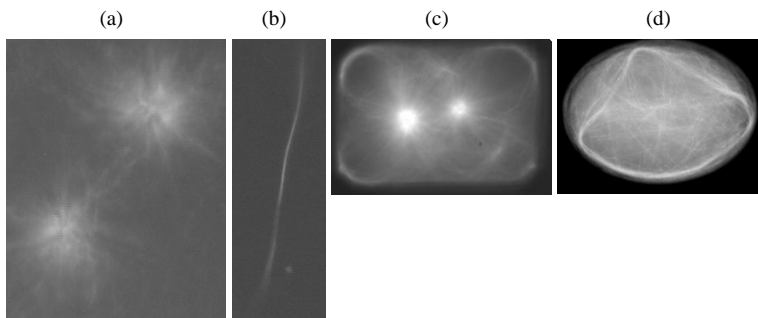


Figure 5.9.: Preliminary results of self-organization assays in bulk and box-like confining geometries. (a) Asters in bulk. The size of the picture is approximately $150 \times 200 \mu\text{m}$. (b) Bundle in bulk, approximately $60 \mu\text{m}$ long, formed by dynamic aggregation of microtubules and motors. (c) Asters in $35 \times 25 \times 25 \mu\text{m}$ sized box. (d) Ring-like pattern in $35 \times 25 \times 25 \mu\text{m}$ sized box. The experiments are performed with BioK401 biotinylated kinesin complexes (purified as in reference [87]) formed with streptavidin. In all the above pictures the concentration of motors is $50 \mu\text{g/ml}$. In (a),(b) microtubules are taxol-stabilized. In (c),(d) microtubules grow from nucleation seeds as in the experiments described in chapter 4.

5.6. Conclusions

I have presented a generic framework to provide a coarse-grained description of active systems of filaments and motors. Within this framework, I adopted a top-down approach to describe the formation of ring-like patterns in a system with the geometric features of a plant cell, with the objective of demonstrating the feasibility of the role of motor activity in the context of pre-prophase band formation, as prescribed by stylized fact (7) in Ch. 2. The first advantage of this method is that it is generic. That is, one is not committed to a particular microscopic interpretation of the active process that drives pattern formation, which is useful, given the scarcity of experimental evidence. Rather, the model allows to look for the general circumstances, allowed by symmetry considerations, under which the formation of a ring-like pattern is possible, and leaves the interpretation to a subsequent step. Furthermore, the geometric and symmetry constraints imposed by considerations on the patterns formed by cortical microtubules allowed to simplify greatly the general problem, and to reduce the space of relevant parameters to a manageable one. Thanks to this, I could map all the possible instabilities of the homogeneous state for periodic boundaries, isolate one region where the transition to a stripe-like, or ring-like, state is possible, and find analytical and numerical solutions for steady states of this kind.

Interestingly, because of the requirement of lack of vector-like orientation in the pattern, the instability isolated here is driven by a term which does not break the left-right symmetry of the filaments, and, it seems, cannot be derived by microscopic models that are based on this feature [76, 77, 62]. If this is true, two possibilities remain open: either there are microscopic mechanisms of action which (on average) do not break the microtubule left-right symmetry, or the real instability is correlated to vector-like order in the filaments, which is then lost in a later stage of pattern formation. Both possibilities, together with the mere question whether motor proteins play a role in pre-prophase band formation, are within the reach of a test with *in vivo* experiments, looking at the localization, activation, and binding properties of the molecular motors that co-localize with the microtubule interphase arrays of plants, and at the orientation of the filaments themselves. On the other hand, from the *in vitro* side, a combination of the experiment presented in Ch. 4 with the “self-organization assay” of Nédélec and others [36] is currently being tested.

In brief, although there are promising and intriguing indications, they merely form the basis for more work to come. Needless to say, the most effective way to proceed is that of mutual feedback between the different theoretical and experimental approaches. One question that could be asked now is: what are the alternatives to the mechanism described here? I will try to address this question in the next chapter, which attempts a more comprehensive discussion of the results of the last three.

5. *Mean Field Approach to Pre-prophase Band Formation.*

6. Discussion and Open Problems

The scope of this chapter is to draw some collective conclusions regarding the first part of the thesis, focusing on the possible relevance and implications of the results from the point of view of the biological system under examination, the microtubular cytoskeleton of interphase plant cells. In the past three chapters, I have discussed three examples of model systems inspired by three different hypothetical scenarios for plant cell microtubules, and approached with a mixture of theoretical and experimental tools. Although the results of the three models may have an interest independently from the biological inspiration, I would like to focus on how they can be used to contribute in a useful way to the biological scientific debate, and on the questions that this investigation opens on the system, which might stimulate further *in vivo* study. All the works presented share a common approach, whose spirit is to deal with a system as simplified as possible, in order to isolate a concept from the many interconnected ones one has to face when dealing experimentally with a real plant cell. The validity of these concepts and their relevance can to a certain extent be discussed in the light of the outcomes. This is attempted in section 6.1. Section 6.2, on the other hand, compares some alternative scenarios that can be put forward to explain the formation of the cortical microtubule array and the preprophase band in plant cells.

6.1. Considerations on the Scenarios

The main issue that emerges from the first scenario (Ch. 3) is that the data in our possession seem to indicate that the density of microtubules in a cortical array is close to the onset of an apparent nematic transition, where the filaments align purely on the basis of their excluded volume. On the other hand, the available *in vivo* data is too scarce to determine correlation between density and alignment. Although it is possible that these conclusions will be changed by a more extensive analysis of *in vivo* cortical microtubules, they do not allow to rule out the fact that excluded volume plays a role in the alignment of microtubules within the cortical array. In this picture it is assumed that the microtubules are sufficiently short so that the curvature of the plant cortical region and their elasticity are not relevant. This hypothesis would also require further experimental testing, as the only quantitative measure of cortical microtubule length dates back to 1977 [26]. In addition, the description of the interaction as a simple hard core potential is rather crude, and could be improved with the addition of a short ranged soft repulsive potential (no

6. Discussion and Open Problems

attraction is observed from microtubules polymerized *in vitro* from purified tubulin). This modification would unlikely change the qualitative conclusions, while possibly affecting the quantitative outcomes, and therefore the comparison with the *in vivo* system. Lastly, as more and more evidence supports the formation of long, crosslinked microtubule bundles [10], it must be said that the possible role of excluded volume is restricted to the early stages of interphase. In conclusion, while a mechanism of alignment based on excluded volume doesn't seem the best candidate to describe the alignment of cortical microtubules, the fact remains that the density of microtubules is such that they should feel this kind of interaction, which therefore may play some role.

Let us turn now to the second scenario, a model system for the dynamic spring hypothesis. The simple purified ingredients of the experimental model seem sufficient to reproduce coiling configurations similar to those observed in cells. The picture is consistent with the reversible disorganization observed in plant cells caused by the temperature-dependent disruption of microtubules or microtubule bundles induced by mutations in the MOR-1 gene [31], granted the assumption that the breakdown of long microtubule bundles in short fragments prevents the organization mechanism we described. On the other hand the experimental model does not account for the transverse arrangement of microtubules in the cortex of interphase plant cells. A theoretical approach that includes bending elasticity and confinement supports this evidence. Thus, it appears then that, on physical grounds, the implicit assumption in the dynamic spring hypothesis that a filament would form a transverse coil hides a mechanism that goes beyond the pure passive mechanical properties of the microtubules. There are numerous ways the cell could use to bypass this problem, mainly falling into two categories: either some configurations are rendered inaccessible, or active cell components make the transverse coil stable. This opens a new set of biological questions, that can be answered by means of *in vivo* and *in vitro* experiments.

Finally, the third scenario is the most interesting one. Its major result is that ring-like patterns can arise within a system with the geometric features of a plant cell, where cortical microtubules are confined in a thin layer between plasma membrane and vacuole. These patterns have the basic feature that the emerging alignment breaks nematic, but not vector symmetry, or, in more biological words, the filaments' plus ends are randomly placed, consistently with experimental observations on interphase cortical microtubules [85, 86]. This raises an important question about the symmetry of the microscopic components that drive preprophase band formation. Microscopic modeling that uses a simple picture of molecular motor activity [62, 77] is not able to reproduce an instability that does not also break vector symmetry. Only direct investigation on the living system can establish whether the nascent (and therefore supposedly close to the instability) preprophase bands or cortical arrays break this symmetry. If cortical microtubules would turn out as it seems to always retain random vector order during interphase, the mean-field description given in this thesis would be correct, but the microscopic drive should be identified. It could be due to more complex activity of motor proteins (e.g. hetero-complexes) or to other active forces. If on the other hand the instability would turn

out to depend on the vector order parameter, the mean-field description should be extended to include this last quantity, but the microscopic move would be directly comparable with the action of molecular motor activity through microscopic modeling. Furthermore, the mean-field approach introduced here provides a general framework for macroscopic descriptions of systems of filaments and active components, compatible with basic laws of physics. This can be used in many different contexts to generate different models, and classes of models, which describe the active organization of cytoskeletal filaments as a far-from-equilibrium process. These models can always be combined with a microscopic approach.

6.2. Other Scenarios for the Interphase Patterns

I will briefly review now some other scenarios that can be considered for the organization of microtubules in interphase, and discuss how they relate to the ones that I have presented.

Microtubule Alignment as a Reaction-Diffusion Process. A series of experiments by Tabony and collaborators [47, 48] has shown that purified microtubules polymerized in bulk at high (10 mg/ml) tubulin concentration align after a few hours. This ordering does not seem to occur if the sample is exposed to microgravity in the first minutes of the polymerization process. The argued explanation, substantiated by theoretical modeling [49], is based on a pattern formation mechanism that depends purely on the reaction-diffusion processes related to polymerization kinetics, whereby microtubules interact through the density fluctuations (“tubulin trails”) induced in the unpolymerized tubulin pool by their own subsequent (de)polymerizations, dictated in turn by dynamic instability. One might hypothesize that a similar mechanism, transported in a quasi-two dimensional geometry is operative for interphase cortical microtubules.

It is known [5, 88], that the effects of tubulin depletion can be relevant, especially in the so-called regime of unbounded growth of dynamic instability, which might be the case in the experiments of Tabony, where the concentration of tubulin is very high. It can also be argued that the depletion of the tubulin pool around a growing microtubule tip causes an enhancement in the catastrophe probability when two growing tips meet that can result in an effective suppression of growth for unparallel polymers. On the other hand, as free tubulin diffuses quite fast, these fluctuations can be very small. For example the sphere of 1% density depletion in the tubulin pool for a typical growing microtubule tip in a cell extract has a radius between 0.1 and $1\mu\text{m}$ [4]. For this reason, it can be easily argued that, although at very high density the interaction of nascent microtubule seeds through the free tubulin pool may play a role, the function of excluded volume once the filaments have polymerized should predominate for the alignment.

Furthermore, for the case of interest here, according to the parameters of dynamic instability measured on cortical interphase microtubules [34], the relevant regime is that of bounded growth, where the effects of tubulin depletion are neg-

6. Discussion and Open Problems

ligible. I have estimated using Brownian Dynamics simulations the role of the depletion between the growing tips for the same parameter range (system size, microtubule density, etc.) used for the model of rods in a quasi two-dimensional geometry presented in chapter 3, and with the dynamic instability parameters measured in [34]. The model used for dynamic instability in these simulations is that of reference [5]. Under the extreme assumption that each interaction between the 1% depletion spheres causes *deterministically* a catastrophe, this effect is always much smaller than excluded volume.

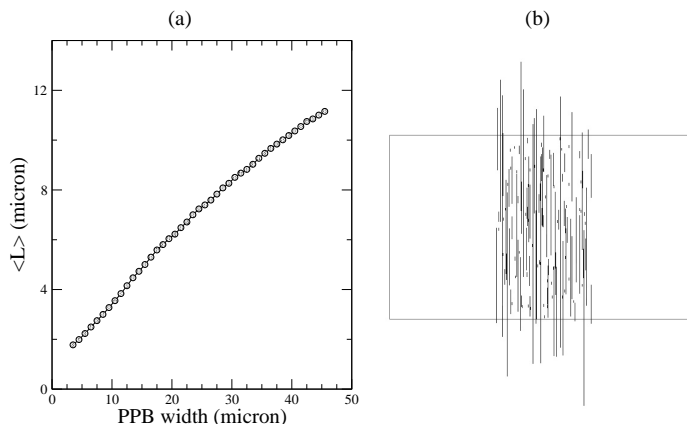


Figure 6.1.: (a) Estimate for microtubule steady-state average length as a function of preprophase band width. Both quantities are plotted in microns. The graph refers to a system of 200 parallel microtubules arranged randomly in a (topological) ring $30 \mu m$ in length having varying width. The parameters of dynamic instability are those measured by Vos and collaborators [34]. For this estimate, I assumed a five-fold increased catastrophe frequency for every interaction, defined as overlap the spheres constructed on two growing tips of estimated 1% density depletion in the tubulin pool. (b) Snapshot of a typical configuration

What is not under discussion is that microtubules, when packed at high densities, do interact through depletion of the tubulin pool. In particular, this must be true when they accumulate at short distances into the pre-prophase band. This may explain the observed increased catastrophe frequency observed in microtubules within the preprophase band [19]. The average length of microtubules would then decrease with the preprophase band width. I estimated this decrease by running simulations of randomly positioned parallel microtubules with dynamic instability, and periodic boundaries to mimic a ring (Fig. 6.1). These runs were performed with fixed microtubule number, and different widths of the ring, to determine the average microtubule length for different widths of the ring. The dynamic instability parameters were again taken from reference [34]. Interactions between the 1% depletion spheres around growing tips was assumed to cause a 5-fold increase in the catastro-

the frequency. As expected, microtubule average length in a steady state decreases linearly with the width of the ring. On the other hand, the increased *rescue* frequency observed in nascent preprophase bands cannot be explained by the same argument. It could be a way cells employ to stabilize these patterns through regulated microtubule-interacting molecules. The sudden disruption of preprophase bands after nuclear envelope breakdown might be a sign that this stabilizing signal has ceased.

Reaction-Diffusion and Preprophase Band Formation. Reaction-diffusion nonequilibrium mechanisms could also be used to build alternative explanations for the formation of the preprophase band. One successful example that bears many analogies with the plant system is the case of placement of the Z-ring in *Escherichia Coli* [89, 90]. This ring, which consists of a protein homologue of tubulin called FtsZ, is involved in determination of the division site, and therefore is an essential part of bacterial cell division. The placement of the division site does not depend on the Z-ring itself, but on the proteins MinC, MinD, and MinE, which suppress FtsZ polymerization at noncentral membrane sites. The Min proteins undergo a highly dynamic localization cycle that depends on the kinetics of chemical reactions among themselves, during which they oscillate between the membrane of both cell halves. Theoretical models [43, 45, 44] have confirmed the feasibility and robustness of this scenario. In this framework, for example, it is easy to design a minimal set of reactions able to place the mid-point of a confining cell with sufficient precision, which would in our case explain how the preprophase band forms (in most cases) in the middle of the plant cell. Similar patterning mechanisms have been observed also in eukariotic cells, and in connection with the microtubule cytoskeleton [46, 91]. By adopting this point of view, the focus for the cytoskeletal organization is diverted from the forces and the mechanics of the cytoskeleton itself to the reaction dynamics of cytoskeleton-related regulatory molecules. Whether one of these two, or a combination of both, complementary descriptions is the most apt to describe preprophase band formation is still an open question.

Search and Capture Mechanisms for Preprophase Band. Recently proposed by Vos and collaborators [34], this mechanism is inspired by a model of chromosome-spindle interaction behavior. It is based on the observation that during preprophase band formation, the dynamic instability of the cortical microtubules outside the preprophase band increases significantly, but the microtubules do not become shorter. The basic idea is that because this regulation of dynamic instability causes the cortical microtubules to modulate their lengths with higher frequency, they can “search” more effectively for the preprophase band, which provides a “sticky target” because of its internal microtubule cross-linking activity. This explains why microtubules gradually disappear from the surrounding cortex and aggregate to the forming preprophase band, and the vector disorder of the incorporated polymers. However, it does not seem to provide an explanation for the instability that drives to preprophase band formation, the narrowing of the ring with time (intuition would suggest that according to this model the width of a pre-

6. Discussion and Open Problems

prophase band should increase with time), and its positioning in the middle of the cells. In any case, to allow a thorough exploration of its consequences, this proposed mechanism should be substantiated by more detailed estimated or proper modeling. The implication of microtubule stable crosslinking gives rise to a new set of questions that can be investigated by *in vivo* and *in vitro* experiments, regarding for example why this crosslinking does not directly involve all the microtubules in a cell, how the activity of the crosslinkers is able to avoid the formation of a gel-like randomly connected network, and the kinetics of bundle formation.

Part II.

**Hydrodynamics of Flexible
Rod Based Microorganism
Motility. A Simulation
Study.**

7. Overview of the Problems

As pointed out by Purcell in his Lecture “Life at low Reynolds numbers” [92], microorganisms experience an environment quite different from our own. In particular, because of their small size (of the order of microns), inertia is, to them, essentially irrelevant. We are all familiar with the concept of inertia. It is the tendency of things in motion to remain in motion. If, for example, you tore this page from the thesis (hopefully having read it first), screwed it up into a ball and threw it, you would expect it to advance for a few meters. Inertia keeps it moving until the friction exerted by the air (or the floor once it has landed) brings it to a halt. Let us now keep our physical size fixed at a couple of meters and see what would happen if we experienced the same environment as a microorganism. As long ago as the 19th century, Reynolds showed that, as far as the dynamics of a fluid are concerned, scaling down a problem (decreasing the characteristic length scale) is, in dimensionless terms, equivalent to increasing the viscosity. That is, if we wanted to repeat our paper throwing experiment in a world parametrically equivalent to that of the micro-organism we would have to immerse ourselves in a fluid a million times more viscous than air. If we also take into account that we (and this thesis) are much denser than air, whereas a micro-organism is typically equivalent in density to its surroundings, we find the following. Transforming the microscopic world to our macroscopic dimensions and repeating the experiment, we could propel our projectile about $10^{-9}m$. That is, we could throw the screwed up paper (or the whole book) a few atomic distances. In an inertialess world it is hard to shake off your environment.

The fact that inertia is irrelevant for micro-organisms makes it difficult for them to move. Many propulsive mechanisms that are perfectly viable on our scale will not work on a mesoscopic scale. This is because of some particular facts that characterize these systems. When describing a macroscopic body in a fluid, the equations of motion governing the body (coming from Newton’s law) are time-reversible, while those governing the surrounding fluid are irreversible. For a mesoscopic body at low Reynolds number, it is just the opposite: the (approximate) equation of motions for the body are irreversible, while those governing the motion of the surrounding fluid become time reversible. This last fact bears the consequence that any reciprocal motion produces no net propulsion. A popular example is that of the stiff one-armed swimmer, a chimerical rod-like organism that tries to move by waving its body back and forth. However, in the absence of inertia any net force generated by one half of the stroke will be equal and opposite to the force generated during the remainder. The total will be zero and the stiff one armed

7. Overview of the Problems

swimmer, in the absence of inertia, goes nowhere. There are two obvious strategies for avoiding this problem. One is to introduce flexibility. If the one-armed swimmer has a flexible arm the shape need not be reciprocal during a cycle. Net propulsion can be generated. Another solution is to have an appendage execute some non-reciprocal motion. That is, to generate motion with some “handedness”. The classic example of this, and the one used by most bacteria, is to rotate a chiral tail [93]. Rotation of a chiral tail again breaks the symmetry of one cycle and has the potential to generate net motion.

In this second part of the thesis I will focus on problems related to the hydrodynamics of elastic mesoscopic filaments. The underlying motivation of these studies is the active motion of flagella and cilia (Fig. 7.1). Cilia and flagella are 10-50 μm long, 100 nm thick protrusions of the eukaryotic cell membrane that are able to generate motion [7]. The function of flagella is to thrust the cell body in the fluid environment. Cilia are used by the cells or tissues for self-propulsion or to stir the surrounding fluid. A cilium has the same internal structure (the axoneme) as a eukaryotic flagellum, containing an arrangement of nine microtubule doublets attached to a basal body anchored to the cell membrane. A complex, symmetric frame of protein bridges and links among the doublets gives elastic properties to the whole structure. Molecular motor activity provides the energy source for the internal engine which produces the active bending [94] that characterizes these motile assemblies.

Because of their size and typical velocities, the motion of these filaments is nearly always in the low Reynolds number regime. Cytoskeletal filaments are involved in cellular and microorganism motility. Perhaps the most widely known example is that of the flagellum of a sperm cell, that enables it to swim along the ovaric tubes. The internal drive of a flagellum, however, is rather complicated [94]. In spite of this, the problem of modeling theoretically eukaryotic flagellar and ciliary motility starting from the internal degrees of freedom has received much attention during the past fifty years. Early attempts date back to the fifties and sixties of the past century, with the works of Gray and Hancock [95] and Machin [96, 97], and were followed by abundant work in the seventies [98, 99, 100, 101], eighties [102, 103, 104, 105], and in the past fourteen years [106, 107, 108, 109, 110, 111]. Unfortunately, this wealth of different models and theoretical results hasn't yet evolved into a unified picture of the problems, possibly because many aspects of the system remain unclear from the experimental point of view.

On the other hand, modern micromanipulation techniques, such as optical and magnetic trapping, open up the possibility of perturbing otherwise passive filaments with a simplified and controlled drive (cf. Fig 7.2). This provides potentially useful model systems for which one may study the hydrodynamic fundamentals of motility, separating them from the equally complex problem of the generation of the internal drive.

I will analyze simplified systems of this kind, with the main purpose of elucidating some facts concerning the hydrodynamics of swimming. As we will see, bending elasticity plays an important role in this analysis. For many biologically important filamentous assemblies, elasticity is crucial. Their typical lengths (mi-

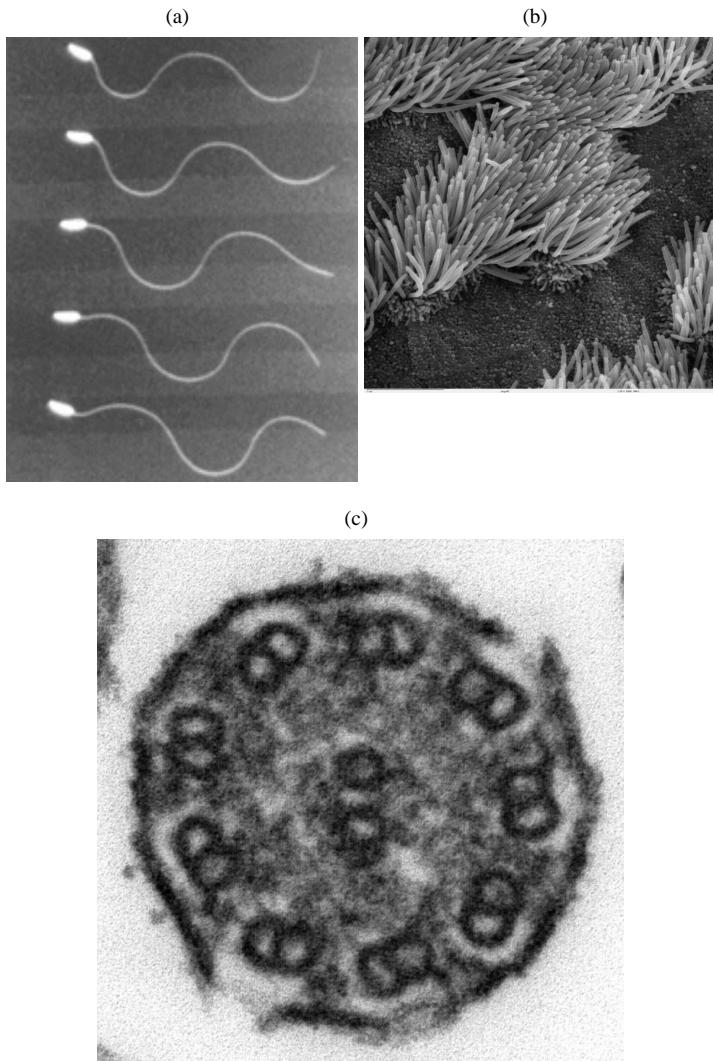


Figure 7.1.: Cilia and flagella. (a) Video microscopy snapshots of a swimming sperm cell, showing the beating movement of the flagellum (C.J. Brokaw, California Institute of Technology). (b) SEM image of cilia in the mammalian lung, the size of the picture is about $25 \times 25 \mu\text{m}$ (C. Daghlian, Dartmouth College, USA). (c) TEM image of the cross section of a 100 nm ciliary axoneme. The nine microtubule doublets and the protein bridges are visible (L. Howard, Dartmouth College, USA).

Strongly focused laser

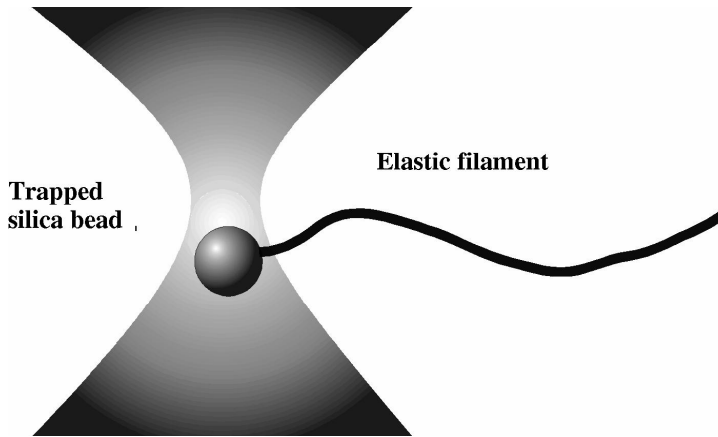


Figure 7.2.: Schematic of a micromanipulation experiment that allows one to apply a controlled drive to an inert filament [112].

crons) are comparable with the scale on which rigidity prevents them from collapsing. The cytoskeletal filaments actin and microtubules fall in this category, as do cilia and flagella, the latter being motile assemblies of microtubules and other proteins. The question is then what the conditions are under which these elastic linear bodies can generate swimming motion under simple drives.

In chapter 8 I describe a method, based on techniques used in molecular dynamics, for simulating the inertialess dynamics of an elastic filament immersed in a fluid. The model is used to study the “one-armed swimmer”. That is, a flexible appendage externally perturbed at one extremity. Simple active driving mechanisms could be an oscillating constraint on the end position, an oscillatory torque applied at one extremity, or a rotating constraint. I will consider all three. This system can be regarded as the simplest example of what has been called *elastohydrodynamics* as it involves the balance of viscous and elastic forces. The case of driving torque is a more plausible biological mechanism as it involves no net external force. For small amplitude motion the simulations will confirm theoretical predictions that, for a filament of given length and stiffness, there is a driving frequency that is optimal for both speed and efficiency [113]. However, I will show that to calculate absolute values of the swimming speed one needs to slightly modify existing theoretical approaches. For the more relevant case of large amplitude motion, while the basic picture remains the same, the dependence of the swimming speed on both frequency and amplitude is substantially modified. For large amplitudes we will see that the one armed swimmer is comparatively neither inefficient nor slow. This begs the question of why there are little or none one-armed swimmers in nature.

In chapter 9 I present a simple way to refine the description of the elastohydrodynamic problem for a filament by incorporating hydrodynamic interactions, which can make an important difference, particularly if one wishes to describe

many-filament systems. This extended model is first implemented on the problem of sedimentation, showing both validating agreement with established results and new, interesting behavior. Hydrodynamic interactions are able to excite elastic instabilities in a uniformly driven filament, and to interact with the hydrodynamic degrees of freedom causing the body to place itself transverse to the driving field. In a second step, I apply the extended model to a one-armed swimmer. However, this does not lead to any new insight, showing good agreement with the results of the simpler model. This can be seen as a further validation of the method which includes hydrodynamic interactions, whose real potential lies in the possibility of investigating cooperative effects in many-body problems.

7. *Overview of the Problems*

8. Dynamics of a Driven Semiflexible Polymer at Low Reynolds Number

8.1. Introduction

The model I will present in this chapter solves numerically the equations of motion of a discretized elastic filament immersed in a low Reynolds number fluid. Any form of internal and external forcing can be imposed but I will restrict the discussion here to an active force, acting on one extremity, that is periodic in time. Namely, an oscillating force, an oscillating torque, a rotating torque. All the driving forces that I will consider can be realized experimentally on inert mesoscopic semiflexible (bio-)filaments by means of micro-manipulation techniques such as optical or magnetic trapping. These simple drives, compared to the biological ones of cilia and flagella have the advantage of being free from more or less complex feedback mechanisms, which couple the driving field to the elastic and hydrodynamic degrees of freedom. It is therefore possible to separate the hydrodynamic problem of swimming from that of the generation of the internal drive.

For these relatively simple model systems, the filament dynamics is determined by the interplay of elastic and hydrodynamic forces. There has fairly recently been theoretical progress in solving analytically the “hyperdiffusion” equation that, in the limit of small amplitude motion, describes the movement of such a filament [113]. The simulation introduced here is designed to be minimal, but at the same time to overcome the main limitation of the analytical theory, which is valid only for nearly straight filaments. In contrast with the theory, the simulation retains all the nonlinearities of the body equation of motion, and works for arbitrary filament shapes, in two and three dimensions. For most of the problems we are concerned with here, the planar driving forces produce planar motions. However, as I will show, the model applies equally well this not being the case.

As in the analytical theory, I will keep throughout this chapter the hydrodynamics to its minimal level of description, that is, the approximation of slender body flow [114], where the local velocity-force relation is reduced to a simple expression in terms of friction coefficients that are shape and position independent. They do nonetheless reflect the difference between friction transverse and longitudinal to the filament. A more sophisticated treatment of hydrodynamic forces will be

introduced in the next chapter. Section 8.2 covers the model adopted and the implementation of the simulation. Section 8.3 contains the results for planar active forces and their implications, while section 8.4 briefly outlines the results for a simple three-dimensional drive, inspired by the motion of bacterial flagella.

8.2. Model and Simulation

Considering a continuous description of the filament in space and time, one can specify this at any given instant t by a curve $\mathbf{r}(s,t)$, giving a point in space for any value of the arclength parameter s (Fig. 8.1).

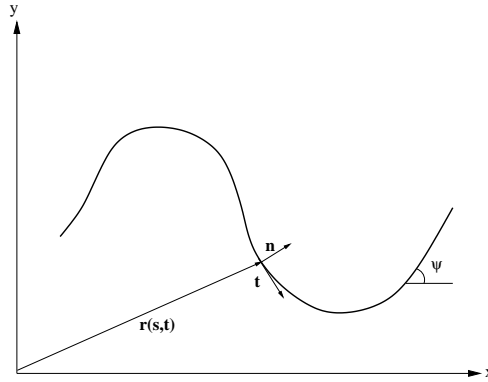


Figure 8.1.: Curve describing the shape of the filament. $\mathbf{n}(s,t)$ and $\mathbf{t}(s,t)$ are the local normal and tangent unit vector respectively. $\psi(s,t)$ is the angle formed with the x axis.

To describe the dynamics one needs the local forces acting on the filament. The latter are related to the energy of the model system. Specifically, they are

- i. A bending elasticity, described by the Hamiltonian

$$H = \frac{1}{2}k \int_0^L C(s)^2 ds , \quad (8.1)$$

where $C(s) = \left(\frac{\partial^2 \mathbf{r}}{\partial s^2} \right)^2$ is the local curvature and k the stiffness.

- ii. A constraint of inextensibility, which can be expressed in terms of the tangent vector as

$$\left| \frac{\partial \mathbf{r}}{\partial s} \right| = 1 ,$$

and imposes the condition that the filament is, to a first approximation, inextensible.

iii. An over-damped (negligible mass) equation of motion, which can be written as

$$\partial_t \mathbf{r}(s, t) = - \left(\frac{1}{\xi_{\parallel}} \hat{\mathbf{t}}\hat{\mathbf{t}} + \frac{1}{\xi_{\perp}} \hat{\mathbf{n}}\hat{\mathbf{n}} \right) \frac{\delta H}{\delta \mathbf{r}(s)}. \quad (8.2)$$

Here, following slender-body theory, the effect of the surrounding fluid is taken as a drag force that is proportional and opposite to the local velocity. This is anisotropic due to the elongated shape of the filament. I therefore require a longitudinal friction coefficient ξ_{\parallel} associated with the projector $\hat{\mathbf{t}}\hat{\mathbf{t}}$ along the tangent vector \mathbf{t} , and a transverse coefficient ξ_{\perp} acting along the normal vector \mathbf{n} .

Accordingly, one obtains two equations of motion, one for the evolution of the filament shape, and the other for the tension force $\tau(s, t)$, that enforces locally the inextensibility constraint. Expressing the curve shape as the angle $\psi(s, t)$ that its local tangent forms with a fixed $\hat{\mathbf{x}}$ direction, one can write these equations as (see [108]):

$$\partial_t \psi = \frac{1}{\xi_{\perp}} (-k \partial_s^4 \psi + \tau \partial_s^2 \psi + \partial_s \psi \partial_s \tau) + \frac{1}{\xi_{\parallel}} \partial_s \psi (k \partial_s^2 \psi \partial_s \psi + \partial_s \tau), \quad (8.3)$$

and

$$\partial_s^2 \tau - \frac{\xi_{\parallel}}{\xi_{\perp}} (\partial_s \psi)^2 \tau = -k \partial_s (\partial_s \psi \partial_s^2 \psi) + \frac{\xi_{\parallel}}{\xi_{\perp}} \partial_s \psi (-k \partial_s^3 \psi). \quad (8.4)$$

The two nonlinear equations above have then to be solved subject to appropriate boundary conditions. For example, no external forces and torques for a free tail. For the wiggling problems I examine here, the non-equilibrium drive (oscillating end position or torque) is, in these terms, simply a time-dependent boundary condition. Through a functional expansion about the obvious solution for zero drive $\psi_0(s, t) = 0$, $\tau_0(s, t) = 0$,

$$\begin{aligned} \psi &= \varepsilon \psi_1 + \varepsilon^2 \psi_2 + \dots \\ \tau &= \varepsilon \tau_1 + \varepsilon^2 \tau_2 + \dots \end{aligned} \quad (8.5)$$

it is straightforward to obtain, to second order in ε the (decoupled) equations

$$\partial_t \psi_1 = - \frac{k}{\xi_{\perp}} \partial_s^4 \psi_1$$

for ψ_1 and

$$\partial_s^2 \tau_2 = -\partial_s (k \partial_s \psi_1 \partial_s^2 \psi_1) - \frac{\xi_{\parallel}}{\xi_{\perp}} (k \partial_s \psi_1 \partial_s^3 \psi_1)$$

for the tension. Furthermore, expressing the shape of the filament in terms of the transverse and longitudinal “absolute” displacements $u(s, t)$ and $h(s, t)$ from the direction $\hat{\mathbf{x}}$ of the filament’s resting position, one gets to the equation

$$\xi_{\perp} \partial_t h = -k \Delta^2 h \quad (8.6)$$

8. Dynamics of a Driven Semiflexible Polymer at Low Reynolds Number

for the time evolution of h to second order in ε . This “hyperdiffusion” equation has to be solved subject to appropriate boundary conditions, which may correspond to different forms of external driving.

In the simulations I use a particle model to solve Eqs. (8.3) and (8.4) numerically using an approach similar to molecular dynamics. Time is discretized and the filament is described as a set of n point particles rigidly connected by $n - 1$ “links”. The interaction between the particles is constructed so as to reproduce the appropriate collective behavior. For convenience in implementing the algorithm, I do not simulate the over-damped motion, given by Eq. (8.2) directly. This would correspond to the zero mass case. Rather, I solve the damped Newton equation for an object with “small” total mass m . By making the mass small enough one can reproduce the required inertialess mass independent behavior [115]. In all cases it was nonetheless checked, by varying the mass, that the results were indeed independent of mass.

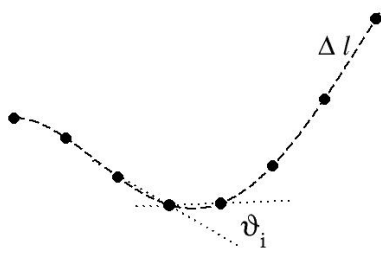


Figure 8.2.: Discretization of the filament.

The bending forces acting on the individual particles are defined as follows. Considering three consecutive discretization points, their positions will lie on one unique circle of radius, R_i ,

$$C_i^2 = \left(\frac{1}{R_i} \right)^2 = \frac{2}{\Delta l^2} (1 - \cos(\theta_i)) ,$$

where $\Delta l = L/(n - 1)$ is the link length and θ_i the angle between two links at the position of bead i . One can introduce a bending potential U_i of the form

$$U_i = A(1 - \cos(\theta_i)) ,$$

so that the total bending energy will be

$$H = \sum_{i=2}^{n-1} U_i = A \sum_{i=2}^{n-1} (1 - \cos(\theta_i)) ,$$

which can be compared with a discretization of the integral in Eq. (8.1)

$$H = \frac{k}{2} \Delta l \sum_{i=2}^{n-1} (C_i^2) .$$

This leads to the identification $A = \frac{k}{\Delta l}$. A more sophisticated approach [116], where the problem is mapped onto the worm-like chain model of Kratky and Porod [117], leads to a slightly different expression, $A = \frac{n-1/2}{L} k$, which is equivalent to the former in the infinite n limit, but leads to faster convergence in the results as the number of discretization point particles is increased. I therefore chose to adopt it.

The inextensibility constraint is implemented by introducing equal and opposite forces along the links between particles. The magnitude of the forces is computed by imposing a fixed distance Δl between consecutive beads at each time step. This is a straightforward matter from the computational point of view, as it involves only the inversion of a tridiagonal matrix [118, 119]. However, it must be noted that this simple implementation is valid as long as thermal fluctuations are neglected. In fact, the equilibrium statistical properties of a filament with rigid inextensibility constraints are not the same as those of a system with extensible constraints in the limit where the extensibility goes to zero. In a fluctuating thermodynamic system a correction has to be made for this [120, 121].

The viscous drag forces acting on the particles of the model filament are taken as $F_{ij} = -\delta_{ij}(\xi_{\parallel} \hat{\mathbf{t}} + \xi_{\perp} \hat{\mathbf{n}})\mathbf{v}$, where $\hat{\mathbf{t}}$ and $\hat{\mathbf{n}}$ are respectively unit vectors tangent and normal to the filament, ξ_{\parallel} and ξ_{\perp} are the longitudinal and transverse friction coefficients, and \mathbf{v} is the local velocity. This means that hydrodynamics is approximated as a local effect on the filament such that the hydrodynamic interaction between different points along the curve does not vary. The global shape of the curve enters only through the anisotropy of the viscous drag coefficients acting on individual points. The ratio of the two coefficients depends on the geometric details of the filament analyzed. For cilia, flagella, or cytoskeletal filaments, its value is typically taken between 1.4 and 2 [122]. I chose to adopt a value 1.5 in most of the simulations, while also examining the cases where the two drags are equal or their ratio is less than unity. The time evolution is evaluated in a molecular dynamics-like fashion, with the only slight subtlety that the Verlet algorithm has to be modified to allow for the velocity dependent anisotropic viscous force [115]. Finally, the active drive at the head is simply implemented as a constraint on the first (for oscillating constraint) or first two (for periodic torque) particles. For example, this is $y_1 = h_0 \cos(\omega t)$ for the oscillating constraint, and the periodic torque, $T_x = B \sin(\omega t)$ is realized as a couple of forces applied to the first two beads. Here ω is the driving frequency.

8.3. Wiggling Motion

Let us consider now the flexible one-armed swimmer. That is, an elastic filament that is wiggled at one end. If the filament were rigid, the reversible motion of

8. Dynamics of a Driven Semiflexible Polymer at Low Reynolds Number

the surrounding fluid would ensure that this mechanism generates no propulsion (the “scallop theorem” as Purcell termed it). However, the flexibility of the arm breaks the time reversal symmetry for the motion of the assemblage. This makes propulsion, in principle, possible. For any microscopic filament the factors that determine its dynamic behavior are the same. Namely, the equations of motion will be essentially inertialess. The motion itself will be determined by a balance between forces driving the filament, friction forces exerted as the surrounding fluid opposes any motion, and bending forces that try to restore the (straight) equilibrium state. For relatively simple model systems, there has recently been theoretical progress in solving analytically the “hyperdiffusion” equation that, in the limit of small amplitude motion, describes the movement of such a filament. Wiggins and Goldstein [113] considered the motion of a single filament driven at one end by an external perturbation. Their analysis emphasized that there are two very different regimes; one where bending forces dominate and the filament behaves like a rigid rod, and a second where the viscous damping of the fluid has the effect of suppressing the propagation of elastic waves. For the one armed swimmer, this leads to an optimal set of parameters that maximize either the swimming speed or swimming efficiency. The same analysis gives predictions for the shape of such a wiggled filament that can be compared with the response observed in a micro-manipulation experiment [112]. By comparing experimental results with theory, they were able to calculate the persistence length of the filament.

To summarize the predictions of the theory, for a given amplitude of driving the remaining parameters can be grouped together to define a dimensionless “sperm number”,

$$Sp = \left(\frac{l^4 \omega \xi_{\perp}}{k} \right)^{\frac{1}{4}}, \quad (8.7)$$

where l is the length of the filament and ω the wiggling frequency.

This characterizes the relative magnitudes of the viscous and bending forces. A low value implies that bending forces dominate, a high value viscous forces. As a function of the Sperm number, the theory predicts

- both the swimming speed and efficiency (defined as the amount of energy consumed, relative to the amount of energy required to simply drag a passive filament through the fluid at the same velocity), go to zero as Sp goes to zero. This is the stiff limit where the motion is reversible and the scallop theorem applies
- at a sperm number $Sp \simeq 4$ there is a maximum in the both the swimming speed and efficiency (although not at exactly the same value of the sperm number)
- at high sperm numbers a plateau region where the speed and efficiency become independent of Sp , albeit at values lower than the peak.

8.3.1. Small Amplitude Motion

Wave Patterns

Using the "sperm number" Sp defined in section 8.3, we can characterize the relative magnitude of the viscous and bending forces. To recapitulate, a low value of Sp indicates that bending forces dominate, whereas for low values the dominant forces are viscous. One reason for defining this number comes from the solution of Eq. (8.6) [113, 115]. Sp can be interpreted as a rescaled filament length, where the rescaling factor is a characteristic length $l_* = \left(\frac{k}{\omega \xi_{\perp}}\right)^{1/4}$ that can be used to non-dimensionalize the equation. This rescaled length was first defined in the context of semiflexible polymer fluctuations, by Farge and Maggs [123, 124]. In the simulation, the sperm number was varied in most cases by varying the bending modulus so that the Reynolds number was fixed at a low value. Both for the oscillating constraint and oscillating torque I recover the fact that the dynamic response, for a fixed driving amplitude, is solely dependent on Sp .

In Fig. 8.3 I have plotted the wave patterns for the filament at different values of Sp . These results were obtained using the oscillating constraint. That is, the transverse position at the wiggled end is forced to be sinusoidal in time. The amplitude of the motion is small, the maximum displacement being 1% of the filament length. The pictures can be interpreted as "stroboscopic snapshots" of the filament's motion. For small Sp , bending forces dominate and the stiff filament pivots around a fixed point. This motion is virtually symmetric with respect to time inversions ("reciprocal"). As Sp increases a (damped) wave travels along the filament and time reciprocity is broken. For increasing values of Sp , viscous forces overcome elastic forces and the characteristic length scale of damping of the traveling wave becomes smaller. This requires that the spacing between the beads in the discrete model must also be reduced to give a fixed degree of accuracy. The number of beads in the model (or equivalently the inverse bead spacing) were thus increased with increasing Sp to ensure that the results are within a percent of the true, continuum, values. The oscillating torque gives qualitatively similar results. All these results are in agreement with the analytical findings of Wiggins and Goldstein [113] in the small amplitude approximation. The agreement is also quantitative.

Swimming

From the simulation it is also possible to compute the velocity and efficiency of the swimming as a function of Sp . I define swimming of the immersed object as the generation of motion, through modifications of shape, in the direction along which no *external* force acts. Both the speed and efficiency, as Wiggins and Goldstein predict, display an optimum value at intermediate (but different) values of Sp . Subsequently they reach a plateau as viscous forces begin to dominate (Sp increases).

According to the "scallop theorem" of low Reynolds number hydrodynamics, reciprocal (time reversion invariant) motion generates no swimming [92]. This is a

8. Dynamics of a Driven Semiflexible Polymer at Low Reynolds Number

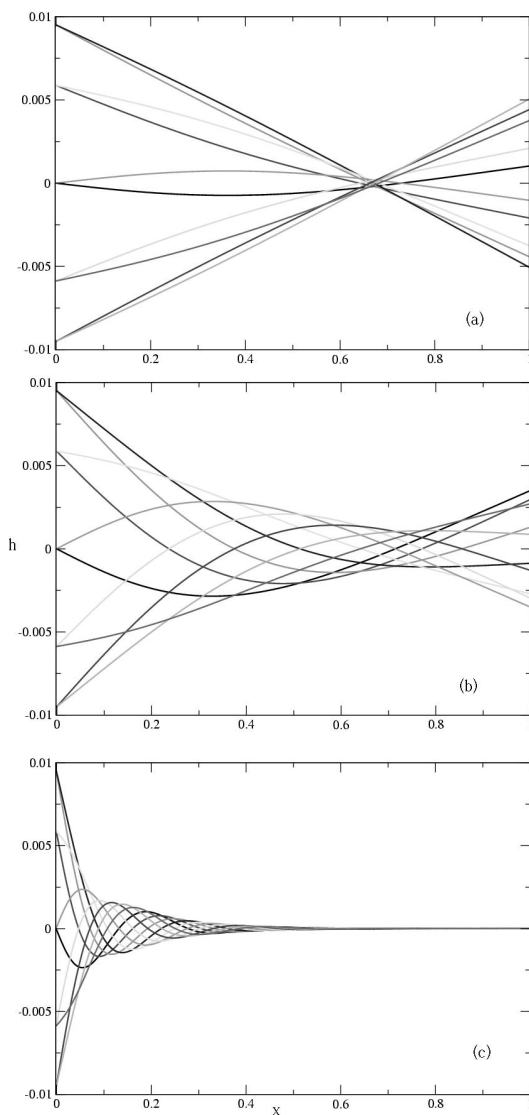


Figure 8.3.: Waveforms of the filament oscillations for different values of Sp . (a) Low Sperm number ($Sp= 2.46$). The motion consists of pivoting oscillations about a fixed point. (b) Intermediate Sperm number ($Sp= 4.29$). A damped wave propagates along the filament making the movement non-reciprocal in time. (c) High Sperm Number ($Sp= 22.61$). The propagating wave is damped within a length that becomes smaller with increasing Sp .

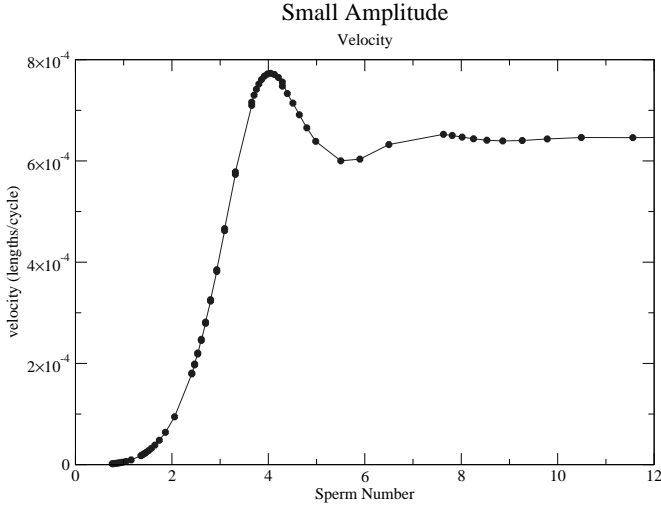


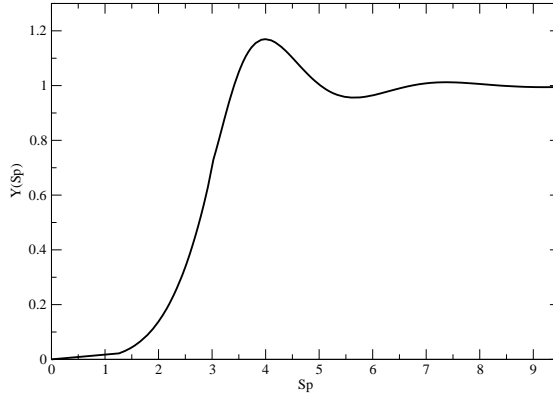
Figure 8.4.: Propulsive velocity as a function of Sperm number for small amplitude oscillation ($h_0 = 0.01l$) of the constraint at the "head" end of the filament. The function goes as the fourth power of Sp for small values of this number, reaches an optimum, then relaxes to a plateau.

consequence of the time-reversibility of Stokes flow and sets an important condition for the ability of microorganisms to swim. In our case, this implies that we should expect no swimming as Sp approaches zero and the motion approaches reciprocity. This is confirmed by the result in Fig. 8.4. The optimum of the velocity is thus the result of a trade-off between non-reciprocity of the motion and damping of the traveling wave.

At this point we should also be able to compare the results quantitatively with those obtained analytically using the approximation of small deviations. However, in this respect the theoretical analysis is somewhat incomplete. Computing the time average of the force, as in [125, 113], yields the expression

$$\bar{F} = \frac{h_0^2 \xi_{\perp} \omega}{4\sqrt{2}} Y(Sp),$$

where $Y(Sp)$ is a scaling function that can be computed exactly (Fig. 8.5). This expression depends only on the transverse friction coefficient and does not reduce to zero when $\xi_{\perp} = \xi_{\parallel}$. As such, it is impossible to relate this to the swimming speed. This follows from the fact that if the condition $\xi_{\perp} = \xi_{\parallel}$ is satisfied there can be no swimming. It is easy to show this must be the case, as a consequence of Newton's third law. The main reason is that, if one considers one particle (i.e. a short piece of filament), the effective viscous drag that it experiences at any moment in time is decoupled from the local configuration of the filament if there is no anisotropy in the friction coefficients. Averaged over one cycle, this always leads, effectively, to


 Figure 8.5.: The function $Y(Sp)$ from Wiggins *et al.*.

reciprocal motion. All the forces sum to zero so there can be no displacement. This is shown more formally in the Appendix. Furthermore, the simulations do indeed yield no average velocity if the two friction coefficients are equal (I use this to check that there is no “numerical” swimming, due to the accumulated errors in the simulation). To correct for this anomaly I used the theory and computed, following the procedure outlined in [108], the time average of the swimming velocity given the analytical solution for the shape [125]. This yields (see the Appendix)

$$v = h_0^2 \left(1 - \frac{\xi_{\perp}}{\xi_{\parallel}} \right) \frac{\omega}{4\sqrt{2}L} Y(Sp), \quad (8.8)$$

where $Y(Sp)$ is again the scaling function specified by Wiggins and Goldstein in computing the average force (Fig. 8.5). Note that this expression (Eq. 8.8) predicts no swimming when

- $Sp = 0$ and the motion is reciprocal in time (see fig. 2)
- When the two drag coefficients ξ_{\perp} and ξ_{\parallel} are equal.

consistently with both the scallop theorem and Newton’s third Law. It also predicts a change in the swimming direction if the friction coefficients are interchanged. Curiously, this reversal of direction has a biological analogue in the organism *Ochromonas* which has a flagellum decorated by lateral projections (mastigonemes) and swims in the same direction as that of the propagating wave. The body follows the flagellum, instead of preceding it as in sperm cells (see Ref. [94], p.11).

Comparing the modified analytical expression for the swimming speed with the simulations, the essential features predicted are obviously present. Both approach

zero as Sp^4 for small Sperm numbers, but display a maximum with increasing sperm number. In fact, a careful analysis shows that the agreement, in the small amplitude limit, is exact. The presence of a plateau at high Sp is hard to interpret, in the sense that it predicts velocities for even the “infinitely floppy” filament, where the wave pattern is completely damped in an infinitely small region close to the driven extremity. However, in the simulations the velocity drops only when the size of this damping region is comparable to the distance between two subsequent discretization points, so I have to confirm the analytical result and explain this oddity, as we will see, as a feature of the small deviation approximation.

8.3.2. Large Angular Deviations

The model previously shown contains the full nonlinear model for the dynamics of the filament, its only limitation being the discretization of space and time. Therefore, it is interesting to use it to investigate the limitations of the analytical model when the motion involves shapes that deviate significantly from straight. This is also closer to a real experimental (or biological) situation. The shapes often cannot be described by a function, as the displacement from the horizontal axis is not single-valued. This can be observed in Fig. 8.6, where I show an example of wave pattern for the case of oscillating large amplitude constraint. In this case, the maximum transverse displacement is 60% of the tail length. Looking at this figure, it is obvious that the behavior predicted by Eq. (8.6) will be substantially modified.

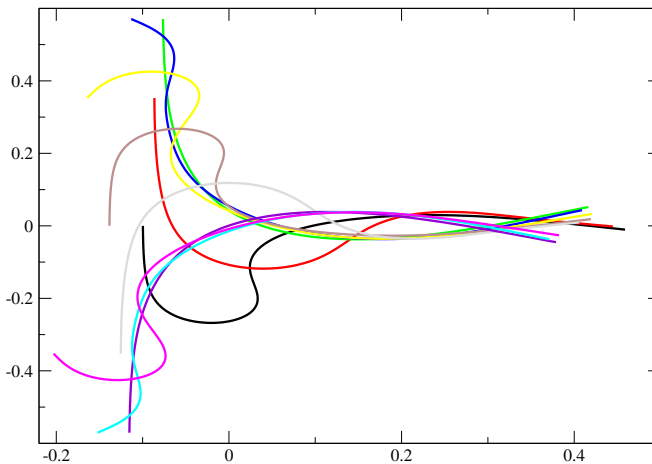


Figure 8.6.: Wave patterns for the case of an oscillating constraint with amplitude $h_0 = 0.6 l$ at $Sp = 4$.

The first notable area of disagreement is at high values of the Sperm number ($Sp \gg 1$) where I no longer find a plateau but a slow and steady drop in both speed and efficiency (Fig. 8.7). This effect is clearly a consequence of the non-negligible amplitude of the motion because for smaller amplitudes a plateau is indeed reached.

8. Dynamics of a Driven Semiflexible Polymer at Low Reynolds Number

This is a limitation of the theory, as large amplitude motions differ from the small amplitude limit. Further the results for a dimensionless amplitude of 0.25 display a transient plateau that subsequently decays to zero. This implies that for any finite amplitude the dimensionless swimming speed always goes to zero for large enough Sp . The smaller the amplitude the longer the plateau persists, but only for negligible amplitude is the asymptotic behavior reached. It should be noted that Figs. 8.4 and 8.7 should be interpreted with care. The swimming velocity is plotted in units of the fraction of the length per cycle. To obtain absolute swimming speeds, for a tail of given length and stiffness, we would need to multiply this dimensionless swimming speed by the frequency. The frequency itself is proportional to Sp^4 so a plateau in these plots still implies a swimming speed increasing proportionally with ω . The drop from the plateau means that the actual swimming speed will increase with frequency, but a slower rate. Thus, in practice the one armed swimmer can go as fast as it likes by wiggling fast enough.

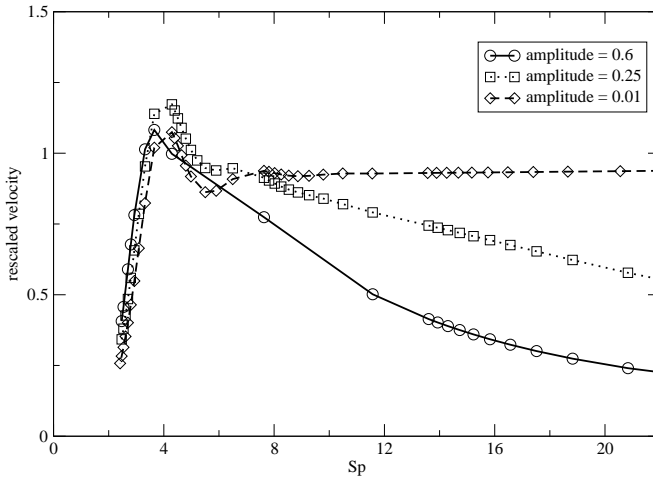


Figure 8.7.: Velocity versus sperm number for different values of the amplitude h_o in the case of oscillating constraint. The velocities have been rescaled to show the drop of the plateau.

Secondly, I find that the dependence of the optimum swimming speed, which Eq. (8.8) predicts as the square of the amplitude of the oscillating constraint, becomes linear for higher amplitude oscillations (Fig. 8.8). Thus far, I have not been able to show why this is the case, but I believe it is related to the following. For small amplitude motion the elastic wave simply propagates along an essentially straight filament. As the amplitude increases, this is no longer true because the filament itself is significantly bent and, so far as the damping is concerned, it is the distance along the filament that is relevant. This quantity can be significantly different from the absolute distance, seemingly leading to an increase in the effective length of the filament.

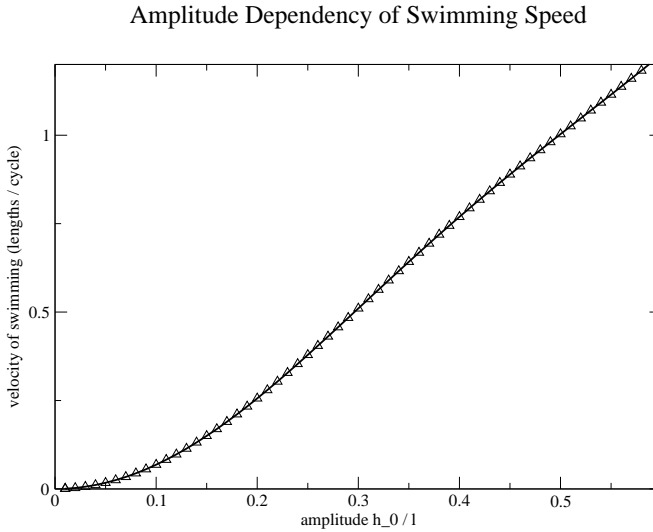


Figure 8.8.: Velocity versus amplitude for the case of an oscillating constraint close to the optimum for the speed ($Sp = 4$).

From these results it is clear that the amplitude of the drive for which the small deviation approximation breaks down depends on the value of Sp , being greater for smaller Sperm Numbers. At the optimal value for the speed, $Sp = 4$, the approximation holds for maximum transverse displacements of up to 20% of the tail length, which is well beyond the point one would expect the assumptions to be valid. However, for values of Sp much higher than 4 the value for the threshold is much lower. As an example, for an actin filament of $50\mu m$, driven at 1 cycle/second at an amplitude of 25% of its length, I estimated a speed of about $1.7\mu m/sec$ with the small deviation model, whereas the simulation predicts a reduction of this value by a factor $1/4$. I should point out that a length of $50\mu m$ is long for an actin filament but typical of a flagellum.

In the case of external driving in the form of a torque applied at one end, I have only considered large amplitude motion. Specifically, the pre-factor B was adjusted to produce a maximum angle at the driven end of 60° . This clearly violates the small angle approximation of Wiggins and Goldstein [113] but is more consistent with the head deflections found in practice for swimming organisms. In Fig. 8.9 I plot the efficiency and the mean velocity as functions of Sp . Once again, the two curves agree qualitatively with those found analytically by Wiggins and Goldstein in that there is a peak speed and efficiency. The locations of the peaks are at slightly different values of Sp and, because the small angle approximation is violated, not quantitatively predicted by Eq. (8.8).

I should add here a few comments. Notably, the peak efficiency of less than 1% seems very low. However, this depends strongly on the amplitude of the motion. Going above the 60° limit that was imposed so far for the torque, or to driving

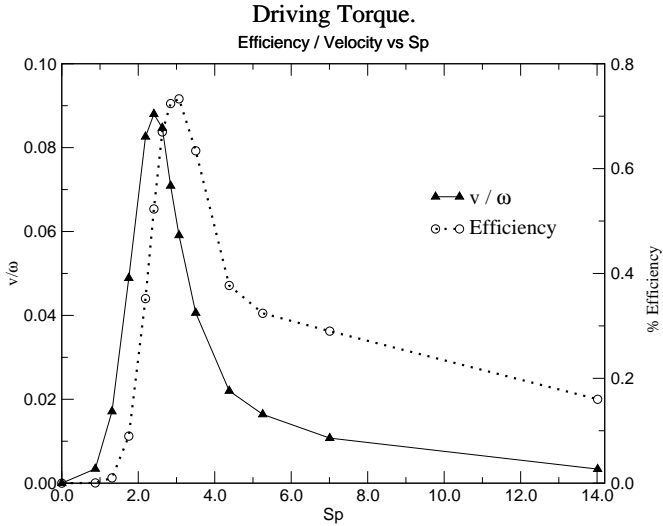


Figure 8.9.: Velocity / efficiency versus Sp for the case of driving torque.

amplitudes of greater than half the length of the filament, it is possible to reach values of 2% before the motion becomes unstable (in the sense that the steady state oscillatory motion is replaced by a tumbling motion during which the swimmer performs repeated complete rotations). This is similar to the efficiency typical for both the helical screw mechanism used by bacteria and sperm motion [115]. Thus, the one-armed swimmer operating at peak efficiency is a plausible and not especially inefficient entity. Note also that the efficiency (which is dimensionless), as well as the swimming speed, decays to zero rather than reaching a plateau value. This means that in absolute terms the one-armed swimmer can carry on with increasing speed by increasing its wiggling frequency but only at the price of decreasing efficiency.

8.4. Rotating Constraint

Up to now I have presented applications of the model to motions that, by physical means, were planar. However, there is no extra conceptual, nor computational cost in applying the model to a fully three dimensional motion. As a demonstration of this, I will describe in this section the results for a third kind of active drive realized through a constraint which makes the tangent vector precess along the axis of the filament (for us the $\hat{\mathbf{x}}$ direction) with angular velocity ω at a certain fixed angle. That is, $\partial_t \hat{\mathbf{t}} = \hat{\omega} \times \hat{\mathbf{t}}$, where $\hat{\omega} = \omega \hat{\mathbf{x}}$, and the parameter $a = \hat{\mathbf{t}} \cdot \hat{\mathbf{x}}$ is fixed to constrain the amplitude of the rotation. With these definitions it is possible to define the sperm number as in the previous sections. This active drive resembles the one that operates for the bacterial flagellar motor [94, 93, 126], where a rigid

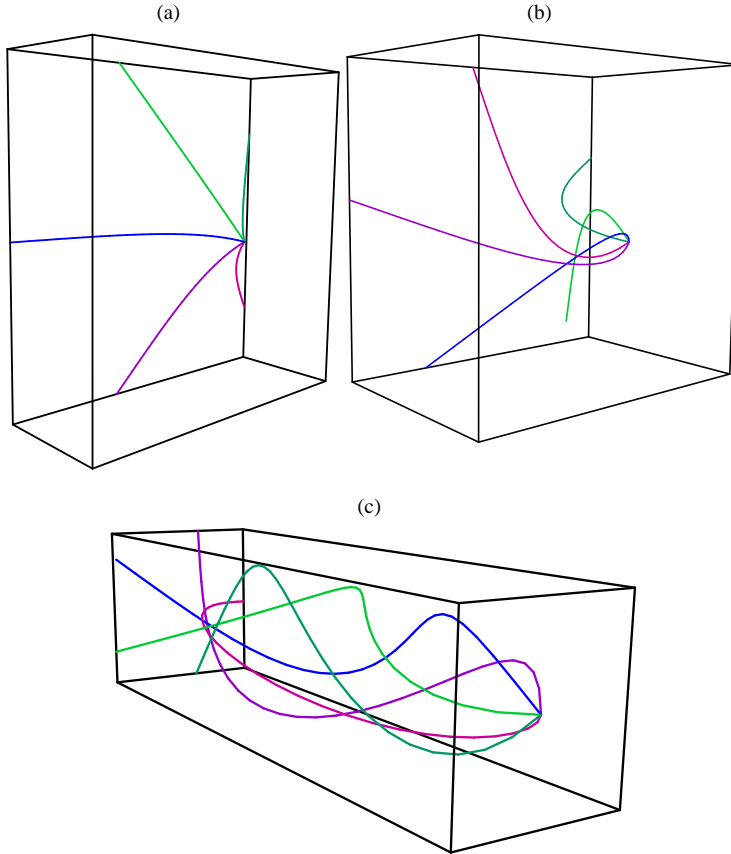


Figure 8.10.: Waveforms of the filament configurations for different values of Sp under a rotating constraint. The three dimensional configurations are plotted for five equally spaced time points during one cycle of rotation. (a) $Sp= 1.27$. The filament precesses as a rigid rod (b) $Sp= 2$. A small chirality begins to form, which breaks the symmetry of the motion. (c) $Sp= 5$. The filament looks like a helical propeller.

8. Dynamics of a Driven Semiflexible Polymer at Low Reynolds Number

tilted component (the “hook”) acts as a universal joint. However, it must be noted that a bacterial flagellar filament is an intrinsically chiral object, as opposed to our semiflexible appendage.

On the other hand, the first fact that emerges from the simulation, is that the rotating one armed swimmer will, for certain values of the parameters, assume a chiral configuration due to the hydrodynamic forces. At fixed amplitude a , this fact is again purely dependent on the value of the sperm number, as illustrated in Fig. 8.10. For small sperm numbers, the filament will rotate as a rigid rod, while for intermediate ones it will assume a helical shape, with the same handedness as the direction of rotation. Along with the breaking of chiral symmetry, comes breaking of time reversal symmetry. In these conditions the scallop theorem is again not applicable and the filament swims[92]. Interestingly, since the configuration is always right-handed for clockwise rotations and left-handed for counterclockwise ones, the direction of swimming is unchanged by the direction of turning, and the filament always swims towards its tail end, in a “backwards” fashion. For forward propulsion (the one relevant for bacteria), a filamentous propeller with handedness opposite to the direction of rotation is needed.

As in the previous cases, it is possible to measure speed and efficiency of the rotating one armed swimmer as a function of sperm number (Fig. 8.11). The rotating drive appears to be comparatively less efficient than the wiggling in generating motion, although it remains within the same range.

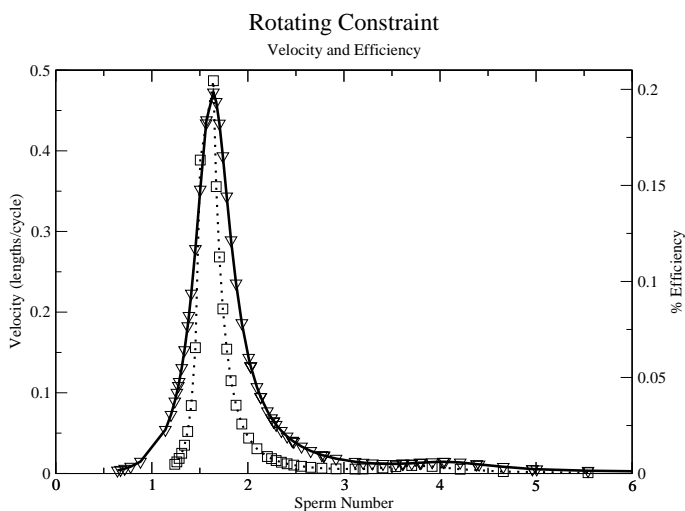


Figure 8.11.: Velocity (solid line) and efficiency (dotted line) versus Sp for a drive generated by a rotating constraint.

8.5. Conclusions

I have described a fully three dimensional simulation method that can be used to study the motion of driven elastic filaments in a low Reynolds number flow. Here, the hydrodynamic friction is treated quite simply, consistent with comparing with analytically tractable theories. I showed that, within this approximation, the picture suggested by Wiggins and Goldstein for the linear regime of small angular deviations from the straight position is essentially correct. The simulation results for the motion of the filament, show good agreement with their analytical calculations. There is an optimal balance between bending forces and viscous forces that leads to a maximum propulsive speed and efficiency. However, with respect to the swimming speed the results suggest that their analysis is incomplete. Instead, I could use their model to compute an expression for the average swimming velocity that is physically more plausible and agrees with the simulation results.

For large amplitude motion, I showed that the dependence of the swimming speed on both sperm number and amplitude was significantly modified relative to the small amplitude case. Further, I suggested that this is due to the fact that in a highly distorted filament the wave travels along a notably different path than it does for small amplitude motion. However, a quantitative understanding of this effect is still lacking. Nonetheless, the general picture derived from the linear theory, of an optimal compromise between the bending required to break time reversibility and excessive damping suppressing motion along the filament, remains valid. The most significant consequence is that there is a point beyond which increasing the wiggling frequency leads to a drop in efficiency. The small amplitude theory, on the other hand, predicts that the efficiency remains constant (which I also found to be the case in this limit).

For large amplitudes of oscillation, one-armed swimming is, speed and efficiency-wise, a plausible strategy a microorganism might use to get around. It is also a sight simpler than the helical screw mechanism used by most bacteria. This requires a rotary joint [94]. Nonetheless, while standing open to correction, I have not been able to identify a single organism that actually adopts this strategy. Perhaps the most interesting question surrounding the one armed swimmer is thus: why doesn't it exist? Based on the results, I can suggest two hypotheses. First, localized bending of the tail requires implausibly high energy densities. Second, the existence of an evolutionary barrier. It is useless trying to swim with a short, or slow moving, tail (in evolutionary terms one would expect that a primitive appendage would have both these properties). Note that at small Sp (that is, low frequency and/or a short appendage) there is nothing to be gained in terms of motility. For example, this is not the case for the traveling wave mechanism, used by spermatozoa, which gives a *maximum* swimming speed and efficiency at low sperm numbers. The helical screw mechanism, commonly used by bacteria, is not directly comparable to these results, because it is based on an intrinsically chiral appendage. Moreover, being approximately rigid, the helical screw operates at constant efficiency within a range of viscosities, and the swimming speed depends mainly on its geometrical features [127].

On the other hand, this last propulsion method can be compared with our toy model having a rotating torque applied to a semiflexible filament. Besides confirming that the simulation operates on a fully three dimensional problem, the results can be used for some simple considerations of biological relevance. As a matter of fact, the simulation confirms the basic statement, established by the scallop theorem, that to invert the direction of motion, a hypothetical bacterium could in principle reverse the chirality of its flagellum, instead of the rotation direction of the flagellar motor. Doing both would have no effect, as the results of inversion of handedness and rotation cancel each other. This is exactly what happens to the helical semiflexible filament, which has to adapt its chiral configuration to the direction of rotation of the drive. An imaginary bacterium with such a semi-flexible flagellum would only be allowed to swim backwards.

Regarding experimental studies of in vitro motility using imposed wiggling, one main problem so far is that the force involved has been too small to be detectable with an optical trapping experiment [125]. This limitation could be resolved simply by time, as it is reasonable to expect that the resolution of experiments will improve. On the other hand, by means of the model one could try to find the region of the parameter space where this force is expected to be the highest, and try to design an “optimal experiment” where the motility could actually be quantified.

Finally, more complete calculation of the hydrodynamic effects would without any doubt be instructive. In particular, the friction coefficients are not, as assumed so far, independent of distance along the filament. As we will see in the next chapter, at the expense of a little more computational complexity, such effects can be incorporated into the model in a straightforward manner.

8.A. Unequal Friction Coefficients as a Condition for Motility

It is possible to show that there can be no movement if the viscous drag coefficients are equal. Most conveniently, we work with the discrete model. Since the discrete model produces the continuum result in the limit that the number of beads N goes to infinity, there is no loss of generality (so long as the answer does not depend on N). The equation of motion for the center of mass is

$$m \frac{d\bar{\mathbf{v}}}{dt} = \sum_{i=1}^N \mathbf{f}_i, \quad (8.9)$$

where $\bar{\mathbf{v}} = \frac{1}{N} \sum_{i=1}^N \mathbf{v}_i$ is the center of mass velocity, m is the total mass. The total force \mathbf{f}_i on each bead consists of a bending force \mathbf{f}_{iB} a tension force \mathbf{f}_{iT} an hydrodynamic force \mathbf{f}_{iH} and an “external” force \mathbf{f}_{iX} which accounts for the external drive. We know that by definition

$$\sum_{i=1}^N \mathbf{f}_{iB} = \sum_{i=1}^N \mathbf{f}_{iT} = 0$$

Now, the external periodic force is applied only at one extremity, so that $\sum_{i=1}^n \mathbf{f}_{iX} = \mathbf{f}_1(t)$, and Eq. (8.9) can be written as

$$m \frac{d\bar{\mathbf{v}}}{dt} = \sum_{i=1}^N \mathbf{f}_{iH} + \mathbf{f}_1(t).$$

Integrating on a cycle we get

$$m \Delta \bar{\mathbf{v}}_{\text{cycle}} = \int_{\text{cycle}} dt \sum_{i=1}^N \mathbf{f}_{iH}.$$

The hydrodynamic force on bead i is written in the form $\mathbf{f}_{iH} = -\xi_{i\parallel} \mathbf{v}_{i\parallel} - \xi_{i\perp} \bar{\mathbf{v}}_{i\perp}$ (with $\xi_{iX} = \xi_X/N$). Thus, the effective drag on one particle depends on the local configuration of the filament shape.

If the two friction coefficients are the same $\xi_{i\parallel} = \xi_{i\perp} = \xi_i$ then

$$m \Delta \bar{\mathbf{v}}_{\text{cycle}} = \xi \int_{\text{cycle}} dt \bar{\mathbf{v}}, \quad (8.10)$$

which necessarily leads to zero (or decaying to zero) global velocity. On the other hand, if the two drags are different, the right hand side integral in Eq. (8.10) can be written as

$$\int_{\text{cycle}} dt \xi_*(t) \bar{\mathbf{v}}(t),$$

where ξ_* is an effective drag which depends on time through the configuration of the filament. This integral in general gives a number once, in the spirit of resistive force theory, the configuration is plugged in, and swimming is not, therefore, precluded.

8.B. Analytical Computation of the Mean Swimming Velocity in the the Small Angular Deviation Approximation

Here I outline the procedure adopted to calculate analytically the average of the swimming speed using the small deviation approximation. This calculation largely follows the methodology used in [108] on a different model.

We can define the time average of the swimming speed (projected along its only nonzero component along the $\hat{\mathbf{x}}$ direction) as

$$\langle v \rangle = \lim_{t \rightarrow \infty} \frac{1}{t} \int_0^L dt \partial_t \mathbf{r} \cdot \hat{\mathbf{x}}.$$

The expression for $\partial_t \mathbf{r}$ can be obtained from Eq. (8.2) in terms of the local angle ψ as

$$\partial_t \mathbf{r} = \frac{1}{\xi_{\perp}} \mathbf{n} (-k \partial_s^3 \psi + \tau \partial_s \psi) + \frac{1}{\xi_{\parallel}} \mathbf{t} (k \partial_s^2 \psi \partial_s \psi + \partial_s \tau).$$

8. Dynamics of a Driven Semiflexible Polymer at Low Reynolds Number

Fixing a reference frame one can consider the “comoving” frame with respect to the filament, and expand ψ and τ , together with the absolute displacements h and u , and the swimming speed $\langle v \rangle$ as in Eq. (8.5). Following this reasoning we can rewrite in vector notation the formula above for $s = 0$ as

$$\begin{aligned} & (\varepsilon \langle v_1 \rangle + \varepsilon^2 \langle v_2 \rangle, 0) + \partial_t (\varepsilon u_1(0) + \varepsilon^2 u_2(0), \varepsilon h_1(0) + \varepsilon^2 h_2(0)) = \\ & = \left[\frac{1}{\xi_{\perp}} \varepsilon^2 k \psi_1 \partial_s^3 \psi_1 + \frac{1}{\xi_{\parallel}} (k \varepsilon^2 \partial_s^2 \psi_1 \partial_s \psi_1 + \varepsilon^2 \partial_s \tau_2) \right]_0 \hat{\mathbf{x}} + \left[\frac{1}{\xi_{\perp}} (-k \varepsilon \partial_s^3 \psi_1) \right]_0 \hat{\mathbf{y}}, \end{aligned} \quad (8.11)$$

where we stop the expansion to second order in ε .

Expressing the equality for the different powers of ε one gets $\langle v_1 \rangle = 0$ and

$$\langle v_2 \rangle + \partial_t u_2(0) = -\psi_1(0) \partial_t h_1(0) + \frac{1}{\xi_{\parallel}} (k \partial_s \psi_1(0) \partial_s^2 \psi_1(0) + \partial_s \tau_2(0)),$$

where $\tau_2(0)$ can be obtained integrating Eq. (8.11). Finally, taking into account the boundary conditions for h , u and τ one gets to the expression

$$\langle v_2 \rangle + \partial_t u_2(0) = \frac{\xi_{\perp} - \xi_{\parallel}}{\xi_{\parallel} L} \int_0^L ds \partial_s h_1 \partial_t h_1 + \frac{1}{L} \int_0^L ds \int_0^s ds' \frac{1}{2} \partial_t (\partial_s h_1)^2.$$

For any cyclic motion, the terms which involve time derivatives (the second term on the left and the second term on the right) integrate to zero resulting in the expression of Camalet and Julicher. Using the analytical solution of Eq. (8.6) then gives Eq. (8.8).

9. A Method to Include Oseen-level Hydrodynamic Interaction

9.1. Introduction

The purpose of this chapter is to extend the slender body model of a filament, presented in chapter 8, to include a simple and computationally economical description of the hydrodynamic interactions induced by the presence of a low Reynolds number fluid. The first question to ask is whether it is necessary to describe a filament with hydrodynamic interactions in the context of filament motility. The work described so far neglects them. Nevertheless, we have seen that such a simple description is consistent with tractable theoretical models, and captures the essential behavior observed in experiments. Considering this, we can anticipate, for the case of the one-armed swimmer, a mere validation of the results of the previous model, and therefore that a refined description of hydrodynamics is inessential. I will show that this is indeed the case. In fact, this point of view can be revolved, and the results for the one-armed swimmer can be used to validate the simulation technique that includes the hydrodynamic interactions.

On the other hand, we will see that unusual behavior, resulting from the non-uniformity of the drags along the filament, emerges in a much simpler nonequilibrium problem, that of sedimentation, or driving from a constant force field. I will show that, besides reproducing the correct behavior in the limit of stiff filaments, the extended model shows instabilities that are completely missed by the slender body model, as they depend on the interplay between the non-local action of the fluid velocity field and the elastic degrees of freedom of the body. These results are possibly testable experimentally.

Furthermore, there are interesting problems connected to the biology of swimming micro-organisms that cannot be treated without hydrodynamic interactions. These problems concern the dynamics of many filaments and are related to many body swimming. As a matter of fact, if the previous chapter was inspired by the hydrodynamics of swimming of a single microorganism with a semiflexible tail, we can say the present one establishes the basis to approach the problem of the cooperation and coordination of many of these hypothetical organisms or tails. This is very relevant in a biological context, for example in ciliary movement. Cilia

move in a cyclic beat composed of two phases: the *power stroke* – which actively propels the fluid – and the *recovery stroke*, which is passive. A ciliated cell generally has a field of hundreds of cilia which beat in a coordinated manner, setting up wave-like time dependent patterns. This phenomenon is referred to as *metachronism*. To describe the hydrodynamics of the highly correlated movements of many cilia, observed in the phenomenon of metachronism, hydrodynamic interactions are necessary [128, 122].

The viscous forces are in general complex to implement. They are dependent on the instantaneous shape of the filament and are also time dependent [129]. They can in principle be incorporated keeping the time dependence, using numerical solutions of the Navier-Stokes equations of different kinds [130], or mesoscopic models such as the lattice Boltzmann techniques [131]. A cheaper alternative is to incorporate only the “steady state” level, for example using Stokesian dynamics [132]. I will make this choice in what follows, introducing a model inspired by Stokesian dynamics, adapted to the description of a semiflexible, inextensible filament. Section 9.2 contains a description of the algorithm and how hydrodynamic interactions are represented in it. The sedimentation of a filament is treated in sections 9.3 and 9.4. Finally, in section 9.5, I will discuss the problem of the one-armed swimmer.

9.2. Description of the Method

As in the previous model, I discretize the time evolution equation and the filament itself. Each discretization point can be regarded as a small sphere, a “bead”, from the hydrodynamic point of view, interacting with all the others through the velocity field propagated by the fluid.

The discrete evolution equations for the i -th discretization point are obtained using the velocity Verlet algorithm [133]. They are

$$\begin{aligned} \mathbf{r}_i(t + \Delta t) &= \mathbf{r}_i(t) + \mathbf{v}_i(t)\Delta t + \frac{\Delta t^2}{2m_i}\mathbf{F}_i(t) \\ \mathbf{v}_i(t + \Delta t) &= \mathbf{v}_i(t) + \frac{\Delta t}{2m_i}(\mathbf{F}_i(t) + \mathbf{F}_i(t + \Delta t)). \end{aligned} \quad (9.1)$$

The previous expression contains the three familiar contributions for the forces. Namely, the bending forces, \mathbf{F}_{iB} , the constraint forces \mathbf{F}_{iC} and the friction forces \mathbf{F}_{if} . The bending forces \mathbf{F}_{iB} are computed as described in Ch. 8 (page 92). The constraint forces can be decomposed in passive (the inextensibility constraint) and active (the drive): $\mathbf{F}_{iC} = \mathbf{F}_{iC_p} + \mathbf{F}_{iC_a}$. Finally, the last contribution, \mathbf{F}_{if} , has to include the hydrodynamic interactions, and will contain all the changes of this model with respect to the previous one.

To describe hydrodynamic interactions, we need to know the force exerted by the fluid on the bead. This last quantity can in principle be computed knowing the the velocities of the beads, and solving Stokes equation with the boundary conditions imposed by this configuration. This would require using a numerical solver

for Stokes equation on all space, and having to represent explicit solid-fluid interfaces, thereby increasing the computational cost.

To avoid this complication, one can use a mobility matrix, or the fundamental solution of Stokes equation [134], as is done in Stokesian dynamics [132]. Let us assume that $\mathbf{F}_{jB} + \mathbf{F}_{jC}$, for $j \neq i$, are the forces exerted on the fluid by all the other beads, then the fluid velocity created at position $\mathbf{r}_i(t)$, which we can call the ‘‘hydrodynamic velocity’’, $\mathbf{v}_i^H(t)$, of bead i , is computed in the Oseen approximation, through the expression [84, 132]

$$\mathbf{v}_i^H(t) = \gamma_0^{-1} \frac{3}{4} \frac{a}{b} \left\{ \sum_{j \neq i} \frac{\mathbf{1} + \hat{\mathbf{r}}_{ij}(t) \hat{\mathbf{r}}_{ij}(t)}{r_{ij}(t)/b} \right\} \cdot [\mathbf{F}_{jB}(t) + \mathbf{F}_{jC}(t)], \quad (9.2)$$

where $\gamma_0 = 6\pi\eta$, a is the hydrodynamic radius of a bead and b the distance of two subsequent beads. Better approximations, such as the Rotne-Prager mobility matrix [135], can be used instead of the Oseen tensor without affecting the model.

In this model I assume the hydrodynamic force to be a dissipative force due to the difference between the velocity of bead i at a given time and its hydrodynamic velocity. In other words, the friction force on the discretization point i is implemented as

$$\mathbf{F}_{if} = -\gamma_0(\mathbf{v}_i - \mathbf{v}_i^H). \quad (9.3)$$

This can be seen as a sort of dissipative constraint that will impose self-consistency between the solution of the equation of motion of the body (defined by the set of beads) and the solution of Stokes equation for the fluid (in the Oseen approximation). It can be easily checked that the friction coefficient multiplying \mathbf{v}_i^H in this expression cancel out with its inverse entering Eq. (9.2). This indicates that the value of γ_0 is only relevant for the term $\gamma_0 \mathbf{v}_i$ of Eq. 9.3. This term corresponds to the dissipative force which sets the relaxation time scale (the scale on which the inertia of the body is important, see below).

We can rewrite the evolution equation for the velocity spelling out the velocity dependence of the friction force,

$$\begin{aligned} \mathbf{v}_i(t + \Delta t) &= \mathbf{v}_i(t) + \frac{\Delta t}{2m_i} [\mathbf{F}_{iB}(t) + \mathbf{F}_{iC}(t) + \mathbf{F}_{iB}(t + \Delta t) + \mathbf{F}_{iC}(t + \Delta t)] \\ &+ \gamma_0 \frac{\Delta t}{2m_i} [\mathbf{v}_i^H(t) + \mathbf{v}_i^H(t + \Delta t) - \mathbf{v}_i(t)] \\ &- \gamma_0 \frac{\Delta t}{2m_i} \mathbf{v}_i(t + \Delta t). \end{aligned} \quad (9.4)$$

From a practical point of view, it is worth decomposing the velocity update in two steps, before and after the forces and velocities of the subsequent iteration (time $t + \Delta t$) are computed. Starting from the explicit expression

$$\begin{aligned} \mathbf{v}_i(t + \Delta t) &= \frac{1}{1 + \gamma_0 \frac{\Delta t}{2m_i}} \left\{ \mathbf{v}_i(t) + \frac{\Delta t}{2m_i} (\mathbf{F}_{iB}(t) + \mathbf{F}_{iC}(t) + \mathbf{F}_{iB}(t + \Delta t) + \mathbf{F}_{iC}(t + \Delta t)) \right. \\ &+ \left. \gamma_0 [\mathbf{v}_i^H(t) + \mathbf{v}_i^H(t + \Delta t) - \mathbf{v}_i(t)] \right\}, \end{aligned} \quad (9.5)$$

9. A Method to Include Oseen-level Hydrodynamic Interaction

we can separate in the right hand side the contributions relative to time t from those relative to time $t + \Delta t$.

The velocity update is carried by calling in two instances the Verlet subroutine. In the first sub-step the positions are updated, and the velocities are modified according to the contributions relative to time t .

$$\begin{aligned} \mathbf{v}_i^*(t + \Delta t) &= \frac{1}{1 + \gamma_0 \frac{\Delta t}{2m_i}} \left[\mathbf{v}_i(t) + \frac{\Delta t}{2m_i} (\mathbf{F}_{iB}(t) + \mathbf{F}_{iC}(t) + \gamma_0 [\mathbf{v}_i^H(t) - \mathbf{v}_i(t)]) \right] \\ \mathbf{r}_i(t + \Delta t) &= \mathbf{r}_i(t) + \mathbf{v}_i(t)\Delta t + \frac{\Delta t^2}{2m_i} [\mathbf{F}_{iB}(t) + \mathbf{F}_{iC}(t) - \gamma_0(\mathbf{v}_i(t) - \mathbf{v}_i^H(t))] . \end{aligned} \quad (9.6)$$

In the second sub-step, after the positions and the forces have been updated, the velocities of a complete time step are computed by adding the missing contribution to the force, relative to the new configuration (time $t + \Delta t$)

$$\mathbf{v}_i(t + \Delta t) = \mathbf{v}_i^*(t + \Delta t) + \frac{\Delta t}{2m_i} \frac{1}{1 + \gamma_0 \frac{\Delta t}{2m_i}} [\mathbf{F}_{iB}(t + \Delta t) + \mathbf{F}_{iC}(t + \Delta t) + \gamma_0 \mathbf{v}_i^H(t + \Delta t)] . \quad (9.7)$$

One can see that the mass of the beads enters these equations in two forms. On the one hand it appears as part of the ratio γ_0/m_i . Dimensionally, this is an inverse time, corresponding to the frequency at which the particle loses its acceleration. To reproduce the correct behavior of a low Reynolds number fluid, this relaxation time should be very small, which suggests choosing a large friction coefficient and/or a small mass. On the other hand, the mass also enters dividing the conservative forces, as it usually happens in any molecular dynamics model. Suppose for example $\mathbf{v}^H = 0$ and $\gamma_0 = 0$. In this case the ratio between the typical magnitude of the force and the mass sets a characteristic time in which the velocity changes. The mass will then determine the magnitude of the time steps. However, I have to note that within the framework of the method it is not sensible to look at inertial effects because the inertia of the fluid is neglected by postulating Stokes equation in the first place. All that is relevant for us is that the mass is sufficiently small to make the dynamics independent from it.

To summarize and clarify, I would like to spell out how the algorithm is actually implemented.

1. Compute $\{\mathbf{v}_i^H\}$.
2. Verlet update (time t).
3. Constrain positions.
4. Compute active forces.
5. Compute bending forces.
6. Compute tension.
7. Compute $\{\mathbf{v}_i^H\}$.

8. Verlet update (time $t + \Delta t$).

Steps 3,4 and 5 are identical to the slender body hydrodynamics model of chapter 8. The other steps have been discussed in this section, with the exception of the tension calculation (step 6), which is carried out in an identical way as the other two constraints [119]. This tension did not need to be computed explicitly in the previous model, but becomes necessary now, as it enters the expression for the hydrodynamic velocity. I was not concerned with the performance of this implementation of the constraints with respect to other possibilities, rather I used the minimal extension of the previous model that would function in the new framework. For a thorough discussion on different techniques of implementing constraints in similar simulations the interested reader can look at [136].

9.3. Measurement of the Friction Coefficients and Sedimentation

In order to make a connection with the model without hydrodynamic interaction and to validate the technique on known analytical results, it is useful to compute the longitudinal and transverse friction coefficients of the filament. These quantities are not external parameters as previously, but have to be computed dynamically. Moreover, the force exerted by the fluid on the object is not spatially constant, but can vary along the filament's length, and, acting on the elastic degrees of freedom, modify the shape of the object.

To measure the parallel and perpendicular drag coefficients, one can simply apply a uniform force field longitudinally or transversely to the filament, and evaluate the resulting velocity of the body, as it would be done in an experiment. For sufficiently stiff filaments, we can compare the results with a discretized calculation on the “shish kebab” model (see reference [84], p. 292) of a rigid rod based on the Oseen tensor. In this model the rod is represented as a set of n beads with hydrodynamic radius equal to one-half their distance ($b = 2a$). This kind of calculation gives, in the infinite n limit the approximation

$$\begin{aligned}\xi_{\parallel} &= \frac{2\pi\eta L}{\log(L/b)} \\ \xi_{\perp} &= 2\xi_{\parallel}\end{aligned}$$

for the values of the drag coefficients (whose exact expression is not known, but can be obtained with better precision comparing with the solution of Stokes equation for a high aspect ratio ellipsoid in a force field [134]). If the number of discretization points n for the shish kebab rod and the model filament are the same, this calculation is in agreement with the simulated results to the last significant digit. This test proves that the hydrodynamic description of the model has the same qualitative validity of the “shish kebab” description of a rigid rod. Quantitatively, it contains the same degree of approximation.

Let us consider now a transverse force field. Having in mind the shish kebab picture of the filament makes it easy to realize that the hydrodynamic velocity is

9. A Method to Include Oseen-level Hydrodynamic Interaction

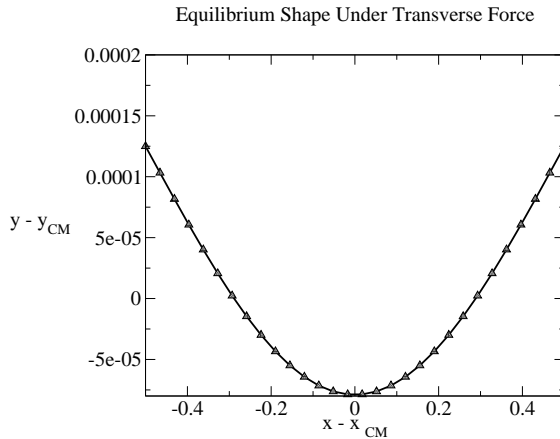


Figure 9.1.: Equilibrium shape of a filament dragged transversely towards negative y in a constant force field for a value $bFL/k = 7.2 \cdot 10^{-3}$.

not constant along the contour of the body. In particular, the beads closer to the edges will feel a higher resistance, because they have a lower number of neighbors to cooperate with. This non-constant force exerted by the fluid, coupled with the filament’s bending elasticity, will result in a non flat steady-state shape during sedimentation, which in turn may affect the value of the transverse drag. The configuration cannot violate the left-right mirror symmetry of the problem. If γ_0 (and therefore the viscosity of the fluid) is fixed, the correct nondimensional parameter, which we can call the “sedimentation number”, or Sed , to associate with this deflection effect is

$$Sed := bFL/k ,$$

where F is the magnitude of the external force field. As can be expected (Fig. 9.1), the typical shape of a filament has the shape of a U, with the ends pointing away from the force field. For small bFL/k , the U shape corresponds to excitations of the first elastic mode.

For $Sed \sim 90$ a more surprising transition occurs, in which a long-standing metastable mode higher than the first is excited (Fig. 9.2). The shape of this configuration is still mirror symmetric as expected, but assumes the profile of a double well, or a W. The W shaped configuration is stable for very long times, but becomes unstable when one of the two wells is lower and left-right symmetry is broken. After this destabilization event, the filament absorbs one of the minima and assumes again a U shape with inward extremities. If the filament starts from an (even very slightly) tilted configuration with respect to the direction orthogonal to the driving field, the symmetry between the two minima of the W is broken from the beginning, and an asymmetric W shape rapidly decays into a U.

The transitions between different regimes are associated with changes in the values of the measured transverse drag. Fig. 9.3 shows the ratio of the drags as a

9.3. Measurement of the Friction Coefficients and Sedimentation

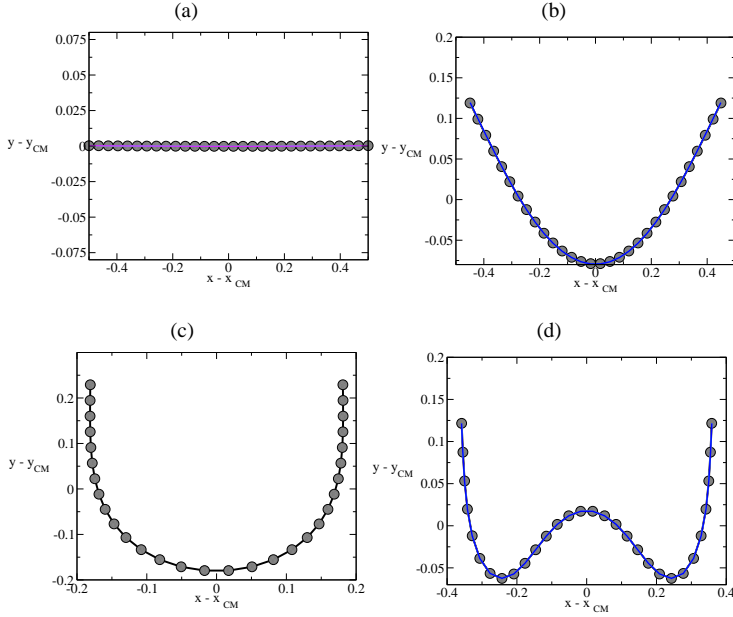


Figure 9.2.: Steady-state shapes of a filament sedimenting in a transverse field. (a) U shape for $Sed \sim 10^{-2}$; on the scale of observation the filament appears flat, but its shape can be rescaled to overlap exactly with the one shown in (b). (b) U shape for $Sed \sim 1$. (c) U shape for $Sed \sim 10$. (d) Metastable W shape, $Sed \sim 100$.

function of bFL/k . For small values of this number the filament is rigid, and the model reproduces the value of the shish-kebab rod model with the same discretization. As the value of Sed increases, the U shape becomes more and more circular, minimizing the transverse drag ξ_{\perp} up to the point that it becomes almost equal to the longitudinal one. On the other hand, the long-lived metastable state found is characterized by a much higher drag than the U, and a sudden jump is visible as a function of Sed . When this W state becomes unstable and transforms into a U, its transverse drag drops radically once more.

Finally, one can analyze the variations in the amplitude of the shape at the steady-state, defined as the vertical distance of the filament extremities from the center of mass (Fig. 9.4). This quantity increases linearly with Sed in the small drive regime. For larger drives, the U shape assumes vertical or converging tangents at the extremities, and the amplitude saturates, because of the constraints imposed by the inextensibility condition. Lastly, the transition to a long-lived metastable W shaped state generates a decrease in the amplitude because of the larger number of folds.

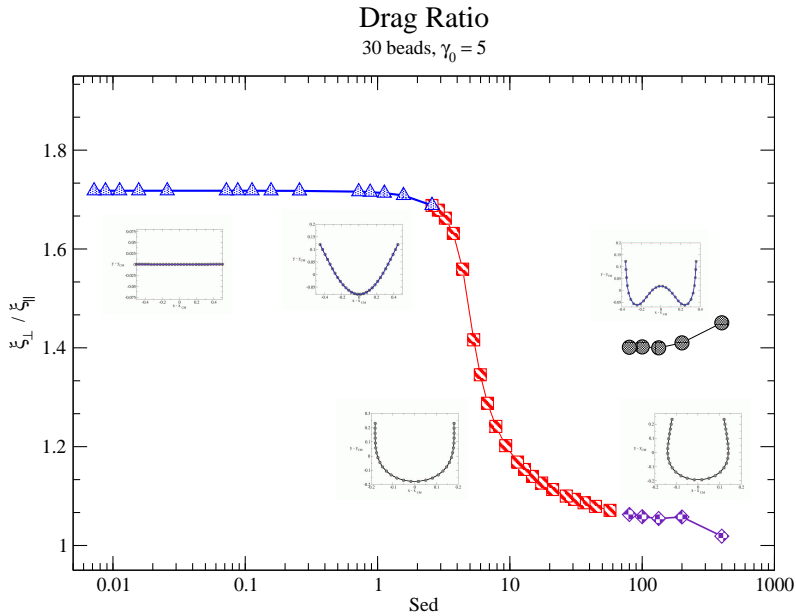


Figure 9.3.: Ratio of the drags as a function of the sedimentation number. The graphs next to the curve indicate the typical shape of the filament in that regime. For small drives, or large stiffness, the ratio of the drags agrees with that predicted by the shish-kebab model with the same number of beads. For $Sed \sim 90$, it starts dropping dramatically, as the filament is more free to modify its shape in order to minimize the fluid resistance. In presence of the long-standing metastable state, another branch appears, with a higher ratio for the drags.

9.4. Sedimentation of an Oblique Filament

As I have shown, the main difference between the model including hydrodynamic interactions and the previous one is whether or not the fluid is able to excite the elastic degrees of freedom of the uniformly driven object. In particular, in the slender-body picture with fixed drags, a filament falling in a constant force field will not bend. This is not true in presence of hydrodynamic interactions. One interesting problem concerns a filament in a straight configuration under a driving field at a fixed angle α with the filament orientation, or, in other words, a filament sedimenting under an angle with the gravitational field. Perhaps surprisingly, I find that, due to the elastic instability triggered by the inhomogeneous viscous force, the filament always reorients itself in a direction orthogonal to the driving field. This is illustrated in Fig. 9.5. It is not trivial to understand how a torque can be generated by the combined action of these inhomogeneous forces and the deformation of the filament. I will give an argument on how this is possible. Let us consider the

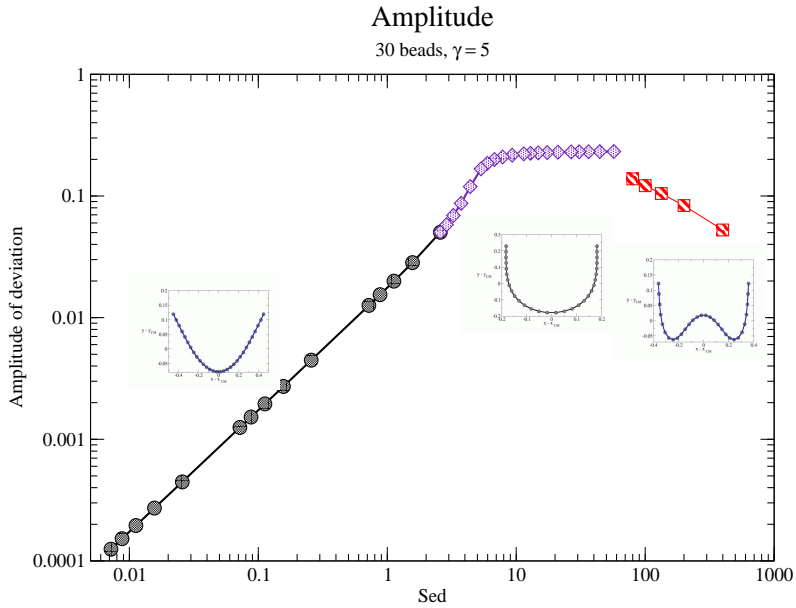


Figure 9.4.: Amplitude of the steady-state configuration as a function of Sed. The amplitude is defined as the maximal distance between two points of the filament along the vertical direction. It scales linearly with Sed in the low drive regime, then it saturates for higher drives, when the inextensibility constraint starts playing a role. Finally, it drops for the W configuration, because of the higher number of folds.

9. A Method to Include Oseen-level Hydrodynamic Interaction

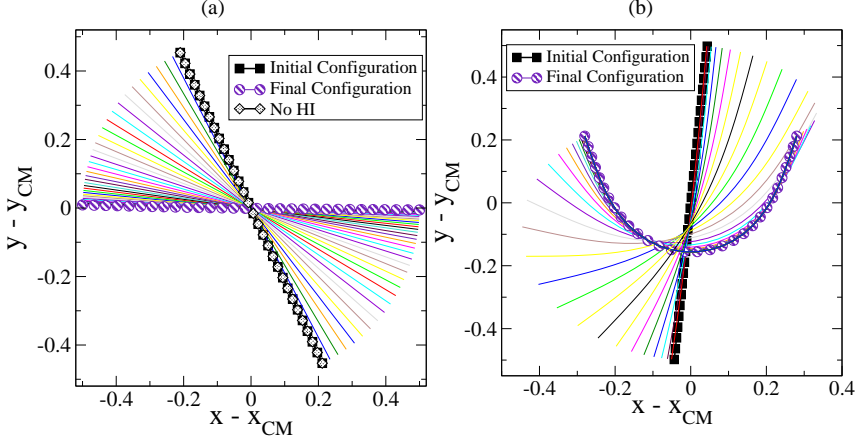


Figure 9.5.: Sedimentation of tilted filaments. The configurations are plotted using the center-of-mass as the origin. (a) Comparison of the results in the models with and without hydrodynamic interactions, for a filament, both with $\xi_{\parallel} = 0.31$, $\xi_{\perp} = 0.18$, and $Sed = 2$, starting from an angle of 25° from the direction of the field (the negative y direction in the graph). Reorientation is absent without hydrodynamic interactions (\diamond). Even for relatively rigid filaments such as this one, the bending instability is sufficient to generate a torque on sufficiently large time scales. The initial configuration (\square) evolves in one exactly perpendicular to the field (\circ). (b) Reorientation of a filament with $Sed = 8$ starting from an initial angle of 5° from the field direction. The elastic instability is visible in this case.

filament as an array of beads, neglecting bending and constraint forces. These beads are equally spaced on a line, and each one is subject to an external force \mathbf{f} under an angle α with this line. The transverse velocity felt by the i -th bead of this linear array is

$$\mathbf{v}_i \cdot \hat{\mathbf{n}} = f \sin(\alpha) \left(\frac{1}{\gamma} + C \sum_{j \neq i} \frac{1}{r_{ij}} \right),$$

where $C = \frac{3}{4} \frac{a}{b} \gamma_0^{-1}$. Due to the sum term in the above expression, this velocity is not homogeneous, but depends on i , being lower at the extremities, where the number of neighbors is lower. However, it is mirror symmetric with respect to the center of mass, so it will not cause any rotation. On the other hand, if the beads are not on a line transverse to the driving field, this left-right symmetry in the configuration can be broken, causing an imbalance in the velocities as well, and thereby making it possible to generate rotations of the whole body. Although I find this reorientation for any filament stiffness, the rotation time increases for stiffer filaments, so that the process requires longer and longer simulation times to be observable.

To analyze the scaling of the relaxation time with the parameters, let us consider a filament starting from a fixed angle and driven in the negative y direction. The reorientation process can be quantified by the value of $\langle \theta \rangle (t)$, where θ is the angle formed by the filament with the horizontal direction, and $\langle \dots \rangle$ is the spatial average along the filament. This quantity decays as an exponential in time, as can be seen in Fig. 9.6(a).

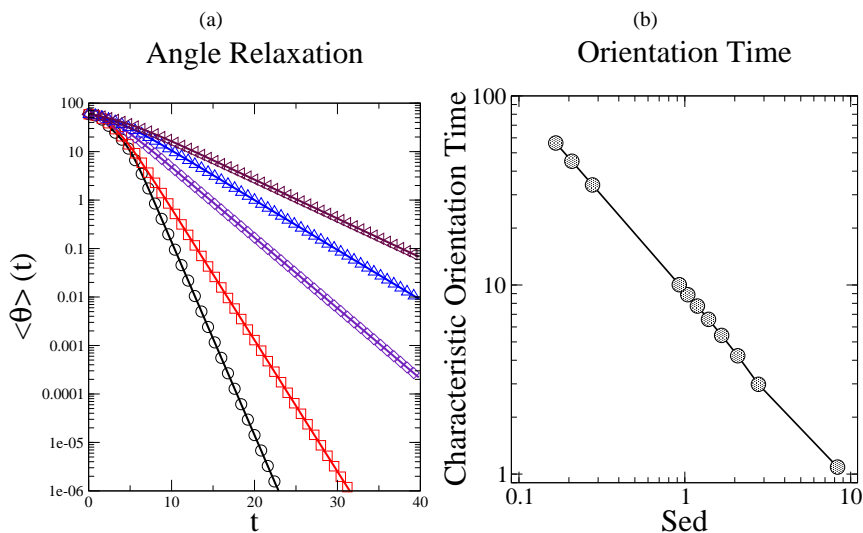


Figure 9.6.: (a) Exponential time decay of the average angle $\langle \theta \rangle (t)$ with respect to the driving field in a few instances, for different values of Sed (linear-log scale). (b) Characteristic orientation time as a function of Sed , plotted in a log-log scale.

The characteristic time scale of the reorientation extracted from these exponentials can be plotted as a function of Sed , yielding a power law with exponent -1 (Fig. 9.6b). Once again, as it can be anticipated, changing the stiffness or the strength of the driving field has an equivalent effect. For larger drives (or smaller stiffness) the relaxation time decreases because the elastic modes are more easily excited.

One may wonder whether this unexpected behavior in uniform driving fields would be observable experimentally, in particular with mesoscopic bio-filaments. If we estimate the value of Sed for a microtubule of, for example, $30 \mu m$ falling under gravity, we get the discouraging order of magnitude of 10^{-6} , for which neither bending nor reorientation in reasonable time-scales are visible. To see any effect, one would need to put the polymer in an ultra-centrifuge, where Sed can increase to the order of 1. In this case, the predicted deflection is about 1% and according to the model the filament would reorient itself transverse to the field on a length scale of thirty times its own length, approximately 1 mm. In these considerations, the main

restriction on the value of S_{ed} is imposed by the microtubule's extremely small mass. This is valid for all the other biofilaments. On the other hand, the magnitude of the total force needed to get a value of S_{ed} in the range 1 – 10 is not exceedingly high, in the region of 1 pN. This can be easily obtained, for example, with an optical trap, which, however, exerts a point force. Forces of the same range can be generated by exerting on the microtubule (in its usual pH 6.8 buffer) a uniform electric field of strength 10 V/cm [137]. In this case there would be an interesting competition between the hydrodynamic rotation towards the transverse direction and the small (on the order of kT for these field strengths) longitudinal aligning potential energy due to the permanent electric dipole moment of the filaments [138, 137].

9.5. One-Armed Swimmer with Hydrodynamic Interaction

A second test of the new model is assessing whether it is able to reproduce the data of the one-armed swimmer. It is. This is not trivial because the longitudinal and transverse drags are not external parameters anymore, but are determined by the dynamics, and so is the sperm number. This is illustrated in figures 9.7, for the example of the swimming speed. Once again, the entire dynamics of the filament is specified, at fixed driving amplitude, by the sperm number, which this time has to be computed using the *measured* transverse drag, evaluated as described in section 9.3.

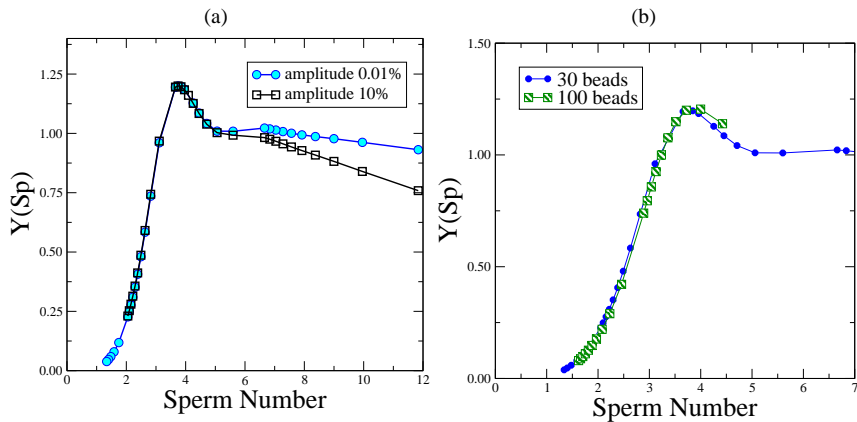


Figure 9.7.: Velocity of the wiggled one-armed swimmer as a function of sperm number in presence of hydrodynamic interactions. (a) Comparison of different amplitudes of the drive (b) Comparison of different discretizations.

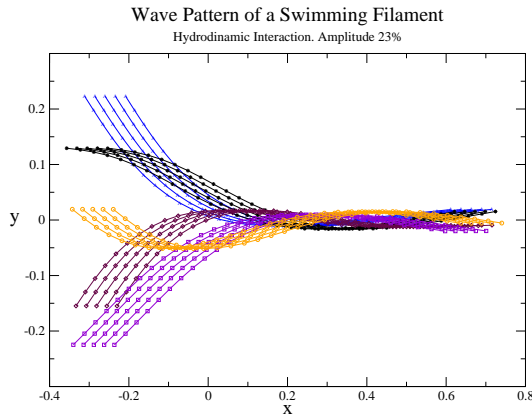


Figure 9.8.: Wave patterns of a wiggled filament at $Sp = 9$, plotted over 5 subsequent cycles. The swimming motion is visible.

On the other hand, I have not been able to identify any qualitative behavior that is not already described by the slender body model with fixed drags. This is another confirmation of the strength of this simple model, which, already in the small amplitude limit that is treatable analytically, is able to make many correct predictions. From the quantitative point of view, this agreement is essentially confirmed. However, the one-armed swimmer with hydrodynamic interactions appears to be a few percent slower, and less efficient than the non-interacting one.

9.6. Conclusions

I have discussed a method to include hydrodynamic interactions in the model for a semiflexible filament in a low Reynolds number fluid described in Ch. 8. This is a new method, designed to be computationally cheap and to avoid the complication of having to deal with explicit representations of the body-fluid surface. The method was validated by measuring the drag coefficients and comparing with known results both for discrete models and in the continuum limit. A second confirmation of its validity comes from the application to the problem of the wiggled one-armed swimmer.

More interestingly, I have shown that novel nontrivial behavior emerges in applying the model to the problem of filament sedimentation. A first effect is the presence of elastic instabilities, translated in changes of the value of the transverse drag for a filament in a transverse driving field. Surprisingly, modes higher than the first can be excited in the limit of large drives. The second notable result is the prediction that, because of the interplay between elastic instabilities and hydrodynamic interactions, a sedimenting filament tends to rotate place itself orthogonal to the driving field. Some of these results can possibly be tested experimentally on biological polymers such as microtubules, by using fast centrifugation or electric

9. *A Method to Include Oseen-level Hydrodynamic Interaction*

field as a drive.

However, this chapter is merely a prelude to what the model can be used for. The main advantage of the simulation method described here is its small computational cost, that allows to explore larger time scales and problems involving many filaments. In fact, there is an astonishing number of open problems that can be tackled with the method. This is valid both in soft condensed matter (collective sedimentation, behavior under shear, interplay of thermal fluctuations and hydrodynamic interactions) and, more interestingly for the author, in biology (coordination and cooperativity of ciliary and flagellar movement in eukaryotes).

10. Discussion and Open Problems

The scope of this chapter is to draw some comprehensive conclusion on this second part of the thesis. Once again, I will try to focus more on the issues where a physical point of view helps formulating statements with some biological relevance. In this view, the first fact worth mentioning is undoubtedly the reason for the nonexistence of one-armed swimmers in the biological world. For large amplitude motion (the only one biologically relevant), I have shown that this swimming strategy does not have major disadvantages with respect to the competition. However, it seems that no known microorganism on this planet adopts it. A possible explanation of this is the necessity of exceedingly high forces localized at the junction of the tail. Another possibility is based on the functional dependence of speed and efficiency on filament length, stiffness and driving frequency. The model shows that trying to swim with a short, or slow moving tail is never advantageous. On the other hand, we can imagine that a primitive appendage would be short, and would not have any reason to be particularly fast moving. This hypothetical barrier would be absent for both the traveling wave mechanism used by spermatozoa, and the helical screw mechanism used by most bacteria.

Experimental realizations of the one-armed swimmer *in vitro*, applying wiggling forces or periodic torque (or even rotary drive) using optical tweezers are definitely within reach. The main complication is that spurious fluid flow in the sample must be absent. To date, the only experimental attempt [125] using a wiggled actin microfilament, failed to measure the propulsive force, because of limits in the resolution, and was used as a measure of the stiffness of the filament (for which more reliable methods are available [66]). Being able to measure force and efficiency in such a setup would allow a direct comparison with the theoretical model. Furthermore the model I presented could help finding “optimal” parameters in designing an experiment of this kind.

Another issue with some biological implications is the dynamics of a semiflexible filament jointed with a rotary drive. The results show that because the filament has to change the handedness of its configuration with the direction of rotation of the drive, it can never invert the direction of propulsion. An imaginary bacterium with such a semi-flexible flagellum would suffer of this intrinsic limitation in its steering capabilities. These facts are perfectly compatible with the scallop theorem.

Let us now discuss the role of the hydrodynamic description of the swimming filament. It appears that for the single filament one-armed swimmer a simple local description of the hydrodynamics is sufficient to capture the behavior of the object.

10. Discussion and Open Problems

Introducing hydrodynamic interactions leads only to minor quantitative changes. In fact, the main limitation of the analytical treatment of Wiggins and Goldstein lies in the hypothesis of small amplitude deviations in the shape, necessary to linearize the equation of motion. On the other hand, the simple but computationally efficient nonlocal model of hydrodynamics introduced in chapter 9 can be useful for different problems in the context of biologically inspired motility. For example, the single filament experiments mentioned above are always performed in presence of walls, which can only be taken into account using a nonlocal description of hydrodynamics. More importantly, cooperativity is widely exploited by swimming, or flow-generating cells [94, 139].

A final point regards the possibility of extending the model using more complex, biologically realistic drives. In this thesis, by studying simplified drives such as the one-armed swimmer, I have treated motility as a separate problem from internal force generation in flagella. The main reason for this is that the last problem, despite of the wealth of investigation over the past thirty years is still somewhat open. One of the problems is to generate models that describe both the generation of the wave-patterns and the feedback mechanisms necessary for synchronization. In my opinion, the most effective attempt in doing this is the relatively recent work of Camalet and Julicher [108, 140], which is based on the small deviation approximation for the passive dynamics of the filament, combined with a model for the activity of internal microtubules and motors in a simplified geometry. The model predicts that motion can be generated by a Hopf-bifurcation mechanisms that drives the system to an oscillatory state, which can also give rise to a feedback to external perturbations. Such a description could be implemented in the simulation and explored in conditions of large amplitude motion, and presence of hydrodynamic interactions for a single or many filaments.

Bibliography

- [1] A. Desai and T.J. Mitchison. Microtubule polymerization dynamics. *Annu Rev Cell Dev Biol*, 13:83–117, 1997.
- [2] F. Gittes, B. Mickey, J. Nettleton, and J. Howard. Flexural rigidity of microtubules and actin filaments measured from thermal fluctuations in shape. *J Cell Biol*, 120(4):923–34, 1993.
- [3] E. Nogales, S.G. Wolf, and K.H. Downing. Structure of the alpha beta tubulin dimer by electron crystallography. *Nature*, 391(6663):199–203, 1998.
- [4] A.M. Dogterom. PhD thesis, Université Paris Sud, Centre d’Orsay, 1994.
- [5] M. Dogterom and S. Leibler. Physical aspects of the growth and regulation of microtubule structures. *PHYSICAL REVIEW LETTERS*, 70(9):1347–1350, 1993.
- [6] B. Alberts, A. Johnson, J. Lewis, M. Raff, K. Roberts, and P. Walter. *Molecular Biology of the Cell*. Garland, NY, 2002.
- [7] M.A. Sleight. *Cilia and Flagella*. Academic, London, 1974.
- [8] M. Kirschner and T. Mitchison. Beyond self-assembly: from microtubules to morphogenesis. *Cell*, 45(3):329–42, 1986.
- [9] U. Mayer and G. Jurgens. Microtubule cytoskeleton: a track record. *Curr Opin Plant Biol*, 5(6):494–501, 2002.
- [10] T. Hashimoto. Dynamics and regulation of plant interphase microtubules: a comparative view. *Curr Opin Plant Biol*, 6(6):568–76, 2003.
- [11] T. Hashimoto and D. Inze. Cell biology. How unique is the plant cell? *Curr Opin Plant Biol*, 6(6):517–9, 2003.
- [12] R.J. Cyr and B.A. Palevitz. Organization of cortical microtubules in plant cells. *Curr Opin Cell Biol*, 7(1):65–71, 1995.
- [13] J. Azimzadeh, J. Traas, and M. Pastuglia. Molecular aspects of microtubule dynamics in plants. *Curr Opin Plant Biol*, 4(6):513–9, 2001.
- [14] G.O. Wasteneys. Microtubule organization in the green kingdom: chaos or self-order? *J Cell Sci*, 115(Pt 7):1345–54, 2002.

Bibliography

- [15] C. Lloyd and J. Chan. Helical microtubule arrays and spiral growth. *Plant Cell*, 14(10):2319–24, 2002.
- [16] B. Gunning and M. Sammut. Rearrangements of Microtubules Involved in Establishing Cell Division Planes Start Immediately after DNA Synthesis and Are Completed just before Mitosis. *Plant Cell*, 2(12):1273–1282, 1990.
- [17] Y. Mineyuki. The preprophase band of microtubules: its function as a cytokinetic apparatus in higher plants. microscopy of tubulin and microtubule arrays in plant cells. II. *Int. Rev. Cytol.*, 187:1–49, 1999.
- [18] J.W. Vos, B. Sieberer, A.C. Timmers, and A.M. Emons. Microtubule dynamics during preprophase band formation and the role of endoplasmic microtubules during root hair elongation. *Cell Biol Int*, 27(3):295, 2003.
- [19] P. Dhonukshe and T.W. Gadella, Jr. Alteration of microtubule dynamic instability during preprophase band formation revealed by yellow fluorescent protein-CLIP170 microtubule plus-end labeling. *Plant Cell*, 15(3):597–611, 2003.
- [20] A.M.C. Emons and B.M. Mulder. The making of the architecture of the plant cell wall: how cells exploit geometry. *Proc Natl Acad Sci U S A*, 95(12):7215–9, 1998.
- [21] B. Kost and N.H. Chua. The plant cytoskeleton: vacuoles and cell walls make the difference. *Cell*, 108(1):9–12, 2002.
- [22] B. Kost, J. Mathur, and N.H. Chua. Cytoskeleton in plant development. *Curr Opin Plant Biol*, 2(6):462–70, 1999.
- [23] A.S.N. Reddy. Molecular motors and their functions in plants. *Int Rev Cyt*, 204:97 – 178, 2001.
- [24] C. Lloyd and J. Chan. Microtubules and the shape of plants to come. *Nat Rev Mol Cell Biol*, 5(1):13–22, 2004.
- [25] C.L. Wymer, D.D. Fisher, R.C. Moore, and R.J. Cyr. Elucidating the mechanism of cortical microtubule reorientation in plant cells. *Cell Motil Cytoskeleton*, 35(2):162–73, 1996.
- [26] A.R. Hardham and B.E.S Gunning. The Length and Disposition of Cortical Microtubules in Plant Cells Fixed in Glutaraldehyde-Osmium Tetroxide. *Planta*, 134:201–203, 1977.
- [27] A.R. Hardham and B.E. Gunning. Structure of cortical microtubule arrays in plant cells. *J Cell Biol*, 77(1):14–34, 1978.
- [28] J. Chan, C.G. Jensen, L.C. Jensen, M. Bush, and C.W. Lloyd. The 65-kDa carrot microtubule-associated protein forms regularly arranged filamentous cross-bridges between microtubules. *Proc Natl Acad Sci U S A*, 96(26):14931–6, 1999.

- [29] K. Sugimoto, R.E. Williamson, and G.O. Wasteneys. New techniques enable comparative analysis of microtubule orientation, wall texture, and growth rate in intact roots of *Arabidopsis*. *Plant Physiol*, 124(4):1493–506, 2000.
- [30] B. Wiesler, Q.Y. Wang, and P. Nick. The stability of cortical microtubules depends on their orientation. *Plant J*, 32(6):1023–32, 2002.
- [31] A.T. Whittington, O. Vugrek, K.J. Wei, N.G. Hasenbein, K. Sugimoto, M.C. Rashbrooke, and G.O. Wasteneys. MOR1 is essential for organizing cortical microtubules in plants. *Nature*, 411(6837):610–3, 2001.
- [32] R. Himmelspach, C.L. Wymer, C.W. Lloyd, and P. Nick. Gravity-induced reorientation of cortical microtubules observed in vivo. *Plant J*, 18(4):449–53, 1999.
- [33] S.L. Shaw, R. Kamyar, and D.W. Ehrhardt. Sustained microtubule treadmill in *Arabidopsis* cortical arrays. *Science*, 300(5626):1715–8, 2003.
- [34] J. Vos, M. Dogterom, and A.M.C. Emons. Microtubules become more dynamic but not shorter during preprophase band formation: A possible search-and-capture mechanism for microtubule translocation. *Cell Motility and the Cytoskeleton*, 57(4):246–258, 2004.
- [35] T. Asada, R. Kuriyama, and H. Shibaoka. TKRP125, a kinesin-related protein involved in the centrosome-independent organization of the cytokinetic apparatus in tobacco BY-2 cells. *J Cell Sci*, 110 (Pt 2):179–89, 1997.
- [36] F.J. Nedelec, T. Surrey, A.C. Maggs, and S. Leibler. Self-organization of microtubules and motors. *Nature*, 389(6648):305–8, 1997.
- [37] T.E. Holy, M. Dogterom, B. Yurke, and S. Leibler. Assembly and positioning of microtubule asters in microfabricated chambers. *Proc Natl Acad Sci U S A*, 94(12):6228–31, 1997.
- [38] C. Faivre-Moskalenko and M. Dogterom. Dynamics of microtubule asters in microfabricated chambers: the role of catastrophes. *Proc Natl Acad Sci U S A*, 99(26):16788–93, 2002.
- [39] C. W. Lloyd. Toward a Dynamic Helical Model for the Influence of Microtubules on Wall Patterns in Plants. *Int Rev Cyt*, 86:1–52, 1984.
- [40] C. W. Lloyd and R.W. Seagull. A new spring for plant cell biology: microtubules as dynamic helices. *TIBS*, 10:476–478, 1985.
- [41] G. Nicolis and I. Prigogine. *Self-organization in nonequilibrium systems : from dissipative structures to order through fluctuations*. Wiley, New York, 1977.
- [42] M.C. Cross and P.C. Hohenberg. Pattern-Formation Outside of Equilibrium. *Reviews of Modern Physics*, 65(3):851 – 1112, JUL 1993.

Bibliography

- [43] H. Meinhardt and P.A. de Boer. Pattern formation in *Escherichia coli*: a model for the pole-to-pole oscillations of Min proteins and the localization of the division site. *Proc Natl Acad Sci U S A*, 98(25):14202–7, 2001.
- [44] K. Kruse. A dynamic model for determining the middle of *Escherichia coli*. *Biophys J*, 82(2):618–27, 2002.
- [45] M. Howard and A.D. Rutenberg. Pattern formation inside bacteria: fluctuations due to the low copy number of proteins. *Phys Rev Lett*, 90(12):128102, 2003.
- [46] P.I. Bastiaens. Reaction networks in signalling and morphogenesis, Research Report. Technical report, EMBL, Heidelberg, 2002.
- [47] C. Papaseit, N. Pochon, and J. Tabony. Microtubule self-organization is gravity-dependent. *Proc Natl Acad Sci U S A*, 97(15):8364–8, 2000.
- [48] N. Glade, J. Demongeot, and J. Tabony. Comparison of reaction-diffusion simulations with experiment in self-organised microtubule solutions. *C R Biol*, 325(4):283–94, 2002.
- [49] S. Portet, J.A. Tuszyński, J.M. Dixon, and M.V. Sataric. Models of spatial and orientational self-organization of microtubules under the influence of gravitational fields. *Phys Rev E Stat Nonlin Soft Matter Phys*, 68(2 Pt 1):021903, 2003.
- [50] D. Frenkel and R. Eppenga. Evidence for algebraic orientational order in a two-dimensional hard-core nematic. *Phys Rev A*, 31:1776–1787, 1985.
- [51] M.A. Bates and D. Frenkel. Phase behavior of two-dimensional hard rod fluids. *J Chem Phys*, 112(22):10034 – 10041, JUN 8 2000.
- [52] J.M. Kosterlitz and D.J. Thouless. Ordering, metastability and phase transitions in two-dimensional systems. *Journal of Physics C*, 6(7):1181–1203, 1973.
- [53] J. Dzubiella, M. Schmidt, and H. Lowen. Topological defects in nematic droplets of hard spherocylinders. *Phys Rev E*, 62(4):5081 – 5091, OCT 2000.
- [54] P. vanderSchoot. Nematics of linear assemblies in two dimensions. *J Chem Phys*, 106(6):2355 – 2359, FEB 8 1997.
- [55] M. Schmidt and H. Lowen. Freezing between two and three dimensions. *Phys Rev Lett*, 76(24):4552 – 4555, JUN 10 1996.
- [56] A. Poniewierski. Ordering of Hard Needles at a Hard-wall. *Phys Rev E*, 47(5):3396 – 3403, MAY 1993.
- [57] R. van Roij, M. Dijkstra, and R. Evans. Orientational wetting and capillary nematization of hard-rod fluids. *Europhys Lett*, 49(3):350 – 356, FEB 2000.

- [58] Z.Y. Chen and S.M. Cui. Orientational Wetting Layer of Semiflexible Polymers Near a Hard-wall. *Phys Rev E*, 52(4):3876 – 3880, OCT 1995.
- [59] R. van Roij, M. Dijkstra, and R. Evans. Interfaces, wetting, and capillary nematization of a hard-rod fluid: Theory for the Zwanzig model. *J Chem Phys*, 113(17):7689 – 7701, NOV 1 2000.
- [60] L. Harnau and S. Dietrich. Wetting and capillary nematization of binary hard-platelet and hard-rod fluids. *Phys Rev E*, 66(5):art. no. – 051702, NOV 2002.
- [61] M. Dijkstra, R. van Roij, and R. Evans. Wetting and capillary nematization of a hard-rod fluid: A simulation study. *Phys Rev E*, 6305(5):art. no. – 051703, MAY 2001.
- [62] C. Tanase. PhD thesis, AMOLF, Amsterdam, 2004.
- [63] <http://rsb.info.nih.gov/ij/>.
- [64] www.vtk.org.
- [65] <http://vegemite.chem.nott.ac.uk/xmakemol/>.
- [66] M.E. Janson. *Force Generation by Growing Microtubules*. PhD thesis, AMOLF, Amsterdam, 2002.
- [67] D.K. Fygenson, E. Braun, and A. Libchaber. Phase diagram of microtubules. *Phys Rev E*, 50(2):1579–1588, 1994.
- [68] C. Barroso, J. Chan, V. Allan, J. Doonan, P. Hussey, and C. Lloyd. Two kinesin-related proteins associated with the cold-stable cytoskeleton of carrot cells: characterization of a novel kinesin, DcKRP120-2. *Plant J*, 24(6):859–68, 2000.
- [69] J.C. Gardiner, J.D. Harper, N.D. Weerakoon, D.A. Collings, S. Ritchie, S. Gilroy, R.J. Cyr, and J. Marc. A 90-kD phospholipase D from tobacco binds to microtubules and the plasma membrane. *Plant Cell*, 13(9):2143–58, 2001.
- [70] F. Nedelec, T. Surrey, and E. Karsenti. Self-organisation and forces in the microtubule cytoskeleton. *Curr Opin Cell Biol*, 15(1):118–24, 2003.
- [71] D.G. Oppenheimer, M.A. Pollock, J. Vacik, D.B. Szymanski, B. Ericson, K. Feldmann, and M.D. Marks. Essential role of a kinesin-like protein in Arabidopsis trichome morphogenesis. *Proc Natl Acad Sci U S A*, 94(12):6261–6, 1997.
- [72] D.G. Oppenheimer. Genetics of plant cell shape. *Curr Opin Plant Biol*, 1(6):520–4, 1998.

Bibliography

- [73] R. Zhong, D.H. Burk, W.H. Morrison, 3rd, and Z.H. Ye. A kinesin-like protein is essential for oriented deposition of cellulose microfibrils and cell wall strength. *Plant Cell*, 14(12):3101–17, 2002.
- [74] F. Gibbons. PhD thesis, CIRCS, Boston, 1998.
- [75] F. Nedelec. Computer simulations reveal motor properties generating stable antiparallel microtubule interactions. *J Cell Biol*, 158(6):1005–15, 2002.
- [76] B. Bassetti, M.C. Lagomarsino, and P. Jona. A model for the self-organization of microtubules driven by molecular motors. *Eur Phys Jour B*, 15(3):483 – 492, JUN 2000.
- [77] T.B. Liverpool and M.C. Marchetti. Instabilities of isotropic solutions of active polar filaments. *Phys Rev Lett*, 90(13), APR 4 2003.
- [78] K. Kruse and F. Julicher. Actively contracting bundles of polar filaments. *Phys Rev Lett*, 85(8):1778 – 1781, AUG 21 2000.
- [79] K. Kruse and F. Julicher. Self-organization and mechanical properties of active filament bundles. *Phys Rev E*, 67(5), MAY 2003.
- [80] K. Kruse, A. Zumdieck, and F. Julicher. Continuum theory of contractile fibres. *Europhys Lett*, 64(5):716–722, 2003.
- [81] H.Y. Lee and M. Kardar. Macroscopic equations for pattern formation in mixtures of microtubules and molecular motors. *Phys Rev E Stat Nonlin Soft Matter Phys*, 64(5 Pt 2):056113, 2001.
- [82] J. Kim, Y Park, B. Kahng, and H.Y. Lee. Self-Organized Patterns in Mixtures of Microtubules and Motor Proteins. *Journal of the Korean Physical Society*, 42:162–166, 2003.
- [83] L.D. Landau. *Phys. Z. Sowjetunion*, 11:26, 1937.
- [84] M. Doi and S.F. Edwards. *The Theory of Polymer Dynamics*. Clarendon Press, Oxford, 1986.
- [85] J. Chan, G.M. Calder, J.H. Doonan, and C.W. Lloyd. EB1 reveals mobile microtubule nucleation sites in Arabidopsis. *Nat Cell Biol*, 5(11):967–71, 2003.
- [86] G.W. Tian, D. Smith, S. Gluck, and T.I. Baskin. Higher plant cortical microtubule array analyzed in vitro in the presence of the cell wall. *Cell Motil Cytoskeleton*, 57(1):26–36, 2004.
- [87] T. Surrey, M.B. Elowitz, P.E. Wolf, F. Yang, F. Nedelec, K. Shokat, and S. Leibler. Chromophore-assisted light inactivation and self-organization of microtubules and motors. *Proc Natl Acad Sci U S A*, 95(8):4293–8, 1998.

- [88] M. Dogterom, A.C. Maggs, and S. Leibler. Diffusion and formation of microtubule asters: physical processes versus biochemical regulation. *Proc Natl Acad Sci U S A*, 92(15):6683–8, 1995.
- [89] C.A. Hale, H. Meinhardt, and P.A. de Boer. Dynamic localization cycle of the cell division regulator MinE in *Escherichia coli*. *EMBO J*, 20(7):1563–72, 2001.
- [90] J.E. Johnson, L.L. Lackner, and P.A. de Boer. Targeting of (D)MinC/MinD and (D)MinC/DicB complexes to septal rings in *Escherichia coli* suggests a multistep mechanism for MinC-mediated destruction of nascent FtsZ rings. *J Bacteriol*, 184(11):2951–62, 2002.
- [91] A.R. Reynolds, C. Tischer, P.J. Verveer, O. Rocks, and P.I. Bastiaens. EGFR activation coupled to inhibition of tyrosine phosphatases causes lateral signal propagation. *Nat Cell Biol*, 5(5):447–53, 2003.
- [92] E.M. Purcell. Life at Low Reynolds Numbers. *Am J Phys*, 45:3–11, 1977.
- [93] H.C. Berg and R.A. Anderson. Bacteria swim by rotating their flagellar filaments. *Nature*, 245(5425):380–2, 1973.
- [94] D. Bray. *Cell Movements*. Garland, New York, 1992.
- [95] J. Gray and G. Hancock. *J Exp Biol.*, 32:802, 1955.
- [96] K.E. Machin. Wave Propagation Along Flagella. *J Exp Biol*, 35:796–806, 1958.
- [97] K.E. Machin. *Proc Roy Soc Lond*, B158:88, 1963.
- [98] C.J. Brokaw. Computer simulation of flagellar movement. I. Demonstration of stable bend propagation and bend initiation by the sliding filament model. *Biophys J*, 12(5):564–86, 1972.
- [99] C.J. Brokaw. Cross-bridge behavior in a sliding filament model for flagella. *Soc Gen Physiol Ser*, 30:165–79, 1975.
- [100] M. Hines and J.J. Blum. Bend propagation in flagella. I. Derivation of equations of motion and their simulation. *Biophys J*, 23(1):41–57, 1978.
- [101] M. Hines and J.J. Blum. Bend propagation in flagella. II. Incorporation of dynein cross-bridge kinetics into the equations of motion. *Biophys J*, 25(3):421–41, 1979.
- [102] M. Hines and J.J. Blum. Three-dimensional mechanics of eukaryotic flagella. *Biophys J*, 41(1):67–79, 1983.
- [103] M. Hines and J.J. Blum. On the contribution of moment-bearing links to bending and twisting in a three-dimensional sliding filament model. *Biophys J*, 46(5):559–65, 1984.

Bibliography

- [104] M. Murase and H. Shimizu. A model of flagellar movement based on cooperative dynamics of dynein-tubulin cross-bridges. *J Theor Biol*, 119(4):409–33, 1986.
- [105] M. Murase, M. Hines, and J.J. Blum. Properties of an excitable dynein model for bend propagation in cilia and flagella. *J Theor Biol*, 139(3):413–30, 1989.
- [106] M. Murase. Excitable dynein model with multiple active sites for large-amplitude oscillations and bend propagation in flagella. *J Theor Biol*, 149(2):181–202, 1991.
- [107] S. Gueron, K. Levit-Gurevich, N. Liron, and J.J. Blum. Cilia internal mechanism and metachronal coordination as the result of hydrodynamical coupling. *Proc Natl Acad Sci U S A*, 94(12):6001–6, 1997.
- [108] S. Camalet and F. Julicher. Generic Aspects of Axonemal Beating. *New J Phys*, 2:24.1–24.23, 2000.
- [109] S. Gueron and K. Levit-Gurevich. A three-dimensional model for ciliary motion based on the internal 9+2 structure. *Proc R Soc Lond B Biol Sci*, 268(1467):599–607, 2001.
- [110] C.B. Lindemann. Geometric Clutch model version 3: the role of the inner and outer arm dyneins in the ciliary beat. *Cell Motil Cytoskeleton*, 52(4):242–54, 2002.
- [111] C.J. Brokaw. Computer simulation of flagellar movement VIII: coordination of dynein by local curvature control can generate helical bending waves. *Cell Motil Cytoskeleton*, 53(2):103–24, 2002.
- [112] D. Riveline, C.H. Wiggins, R.E. Goldstein, and A. Ott. Elastohydrodynamic study of actin filaments using fluorescence microscopy. *Phys Rev E*, 56(2):R1330 – R1333, AUG 1997.
- [113] C.H. Wiggins and R.E. Goldstein. Flexive and propulsive dynamics of elastica at low Reynolds number. *Phys Rev Lett*, 80(17):3879 – 3882, APR 27 1998.
- [114] J. Keller and S.J. Rubinow. Slender-body Theory for Slow Viscous Flow. *J Fluid Mech*, 75:705–714, 1976.
- [115] C.P. Lowe. A hybrid particle/continuum model for micro-organism motility. *Fut Gen Comp Sys*, 17(7):853 – 862, MAY 2001.
- [116] V. Ohm, A.F. Bakker, and C.P. Lowe. In *Proceedings of the Eighth School on Computing and Imaging*, 2002.
- [117] O. Kratky and G. Porod. *Rec Trav Chim Pays-Bas*, 68:1106:1118, 1949.

- [118] P.S. Doyle, E.S.G. Shaqfeh, and A.P. Gast. Dynamic simulation of freely draining flexible polymers in steady linear flows. *J Fluid Mech*, 334:251 – 291, MAR 10 1997.
- [119] C.P. Lowe and S.W. de Leeuw. Strategies for Constraint Dynamics. In A. Hoekstra and J.F.M. Tonino, editors, *Proceedings of the 5th annual conference of the Advanced School for Imaging and Computing*, pages 279–287, 1999.
- [120] F. Gittes and F. C. MacKintosh. Dynamic shear modulus of a semiflexible polymer network. *Phys Rev E*, 58:R1241–R1244, 1998.
- [121] R. Everaers, F. Jülicher, A. Ajdari, and A.C. Maggs. Dynamic Fluctuations of Semiflexible Filaments. *Phys Rev Lett*, 82:3717–3720, 1999.
- [122] S. Gueron and K. Levit-Gurevich. Energetic considerations of ciliary beating and the advantage of metachronal coordination. *Proc Natl Acad Sci U S A*, 96(22):12240 – 12245, OCT 26 1999.
- [123] E. Farge and A.C. Maggs. Dynamic scattering from semiflexible polymers. *Macromolecules*, 26(19):5041–5044, 1993.
- [124] R. Granek. From Semi-flexible Polymers to Membranes: Anomalous Diffusion and Reptation. *J. Phys. II France*, 7:1761, 1997.
- [125] C.H. Wiggins, D. Rivelino, A. Ott, and R.E. Goldstein. Trapping and wiggling: Elastohydrodynamics of driven microfilaments. *Biophys J*, 74(2):1043 – 1060, FEB 1998.
- [126] H.C. Berg and L. Turner. Movement of microorganisms in viscous environments. *Nature*, 278(5702):349–51, 1979.
- [127] E.M. Purcell. The efficiency of propulsion by a rotating flagellum. *Proc Natl Acad Sci U S A*, 94(21):11307–11, 1997.
- [128] M.A. Sleight. Coordination of the rhythm of beat in some ciliary systems. *Int Rev Cytol*, 25:31–54, 1969.
- [129] L. D. Landau and E. M. Lifshitz. *Fluid Mechanics*. Pergamon Press, 1959.
- [130] J. Connor and C. Brebbia. *Finite Element Techniques for Fluid Flow*. Newnes-Butterworths, 1976.
- [131] A.J.C. Ladd. Short-time motion of colloidal particles - numerical-simulation via a fluctuating lattice-boltzmann equation. *Phys Rev Lett*, 70(9):1339 – 1342, MAR 1 1993.
- [132] J. F. Brady and G. Bossis. The rheology of concentrated suspensions of spheres in simple shear flow by numerical simulation. *J. Fluid Mech*, 155:105–129, 1985.

Bibliography

- [133] D. Frenkel and B. Smit. *Understanding molecular simulation : from algorithms to applications*. Academic Press, San Diego, CA, 2002.
- [134] J. Happel and H. Brenner. *Low Reynolds Number Hydrodynamics with Special Applications to Particulate Media*. Martinus Nijhoff Publishers, Dordrecht, 1986.
- [135] J. Rotne and S Prager. Variational treatment of hydrodynamic interaction in polymers. *Journal-of-Chemical-Physics*, 50(11):4831–7, 1969.
- [136] R. Kutteh. Stokesian dynamics of nonspherical particles, chains, and aggregates. *J Chem Phys*, 119(17):9280 – 9294, NOV 1 2003.
- [137] R. Stracke, K.J. Bohm, L. Wollweber, J.A. Tuszyński, and E. Unger. Analysis of the migration behaviour of single microtubules in electric fields. *Biochem Biophys Res Commun*, 293(1):602–9, 2002.
- [138] P.M. Vassilev, R.T. Dronzine, M.P. Vassileva, and G.A. Georgiev. Parallel arrays of microtubules formed in electric and magnetic fields. *Biosci Rep*, 2(12):1025–9, 1982.
- [139] H. Moore, K. Dvorakova, N. Jenkins, and W. Breed. Exceptional sperm cooperation in the wood mouse. *Nature*, 418(6894):174–7, 2002.
- [140] S. Camalet. PhD thesis, Université Paris 6, 2001.

Samenvatting

Dit proefschrift beschrijft het onderzoek van mij (en anderen) aan twee verschillende biologische onderwerpen, benaderd vanuit een natuurkundig standpunt. Dit houdt in dat ik probeer biologische processen tot hun essentie te reduceren en het functioneren ervan op basis van natuurkundige principes te verklaren. Om de geldigheid van het theoretisch werk te verifiëren heb ik waar mogelijk gebruik gemaakt van *in vitro* experimenten.

Het onderwerp van mijn onderzoek zijn zogenaamde cytoskelet-filamenten. Deze filamenten komen voor in elke levende cel die behoort tot de klasse van de *eukaryoten*. Hieronder vallen uiteenlopende soorten zoals mensen, muggen, walvissen, gist en alle planten. Een uitzondering vormen de bacteriën; zij behoren tot de *prokaryoten*. In vergelijking met de eukaryoten zijn de cellen bij prokaryoten vaak kleiner en minder complex, zowel in hun organisatie als in de taken die ze uitvoeren. Het is precies de complexiteit van eukaryotische cellen die hen geschikt maakt om meercellige organismen te vormen.

De cytoskelet-filamenten in eukaryotische cellen zijn stevige uit eiwitten opgebouwde structuren die vele toepassingen hebben binnen de cel. Zo worden ze gebruikt als 'rails' waarlangs materialen in de cel worden getransporteerd en bepalen ze de structuur van de cel. De filamenten binnen de cel die bepalend zijn voor de structuur van de cel vormen tezamen de basis van het cytoskelet, zo genoemd naar analogie met het skelet in volledige organismen.

1. Het eerste deel van dit proefschrift beschrijft onderzoek aan celdeling dat is uitgevoerd als een onderdeel van een gezamenlijk project van de groepen 'bio-assembly and organisation' en 'theorie van biomoleculaire materie' op AMOLF, de plantencelbiologiegroep van de Universiteit Wageningen, de groep 'biologische fysica' van het MPI-PKS in Dresden en Marjolein Dijkstra, van de Universiteit Utrecht. Het begrip van dit celdelingsproces is een belangrijk onderwerp in de biologie, met vele fysische aspecten. Mijn onderzoek betreft het ontstaan van orde in de organisatie van *microtubuli*, de stevigste van alle filamenten in eukaryoten, in de tijd tussen celdelingen in plantencellen. Experimenten laten zien dat voorafgaand aan de celdeling deze microtubuli zich eerst ordenen in een laag van evenwijdige filamenten vlak onder het celmembraan, die zich vervolgens samentrekt tot een dunne band, de *pre-profaseband*.

De natuurkundige aanpak van dit probleem begint met radicale simplificaties van het systeem. Op theoretisch gebied houdt dit de constructie van simpele modellen in. Op experimenteel gebied betekent dit de constructie van een systeem dat

slechts bestaat uit een minimaal aantal componenten, los van de complexe biologische afhankelijkheden die een rol spelen in een levende cel - en dus in biologische experimenten. Zo hebben we microtubuli laten groeien in 'micro-kamers' met dezelfde afmetingen als een plantencel en met behulp van een microscoop gekeken naar de configuratie van de filamenten in de kamers.

Binnen dit project hebben we drie eenvoudige scenario's voor de configuratie van microtubuli in plantencellen onderzocht: groei in een quasi-tweedimensionale ruimte, groei in een 'micro-kamer' die lijkt op een plantencel en groei in dezelfde situatie met toegevoegde interactie van de microtubuli met moleculen die de microtubuli actief kunnen verplaatsen. Deze drie situaties worden besproken in de hoofdstukken 3, 4 en 5 van dit proefschrift.

De belangrijkste conclusie is dat hoewel passieve mechanismen zoals elasticiteit van microtubuli en onderlinge hindering een belangrijke rol kunnen spelen in het ontstaan van de waargenomen patronen, actieve mechanismen net zo belangrijk zijn. Maar er blijven nog vele vragen onbeantwoord, met name over de identificatie van de actieve mechanismen. Dit opent de weg naar nieuw biologisch en natuurkundig onderzoek dat de komende jaren kan worden uitgevoerd op AMOLF en in Wageningen. Van biologische zijde is de grootste uitdaging om verder onderzoek te doen naar de rol van moleculaire motoren, moleculen die krachten uitoefenen op microtubuli. Van natuurkundige zijde kan de rol van deze motoren en andere actieve processen worden onderzocht zowel door middel van *in vitro* experimenten, zoals die in dit proefschrift beschreven zijn, als door middel van meer gedetailleerde modellen, volgens de richtlijnen uit hoofdstuk 5.

2. Het tweede deel van dit proefschrift beschrijft onderzoek dat is uitgevoerd in samenwerking met F. Capuani (AMOLF), C. P. Lowe (Universiteit van Amsterdam) en I. Pagonabarraga (Universiteit van Barcelona). Het gaat over een andere belangrijke toepassing van cytoskelet-filamenten. Sommige gespecialiseerde cellen gebruiken deze om een vloeistof voort te stuwen of om *zichzelf* voort te stuwen in een vloeistof, zoals het geval is bij een spermatozoïde. De staart hiervan heet een *flagellum*. Flagella zijn lange, dunne uitsteeksels van het celmembraan die een complexe bundel van microtubuli en actieve eiwitten bevatten. Deze eiwitten gebruiken chemische energie om de flagella te vervormen op een zodanige wijze dat de cel zich kan voortbewegen in een vloeistof.

Zwemmen is geen eenvoudige opgave voor een klein object zoals een cel, omdat het niet kan vertrouwen op zijn eigen traagheid, zoals wij dat doen. Als je bijvoorbeeld deze pagina zou verscheuren (na deze hopelijk eerst gelezen te hebben), zou verfrommelen en weg zou gooien, weet je dat de vliegende prop een paar meter af zal leggen. De traagheid zorgt ervoor dat hij blijft bewegen totdat deze tot stilstand wordt gebracht door wrijving met de lucht (of contact met de grond). Als we de microscopische wereld van de cel zouden opblazen tot onze macroscopische dimensies en hetzelfde experiment zouden herhalen zou hetzelfde projectiel slechts een nanometer (een duizend-miljoenste meter) afleggen voordat deze tot stilstand zou komen! In een wereld zonder traagheid is het erg lastig je los te maken van je omgeving.

In plaats het probleem van de flagella in alle volledigheid aan te pakken heb ik gekeken naar een simpeler model: de ‘een-armige zwemmer’. Dat wil zeggen een flexibele staaf die wordt aangedreven aan één uiteinde. In hoofdstuk 8 beschrijf ik een numerieke studie naar de wijze waarop een dergelijke staaf kan zwemmen in afwezigheid van traagheid en hoe snel en efficiënt dit kan zijn. In hoofdstuk 9 presenteer ik vervolgens een simulatiemethode die gebruikt kan worden om ook hydrodynamische interacties tussen filamenten en coöperatieve effecten in rekening te brengen, zoals het zwemmen door middel van vele filamenten.

De resultaten uit beide hoofdstukken geven aan dat zwemmen met behulp van één arm een goede methode is voor een micro-organisme om zich voort te bewegen, zowel vanuit het oogpunt van snelheid als efficiëntie. De vraag die zich aandient is dus: waarom bestaat de één-armige zwemmer niet in de natuur? Een mogelijk antwoord op deze vraag is het bestaan van een evolutionaire barrière. Inderdaad laten de resultaten zien dat het voor een één-armige zwemmer niet effectief is om gebruik te maken van een korte of langzaam bewegende arm, terwijl een primitieve arm deze beide eigenschappen waarschijnlijk zou hebben.

De meest veelbelovende richting voor vervolgonderzoek is gerelateerd aan de hydrodynamische methode uit hoofdstuk 9. Deze methode is tot nu toe slechts toegepast op de één-armige zwemmer en het probleem van sedimentatie, maar kan eenvoudig worden gebruikt voor simulaties met interacties tussen vele filamenten. Hiermee kan bijvoorbeeld de vraag worden beantwoord of twee spermatozoiden samen sneller zwemmen dan alleen.

Samenvatting

Curriculum Vitae

Marco Cosentino Lagomarsino was born in Verona, Italy, on the 26th of June 1974. He spent the first twenty-five years of his life in the outskirts of Milan, Italy, where he went to elementary, middle and high school. During his fourth high school year, he was an exchange student in Venice, Florida, USA. Back in Milan, he studied physics at the State University, where he graduated in theoretical physics in 1999, with the thesis “Active transport far from equilibrium, the case of molecular motors. Dynamics. Cooperative effects. Thermodynamics”, having Bruno Bassetti as a supervisor. He collaborated with the theory group there for one more year. Then, in March 2000, he moved to Amsterdam (where he has lived since), starting a PhD at AMOLF, in the group of Marileen Dogterom. He plays percussions and has also worked as: librarian, counselor, guide of a science museum, cool-hunter. After spending his life in the Lombardy plain, Florida and Holland, he is currently considering to move in a more rugged landscape.

